Ph.D. Dissertation

International Doctoral School in Information

and Communication Technology

DISI - University of Trento

Innovative Inversion Approaches for Buried Objects Detection and Imaging

Marco Salucci

Tutor:
  Andrea Massa, Professor
  University of Trento
Advisor:
  Giacomo Oliveri, Aggregate Professor
  University of Trento
Co-Advisor:
  Paolo Rocca, Aggregate Professor
  University of Trento

November 2014

To my parents Franca and Massimo, and to my colleagues and friends of the ELEDIA Research Center. Thank you all.

Abstract

The study, development, and analysis of innovative inversion techniques for the detection and imaging of buried objects is addressed in this thesis. The proposed methodologies are based on the use of microwave radiations and radar techniques for subsurface prospecting, such as, for example, the Ground Penetrating Radar (GPR). More precisely, the reconstruction of shallow buried objects is firstly addressed by an electromagnetic inverse scattering method based on the integration of the inexact Newton (IN) method with an interative multiscaling approach. The performances of such an inversion approach are analyzed both when considering the use of a second-order Born approximation ($SOBA$) and when exploiting the full set of non-linear equations governing the scattering phenomena for the buried scenario. The presented methodologies are particularly suitable for applications such as demining (e.g., for the detection of unexploded ordnances, $UXOs$, and improvised explosive devices, $IEDs$), for civil engineering applications (e.g., for the investigation of possible structural damages, voids, cracks or water infiltrations in walls, pillars, bridges) as well as for biomedical imaging (e.g., for early cancer detection).

Keywords
Ground Penetrating Radar (GPR), Inverse Scattering, Microwave Imaging, Iterative Multi-Scaling Approach, Inexact Newton, Conjugate Gradient, Frequency Hopping

Published Conference Papers

[C1]   F. Viani, M. Donelli, M. Salucci, P. Rocca, and A. Massa, "Opportunistic exploitation of wireless infrastructures for homeland security," *Proc. 2011 IEEE AP-S International Symposium*, Spokane, Washington, USA, pp. 3062-3065, July 3-8, 2011.

[C2]   F. Viani, M. Salucci, P. Rocca, G. Oliveri, and A. Massa, "A multi-sensor WSN backbone for museum monitoring and surveillance," *EuCAP* 2012, Prague, Czech Republic, March 26-30, 2012.

[C3]   A. Saverio, T. Cadili, G. Liborio, M. Russo, G. Oliveri, M. Salucci, and A. Massa, "A GA-based strategy for the calibration of satellite communication phased array antennas," *EuCAP* 2013, Gothenburg, Sweden, April 8-12, 2013.

[C4]   G. Oliveri, M. Salucci, A. Massa, D. Gonzalez-Ovejero, and C. Craeye, "Analytically designed planar aperiodic arrays in the presence of mutual coupling," *EuCAP* 2013, Gothenburg, Sweden, April 8-12, 2013.

[C5]   F. Viani, F. Robol, M. Salucci, E. Giarola, S. De Vigili, M. Rocca, F. Boldrini, G. Benedetti, and A. Massa, "WSN-based early alert system for preventing wildlife-vehicle collisions in Alps regions - From the laboratory test to the real-world implementation," *EuCAP* 2013, Gothenburg, Sweden, April 8-12, 2013.

[C6]   L. Manica, P. Rocca, M. Salucci, M. Carlin, and A. Massa, "Scattering data inversion through interval analysis under Rytov approximation," *EuCAP* 2013, Gothenburg, Sweden, April 8-12, 2013.

[C7]   M. Salucci, D. Sartori, N. Anselmi, A. Randazzo, G. Oliveri, and A. Massa, "Imaging buried objects within the second-order Born approximation through a multiresolution-regularized inexact-Newton method," 2013 *International Symposium on Electromagnetic Theory* (EMTS 2013), Hiroshima, Japan, May 20-24, 2013 (Invited).

[C8]   G. Oliveri, P. Rocca, M. Salucci, E. T. Bekele, D. H. Werner, and A. Massa, "Design and synthesis of innovative metamaterial-enhanced

arrays," *Proc. 2013 IEEE AP-S International Symposium*, Lake Buena Vista, Florida, USA, July 7-12, 2013.

[C9]   M. Salucci, P. Rocca, G. Oliveri, and A. Massa, "An innovative frequency hopping multizoom inversion strategy for GPR subsurface imaging," *15th International Conference on Ground Penetrating Radar* (GPR 2014), Brussels, Belgium, June 30 - July 04, 2014.

[C10]   M. Salucci, G. Oliveri, A. Randazzo, M. Pastorino, and A. Massa, "Multi-Focusing Procedure based on the Inexact-Newton Method for Electromagnetic Subsurface Prospecting," *European Geosciences Union General Assembly* (EGU2014), Vienna, Austria, April 27 - May 2, 2014.

[C11]   M. Salucci, L. Tenuti, C. Nardin, G. Oliveri, F. Viani, P. Rocca, and A. Massa , "Civil engineering applications of ground penetrating radar recent advances @ the ELEDIA Research Center," *European Geosciences Union General Assembly* (EGU2014), Vienna, Austria, April 27 - May 2, 2014.

[C12]   M. Salucci, L. Tenuti, C. Nardin, M. Carlin, F. Viani, G. Oliveri and A. Massa, "Gpr survey through a multi-resolution deterministic approach," *IEEE AP-S International Symposium*, Memphis, Tennessee, USA, July 6-12, 2014.

[C13]   L. Manica, G. Oliveri, E. Bekele, M. Carlin, M. Salucci, C. Nardin, E. Martini, S. Maci, and A. Massa, "Optimized synthesis of wave-manipulating devices within the system-by-design paradigm," *IEEE AP-S International Symposium*, Memphis, Tennessee, USA, July 6-12, 2014.

[C14]   A. Massa, G. Oliveri, M. Salucci, C. Nardin, and P. Rocca, "Dealing with EM functional optimization through new generation evolutionary-based methods," *IEEE International Conference on Numerical Electromagnetic Modeling and Optimization for RF, Microwave and Terahertz Applications*, Pavia, Italy, May 14-16, 2014 (Invited).

[C15]   M. Salucci, G. Oliveri, M. Gregory, D. Werner, and A. Massa, "A frequency-tunable metamaterial-based antenna using a reconfigurable AMC groundplane," *8th European Conference on Antennas and Propagation* (EuCAP 2014), The Hague, The Netherlands, Apr. 6-11, 2014.

[C16]   L. Poli, M. Salucci, P. Rocca, and A. Massa, "Adaptive GA-based thinning strategy for pattern nulling in sub-arrayed phased arrays," *8th European Conference on Antennas and Propagation* (EUCAP 2014), The Hague, The Netherlands, Apr. 6-11, 2014.

[C17]   T. Moriyama, M. Salucci, G. Oliveri, L. Tenuti, P. Rocca, and A. Massa, "Multi-scaling deterministic imaging for GPR survey," *IEEE International Conference on Antenna Measurements & Applications* (IEEE CAMA 2014), (Antibes Juan-les-Pins, France), Nov. 16-19 2014.

[C18]   G. Oliveri, P. Rocca, M. Salucci, and A. Massa, "Efficient synthesis of complex antenna devices through system-by-design," *Proc. 2014 IEEE Symposium Series on Computational Intelligence* (IEEE SSCI 2014), Orlando, Florida, USA, December 9-12, 2014 (Accepted).

[C19]   G. Oliveri, P. Rocca, M. Salucci, and A. Massa, "Evolution of nature-inspired optimization for new generation antenna design," *Proc. 2014 IEEE Symposium Series on Computational Intelligence* (IEEE SSCI 2014), Orlando, Florida, USA, December 9-12, 2014 (Accepted).

[C20]   G. Oliveri, P. Rocca, D. H. Werner, E. Bekele, M. Salucci, and A. Massa, "Design and synthesis of innovative metamaterial-enhanced arrays," *2013 IEEE Antennas and Propagation Society International Symposium*, (Orlando, USA), pp. 972-973, July 7-13, 2013.

[C21]   M. Carlin, M. Salucci, L. Tenuti, P. Rocca, and A. Massa, "Efficient radome optimization through the system-by-design methodology," 9th European Conference on Antennas and Propagation (EUCAP 2015), Lisbon, Portugal, April 12-17, 2015 (Submitted).

[C22]   L. Tenuti, M. Salucci, L. Poli, G. Oliveri, and A. Massa, "Physical-information exploitation in inverse scattering approaches for GPR survey," *9th European Conference on Antennas and Propagation* (EUCAP 2015), Lisbon, Portugal, April 12-17, 2015 (Submitted).

[C23]   F. Viani, M. Salucci, F. Robol, E. Giarola, and A. Massa, "WSNs as enabling tool for next generation smart systems," *Atti XIX Riunione Nazionale di Elettromagnetismo* (XIX RiNEm), Roma, pp. 393-396, 10-14 Settembre 2012.

Published Journals Papers

[R1]   F. Viani, M. Salucci, F. Robol, G. Oliveri, and A. Massa, "Design of a UHF RFID/GPS fractal antenna for logistics management," *Journal of Electromagnetic Waves and Applications*, vol. 26, no. 4, pp. 480-492, 2012.

[R2]   F. Viani, M. Salucci, F. Robol, and A. Massa, "Multiband Fractal ZigBee/WLAN Antenna for Ubiquitous Wireless Environments," *Journal of Electromagnetic Waves and Applications*, vol. 26, no. 11-12, pp. 1554-1562, 2012.

[R3]   L. Poli, P. Rocca, M. Salucci, and A. Massa, "Reconfigurable thinning for the adaptive control of linear arrays," *IEEE Transactions on Antennas and Propagation*, vol. 61, no. 10, pp. 5068-5077, 2013.

[R4]   B. Majone, F. Viani, E. Filippi, A. Bellin, A. Massa, G. Toller, F. Robol and M. Salucci, "Wireless sensor network deployment for monitoring soil moisture dynamics at the field scale," *Procedia Environmental Sciences*, vol. 19, pp. 426-435, 2013.

[R5]   M. Salucci, G. Oliveri, A. Randazzo, M. Pastorino, and A. Massa, "Electromagnetic subsurface prospecting by a multi-focusing inexact Newton method within the second-order Born approximation," *Journal of Optical Society of America A*, vol. 31, no. 6, pp. 1167-1179, 2014.

[R6]   T. Moriyama, G. Oliveri, M. Salucci, and T. Takenaka, "A multi-scaling forward-backward timestepping method for microwave imaging," *IEICE Electronics Express*, vol. 11, no. 16, id. 20140569, pp. 1-10, Aug. 2014. doi:10.1587/elex.11.20140578.

[R7]   T. Moriyama, E. Giarola, M. Salucci, and G. Oliveri, "On the radiation properties of ADS thinned dipole arrays," *IEICE Electronics Express*, vol. 11, no. 16, id. 20140578, pp. 1-12, Aug. 2014. doi:10.1587/elex.11.20140569.

[R8]   M. Salucci, G. Oliveri, A. Randazzo, M. Pastorino, and A. Massa, "Electromagnetic subsurface prospecting by a fully nonlinear multi-focusing inexact Newton method," *Journal of Optical Society of America A*, vol. 31, no. 12, pp. 2618-2629, 2014.

Contents

List of Tables

List of Figures

Chapter 1

Introduction

In recent years, there has been a growing interest in the development of imaging systems based on the use of microwave radiations [1]-[5]. Due to the comparable values of the incident wavelength and object linear dimensions, the physical phenomenon involved in these systems is the scattering of electromagnetic waves. Approaches based on microwaves can be profitably employed in several diagnostic scenarios, such as nondestructive testing and evaluation (NDT/NDE) of materials in civil engineering [6]-[9], medical imaging for breast cancer detection [10]-[12], shallow investigation of Earth's subsurface [13] as well as retrieval of electromagnetic and geometrical characteristics of scatterers buried under the air-soil interface [14][18].

One of the key instruments for subsurface monitoring and imaging is the ground penetrating radar (GPR) [13][19] which can be used, for example, for verifying the structural stability of concrete structures and for crack detection inside inaccessible materials. Although very good results have been obtained by using GPR, the solution of inverse scattering problems for buried detection is still a challenging issue, especially considering the need for fast and accurate apparatuses for illuminating the target under test and measuring the scattered radiation, as well as for efficient procedures to retrieve the geometrical and dielectric properties of objects buried under ground with an acceptable level of resolution. In particular, concerning the inversion procedures, it seems that further researches are required in order to overcome the limitations arising from the well known issues of *non-linearity* and *ill-posedness* characterizing the basic electromagnetic formulation [5]. The *non-linearity* is directly linked to the dependence of the unknown total field inside the investigation area on the scatterer properties [20], while the *ill-posedness* causes the solution to be extremely sensitive to noise affecting available data for the inversion. Moreover, the available measured data are limited and practical measurements are carried out from limited transmitter-receiver positions, resulting in limited data diversity [20]. For these reasons, efficient regularization techniques [21]-[23] capable to mitigate the above mentioned issues are needed. Approaches based on Rytov [24] and Tikhonov strategies [2] have

1

been exploited, along with numerical approximations such as first-order [25][26] and second-order [27]-[29] Born approximations.

In this context, it has also been proved that deterministic inversion procedures [30]-[32] can provide very accurate reconstruction results, although they suffer from a strong dependence on the initialization phase. On the other hand, the use of stochastic techniques has also been proposed [33]-[38]. Stochastic approaches can efficiently overcome the above limitation, but they exhibit a significantly higher computational cost [41][42].

Among deterministic approaches, inexact-Newton (IN) methods [28][29][43]-[49] have been proven to be effective as linearization and regularization tools for solving inverse-scattering problems, both numerically and experimentally [44]. Basically, these methods provide a linearization of the imaging equations by means of a Newton's expansion through the Fréchet derivative, and solve them in an approximate way [29]. However, the application of such an approach has been mainly limited to the free-space scenario, while a more complex formulation is needed when dealing with subsurface prospecting [50]. The IN method has been preliminary applied to retrieve buried objects in [28] within the second-order Born approximation ($SOBA$) [27]. By exploiting such a second-order approximation, a significant reduction of the computational burden can be achieved, thanks to a reduction of the problem unknowns (the dielectric parameters), since the internal total electric field is written as the sum of the known incident field and the internal linearized scattered field (which is also expressed in terms of the transmitted field) [29].

It must be also noticed that multi-resolution approaches [51]-[53] have been proven to be very effective in reducing the amount of local minima arising from the *non-linearity* of the free-space inverse-scattering problem, bringing a better exploitation of the available information from collected data and yielding both accurate reconstructions and high computational efficiency. The synergetic integration of a direct regularization technique, such as the IN method, and the iterative multi-scaling approach ($IMSA$) [54] has been shown to effectively tackle both the *non-linearity* and the *ill-posedness/ill-conditioning* of microwave imaging problems by exploiting the best properties of the two strategies and mutually overcoming their intrinsic limitations in tomographic imaging [48]-[47]. As a matter of fact the exploitation of such an approach leads to a strong simplification of the problem, thanks its capability to enforce a higher resolution only in the so-called regions-of-interest ($RoIs$) [54].

Moreover, a significant advantage in using GPR as the subsurface prospecting tool is represented by the availability of wide-band measurements [59], covering a wide range of the microwave radiation spectrum. In fact, pulsed GPR systems are based on the transmission of short electromagnetic pulses in time-domain [59], which penetrate inside the host medium and are partially reflected towards the receiving antennas each time a discontinuity of the dielectric characteristics is found. Given that, the capabilities of standard single-frequency inverse scat-

tering approaches can be further extended by introducing additional information coming from the intrinsic frequency diversity of the collected data. In such a way, the exploitation of wide-band GPR measurements requires the development of multi-frequency techniques which are able to profitably exploit the information associated to different components of the measured spectrum.

Following the above considerations, this thesis presents two efficient single-frequency techniques based on the integration of the inexact-Newton (IN) method with a multifocusing technique, and then a multi-frequency approach which is able to effectively exploit the frequency diversity of GPR measurements through a Frequency-Hopping (FH) scheme.

Thesis outline

The thesis is organized as follows. Firstly, the basic equation governing in frequency domain the scattering phenomena in subsurface problems are introduced in Chapter 2. Then, a single-frequency approach based on the IN method under the second order Born approximation $(SOBA)$ is presented in Chapter 3. An improved version of this technique, treating the full non-linear inverse scattering problem is shown in Chapter 4, extending to strong scatterers the imaging capabilities of the first approximated approach. Finally, Chapter 5 presents an innovative microwave inverse-scattering nested approach combining a Frequency-Hopping (FH) procedure and a Multi-Focusing (MF) technique for dealing with multi-frequency GPR measurements. Finally, a comparison among the different presented techniques is given and some final conclusions are drawn in Chapter 6.

Chapter 2

Inverse Scattering Equations for the Subsurface Problem

In this chapter, the basic equations mathematically modeling the subsurface inverse scattering problem in frequency domain are presented. More precisely, the two equations completely describing the fields measured within and outside the buried investigation domain are referred to as "*state*" and "*data*" equations. It is shown that the problem of retrieving the electromagnetic characteristics of unknown objects buried below the interface in a half space scenario can be reformulated as the minimization of a suitable cost function. Such a cost function accounts for both the mismatch between the measured and computed scattered field over a given observation domain and for the mismatch between the measured and the computed incident field within the investigation domain.

2.1 Geometry of the Problem

Let us consider a set of cylindrical scatterers buried in a homogeneous, isotropic and non-magnetic half space medium [Fig. 2.1]. The upper medium (i.e., $y > 0$) is supposed to be air, with dielectric properties equal to those of the vacuum ($\varepsilon_0 = 8.85 \times 10^{-12}$ Farad/m, $\mu_0 = 1.26 \times 10^{-6}$ Henry/m and $\sigma_0 = 0$ S/m). The lossy lower half space of background relative permittivity ε_{rB} and background conductivity σ_B S/m, contains a set of scatterers located within the known investigation domain D_{inv} [Fig. 2.1] and described by discontinuous (wrt the background) profiles of permittivity $\varepsilon_r(\mathbf{r})$ and conductivity $\sigma(\mathbf{r})$, where the position vector $\mathbf{r}$ denotes a point in the transverse plane (i.e., $\mathbf{r} = (x, y)$).
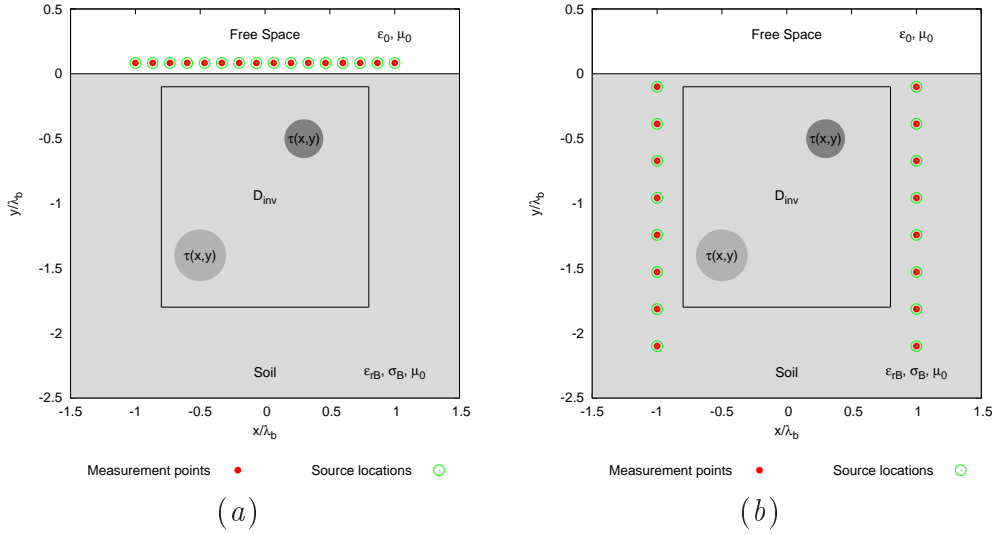
Figure 2.1: Geometry of a subsurface imaging problem. (a) Cross-borehole and (b) half space setup. λ_b is the wavelength in the background material.

2.2 Mathematical Formulation

In the following, we assume that the unknown buried targets are illuminated by a set of V incident monochromatic waves produced by a set of infinite line currents oriented along the z axis, which can be arranged in both half space [Fig. 2.1(a)] or cross-borehole [Fig. 2.1(b)] setup[1]. Given that, the generated incident waves are of transverse magnetic (TM) type, such that

$$\mathbf{E}_{inc}^{(v)}(\mathbf{r}) = E_{inc}^{(v)}(\mathbf{r})\,\widehat{\mathbf{z}}, \quad v = 1, ..., V. \tag{2.1}$$

---

[1]Hybrid configurations can exist, too, where the sources of em waves are displaced both above and below the interface separating the two homogeneous media.

Moreover, we assume that for each v-th illumination the longitudinal component of the scattered electric field vector is collected at M measurement points located at position $\mathbf{r}_m^{(v)}$, $m = 1, ..., M$ defining the observation domain D_{obs}. Following the classical inverse scattering approach [5], the problem of retrieving the shape, the position and the electromagnetic characteristics of the targets buried within D_{inv} is formulated as the problem of reconstructing the so-called contrast function, defined as

$$\tau(\mathbf{r}) = \frac{\varepsilon_{eq}(\mathbf{r}) - \varepsilon_{B,eq}}{\varepsilon_0} \tag{2.2}$$

where

$$\varepsilon_{eq}(\mathbf{r}) = \varepsilon_0 \varepsilon_r(\mathbf{r}) - j \frac{\sigma(\mathbf{r})}{\omega} \tag{2.3}$$

and

$$\varepsilon_{B,eq} = \varepsilon_0 \varepsilon_{rB} - j \frac{\sigma_B}{\omega} . \tag{2.4}$$

Given (2.3) and (2.4), it is easy to verify that the real part of the contrast is given by

$$\Re\{\tau(\mathbf{r})\} = \varepsilon_r(\mathbf{r}) - \varepsilon_{rB} \tag{2.5}$$

while the imaginary part depends on the frequency via the angular speed $\omega = 2\pi f$ as

$$\Im\{\tau(\mathbf{r})\} = \frac{\sigma_B - \sigma(\mathbf{r})}{\omega \varepsilon_0}. \tag{2.6}$$

Denoting with $v^{(j)}$ the cross-section of the j-th target buried within D_{inv} ($j = 1, ..., J$, being J the total number of scatterers), we then have

$$\tau(\mathbf{r}) = \begin{cases} 0 & \mathbf{r} \notin \sum_{j=1}^{J} v^{(j)} \\ \\ \tau(\mathbf{r}) & \mathbf{r} \in \sum_{j=1}^{J} v^{(j)} \end{cases} \tag{2.7}$$

since outside the support of the J buried targets the equivalent permittivity and the conductivity is that of the background medium (i.e., $\varepsilon_{eq}(\mathbf{r}) = \varepsilon_{B,eq}$ and $\sigma(\mathbf{r}) = \sigma_B$) and no discontinuity can be observed by the propagating impinging waves.

As a matter of fact, the total field measured at position $\mathbf{r}$ when the J targets are buried inside the investigation domain can be decomposed as the sum of two separate contributions, represented by the incident field and by the so-called scattered field, respectively

$$\mathbf{E}_{tot}^{(v)}(\mathbf{r}) = \mathbf{E}_{inc}^{(v)}(\mathbf{r}) + \mathbf{E}_{scatt}^{(v)}(\mathbf{r}), \quad v = 1, ..., V. \tag{2.8}$$

Given the cylindrical symmetry of the problem [Fig. 2.1] and the isotropic characteristics of the medium at hand, also the total field and the scattered field result z-oriented (i.e., $\mathbf{E}_{tot}^{(v)}(\mathbf{r}) = E_{tot}^{(v)}(\mathbf{r})\widehat{\mathbf{z}}$ and $\mathbf{E}_{scatt}^{(v)}(\mathbf{r}) = E_{scatt}^{(v)}(\mathbf{r})\widehat{\mathbf{z}}$, for

7

$v = 1, ..., V$). If on the one hand the incident field $\mathbf{E}_{inc}^{(v)}(\mathbf{r})$ is referred to the half space scenario when no objects are located below the interface [Fig. 2.1], on the other hand the scattered field is the contribution to the total field due to the presence of scatterers buried within D_{inv}. More precisely, the total field is completely described by means of the following set of Maxwell equations [59]

$$
\begin{cases}
\triangledown \times \mathbf{E}_{tot}^{(v)}(\mathbf{r}) = -j\omega\mu_0\mathbf{H}_{tot}^{(v)}(\mathbf{r}) \\[2mm]
\triangledown \times \mathbf{H}_{tot}^{(v)}(\mathbf{r}) = j\omega\varepsilon_{eq}(\mathbf{r})\mathbf{E}_{tot}^{(v)}(\mathbf{r}) + I_0\delta\left(x - x^{(v)}\right)\delta\left(y - y^{(v)}\right)\widehat{\mathbf{z}} \\[2mm]
\triangledown \cdot \varepsilon_{eq}(\mathbf{r})\mathbf{E}_{tot}^{(v)}(\mathbf{r}) = 0 \\[2mm]
\triangledown \cdot \mu_0\mathbf{H}_{tot}^{(v)}(\mathbf{r}) = 0
\end{cases}
\tag{2.9}
$$

where $\mathbf{H}_{tot}^{(v)}(\mathbf{r})$ is the total magnetic field at position $\mathbf{r}$

$$
\mathbf{H}_{tot}^{(v)}(\mathbf{r}) = H_{tot,x}^{(v)}(\mathbf{r})\widehat{\mathbf{x}} + H_{tot,y}^{(v)}(\mathbf{r})\widehat{\mathbf{y}}
\tag{2.10}
$$

and the impressed current for the v-th illumination is expressed in explicit form as

$$
\mathbf{J}_0(\mathbf{r}) = I_0\delta\left(x - x^{(v)}\right)\delta\left(y - y^{(v)}\right)\widehat{\mathbf{z}}
\tag{2.11}
$$

where I_0 is the amplitude of the current flowing along an infinite z-oriented line located at position $\left(x^{(v)}, y^{(v)}\right)$. In (2.9), the divergence of $\varepsilon_{eq}(\mathbf{r})\mathbf{E}_{tot}^{(v)}$ is set to null (i.e., $\varepsilon_{eq}(\mathbf{r})\mathbf{E}_{tot}^{(v)}$ is solenoidal) since it is easily verified that

$$
\triangledown \cdot \varepsilon_{eq}(\mathbf{r})\mathbf{E}_{tot}^{(v)} = \frac{\partial}{\partial z}\left\{\varepsilon_{eq}(x, y)E_{tot}^{(v)}(x, y)\right\} = 0.
\tag{2.12}
$$

Similarly, in absence of targets within D_{inv}, the incident field satisfies the following set of equations [59]

$$
\begin{cases}
\triangledown \times \mathbf{E}_{inc}^{(v)}(\mathbf{r}) = -j\omega\mu_0\mathbf{H}_{inc}^{(v)}(\mathbf{r}) \\[2mm]
\triangledown \times \mathbf{H}_{inc}^{(v)}(\mathbf{r}) = j\omega\varepsilon_{hs}\mathbf{E}_{inc}^{(v)}(\mathbf{r}) + I_0\delta\left(x - x^{(v)}\right)\delta\left(y - y^{(v)}\right)\widehat{\mathbf{z}} \\[2mm]
\triangledown \cdot \varepsilon_{hs}\mathbf{E}_{inc}^{(v)}(\mathbf{r}) = 0 \\[2mm]
\triangledown \cdot \mu_0\mathbf{H}_{inc}^{(v)}(\mathbf{r}) = 0
\end{cases}
\tag{2.13}
$$

where $\mathbf{H}_{inc}^{(v)}(\mathbf{r})$ is the incident magnetic field at position $\mathbf{r}$

$$
\mathbf{H}_{inc}^{(v)}(\mathbf{r}) = H_{inc,x}^{(v)}(\mathbf{r})\widehat{\mathbf{x}} + H_{inc,y}^{(v)}(\mathbf{r})\widehat{\mathbf{y}}
\tag{2.14}
$$

and ε_{hs} is a piece-wise constant function defining the (possibly complex) dielectric permittivity of the half space scenario at hand

$$\varepsilon_{hs} = \begin{cases} \varepsilon_0 & y > 0 \\ \\ \varepsilon_{B,eq} & y < 0. \end{cases} \tag{2.15}$$

Given that, it follows that the scattered field satisfies the following set of equations [59]

$$\begin{cases} \bigtriangledown \times \mathbf{E}_{scatt}^{(v)}(\mathbf{r}) = -j\omega\mu_0\mathbf{H}_{scatt}^{(v)}(\mathbf{r}) \\ \\ \bigtriangledown \times \mathbf{H}_{scatt}^{(v)}(\mathbf{r}) = j\omega\varepsilon_{hs}\mathbf{E}_{scatt}^{(v)}(\mathbf{r}) + j\omega\Delta\varepsilon(\mathbf{r})\mathbf{E}_{tot}^{(v)}(\mathbf{r}) \\ \\ \bigtriangledown \cdot \varepsilon_{hs}\mathbf{E}_{scatt}^{(v)}(\mathbf{r}) = 0 \\ \\ \bigtriangledown \cdot \mu_0\mathbf{H}_{scatt}^{(v)}(\mathbf{r}) = 0 \end{cases} \tag{2.16}$$

where $\mathbf{H}_{scatt}^{(v)}(\mathbf{r})$ is the scattered magnetic field at position $\mathbf{r}$

$$\mathbf{H}_{scatt}^{(v)}(\mathbf{r}) = H_{scatt,x}^{(v)}(\mathbf{r})\widehat{\mathbf{x}} + H_{scatt,y}^{(v)}(\mathbf{r})\widehat{\mathbf{y}} \tag{2.17}$$

and $\Delta\varepsilon(\mathbf{r})$ models the discontinuity between the dielectric permittivity of the scatterers and the surrounding homogeneous medium

$$\Delta\varepsilon(\mathbf{r}) = \varepsilon_{eq}(\mathbf{r}) - \varepsilon_{hs}. \tag{2.18}$$

By looking at (2.16) we can observe that the scattered field is due to an equivalent source that models the presence of the unknown scatterers inside D_{inv}, defined as [59]

$$\mathbf{J}_{eq}(\mathbf{r}) = j\omega\Delta\varepsilon(\mathbf{r})\mathbf{E}_{tot}^{(v)}(\mathbf{r}). \tag{2.19}$$

By re-arranging (2.16) and imposing the continuity of the tangential components of both the electric and magnetic fields at the interface (i.e., at $y = 0$), eventually [59] the z-component of the scattered field for points located below the interface [i.e., $y < 0$, Fig. 2.1] can be computed as

$$E_{scatt}^{(v)}(\mathbf{r}) = k_B^2 \int_{D_{inv}} \tau(\mathbf{r}')E_{tot}^{(v)}(\mathbf{r}')\mathcal{G}_{buried}(\mathbf{r},\mathbf{r}')d\mathbf{r}' \tag{2.20}$$

while the scattered field for points located above the interface [i.e., $y > 0$, Fig. 2.1] is expressed as

$$E_{scatt}^{(v)}(\mathbf{r}) = k_B^2 \int_{D_{inv}} \tau(\mathbf{r}')E_{tot}^{(v)}(\mathbf{r}')\mathcal{G}_{half-space}(\mathbf{r},\mathbf{r}')d\mathbf{r}'. \tag{2.21}$$

In (2.20) the integral Green's function $\mathcal{G}_{buried}(\mathbf{r}, \mathbf{r}')$ relates points below the interface to points below the interface (i.e., $y < 0$ and $y' < 0$) and, according to Eq. (4.42) in [59] and to the definition of the contrast function given in (2.2), it is defined as

$$\mathcal{G}_{buried}(\mathbf{r}, \mathbf{r}') = \mathcal{G}_{buried}(x, y, x', y') =$$

$$\frac{-j}{4\pi}\left(\frac{\varepsilon_0}{\varepsilon_{B,eq}}\right)\int_{-\infty}^{+\infty}\frac{exp(-ju(x'-x))}{k_{yB}}\left[exp\left(-jk_{yB}\left|y - y'\right|\right) + \right. \tag{2.22}$$

$$\left. \frac{\mu_0 k_{yB} - \mu_0 k_{y0}}{\mu_0 k_{yB} + \mu_0 k_{y0}}exp\left(-jk_{yB}\left(y' + y\right)\right)\right]du$$

while the function $\mathcal{G}_{half-space}(\mathbf{r}, \mathbf{r}')$ links points below the interface to points above the interface (i.e., $y > 0$ and $y' < 0$) and is defined as

$$\mathcal{G}_{half-space}(\mathbf{r}, \mathbf{r}') = \mathcal{G}_{half-space}(x, y, x', y') =$$

$$\frac{-j\mu_0}{2\pi}\left(\frac{\varepsilon_0}{\varepsilon_{B,eq}}\right)\int_{-\infty}^{+\infty}\frac{exp\left(-jk_{yB}y'\right)exp(jk_{y0}y)exp(-ju(x'-x))}{\mu_0 k_{yB} + \mu_0 k_{y0}}du. \tag{2.23}$$

In (2.22) and (2.23) k_{y0} and k_{yB} are functions of the integration variable u and are defined as follows

$$\begin{cases} k_{y0}^2 = k_{y0}^2(u) = k_0^2 - u^2 & y > 0 \\ k_{yB}^2 = k_B^2(u) = k_B^2 - u^2 & y < 0 \end{cases} \tag{2.24}$$

where $k_0 = \omega\sqrt{\varepsilon_0\mu_0}$ and $k_B = \omega\sqrt{\varepsilon_{B,eq}\mu_0}$ are the wave-number in free-space and in the lossy background medium, respectively. Finally, the following scalar integral equations can be retrieved, mathematically modeling the buried scattering problem

$$E_{inc}^{(v)}(\mathbf{r}) = E_{tot}^{(v)}(\mathbf{r}) - k_B^2 \int_{D_{inv}} \tau(\mathbf{r}') E_{tot}^{(v)}(\mathbf{r}') \mathcal{G}_{int}(\mathbf{r}, \mathbf{r}') d\mathbf{r}'$$

$$\mathbf{r} \in D_{inv} \tag{2.25}$$

$$E_{scatt}^{(v)}(\mathbf{r}) = k_B^2 \int_{D_{inv}} \tau(\mathbf{r}') E_{tot}^{(v)}(\mathbf{r}') \mathcal{G}_{ext}(\mathbf{r}, \mathbf{r}') d\mathbf{r}'$$

$$\mathbf{r} \in D_{obs} \tag{2.26}$$

in which $D_{obs} \notin D_{inv}$ is the observation domain, where both sources and measurement points are supposed to be located [Fig. 2.1]. The former integral equation is called "*state equation*", while the latter is the so-called "*data equation*", and both need to be solved in a numerical way in order to retrieve the unknown contrast function $\tau(\mathbf{r})$ and the unknown total field inside D_{inv}. Clearly, since $\mathcal{G}_{int}(\mathbf{r}, \mathbf{r}')$ (commonly known as the "*internal*" Green's function) relates points which are located inside D_{inv}, it will always coincide with $\mathcal{G}_{buried}(\mathbf{r}, \mathbf{r}')$. On the

other hand, $\mathcal{G}_{ext}(\mathbf{r}, \mathbf{r}')$ (commonly known as the "*external*" Green's function) relates points inside D_{inv} to points outside it (i.e., belonging to the observation domain $D_{obs} \notin D_{inv}$). Then, if a half space setup is considered, where measurement points are located above the interface (i.e., $y_m^{(v)} > 0$, for $v = 1, ..., V$ and $m = 1, .., M$ [Fig. 2.1(a)]), we will have that $\mathcal{G}_{ext}(\mathbf{r}, \mathbf{r}') = \mathcal{G}_{half-space}(\mathbf{r}, \mathbf{r}')$. Otherwise, if a cross-borehole setup is considered, where measurement points are located below the interface (i.e., $y_m^{(v)} < 0$, for $v = 1, ..., V$ and $m = 1, .., M$ [Fig. 2.1(b)]), we will have that $\mathcal{G}_{ext}(\mathbf{r}, \mathbf{r}') = \mathcal{G}_{buried}(\mathbf{r}, \mathbf{r}')$.

In order to solve the inverse scattering problem, both the unknowns and the state and data equations need to be discretized. A common choice is to use rectangular basis functions [56] partitioning the investigation domain into N subdomains

$$\tau(\mathbf{r}) = \sum_{n=1}^{N} \tau(\mathbf{r}_n) \psi_n(\mathbf{r})$$

$$E_{tot}^{(v)}(\mathbf{r}) = \sum_{n=1}^{N} E_{tot}(\mathbf{r}_n) \psi_n(\mathbf{r})$$

(2.27)

resulting in the following vector of unknowns

$$\boldsymbol{\Theta} = \left\{ \tau(\mathbf{r}_n) \, ; \, E_{tot}^{(v)}(\mathbf{r}_n) \, ; \, n = 1, ..., N; \, v = 1, ..., V \right\}. \quad (2.28)$$

Given that, the discretized form of the "*state equation*" (2.25) becomes

$$E_{inc}^{(v)}(\mathbf{r}_n) = E_{tot}^{(v)}(\mathbf{r}_n) - k_B^2 \sum_{p=1}^{P} \tau(\mathbf{r}_p) E_{tot}^{(v)}(\mathbf{r}_p) \mathcal{G}_{int}(\mathbf{r}_n, \mathbf{r}_p)$$

(2.29)

$$\mathbf{r}_n, \, \mathbf{r}_p \in D_{inv}$$

while the data equation in (2.26) becomes

$$E_{scatt}^{(v)}\left(\mathbf{r}_m^{(v)}\right) = k_B^2 \sum_{n=1}^{N} \tau(\mathbf{r}_n) E_{tot}^{(v)}(\mathbf{r}_n) \mathcal{G}_{ext}\left(\mathbf{r}_m^{(v)}, \mathbf{r}_n\right)$$

$$\mathbf{r}_m^{(v)} \in D_{obs}, \, \mathbf{r}_n \in D_{inv}.$$

Solving the inverse scattering problem is then reformulated as the estimation of the unknown coefficients $\boldsymbol{\Theta}$ via the minimization of the following cost function

$$\Phi\left\{\hat{\boldsymbol{\Theta}}\right\} = \beta_{data}\Phi_{data}\left\{\hat{\boldsymbol{\Theta}}\right\} + \beta_{state}\Phi_{state}\left\{\hat{\boldsymbol{\Theta}}\right\} \quad (2.30)$$

where β_{data} and β_{state} are constant weights. In (2.30) the "*data*" term $\Phi_{data}\left\{\hat{\boldsymbol{\Theta}}\right\}$ quantifies the mismatch between the known scattered field collected at M points belonging to D_{obs} to the scattered field computed for the retrieved versions of the unknowns (i.e., $\hat{\boldsymbol{\Theta}} = \left\{ \hat{\tau}(\mathbf{r}_n) \, ; \, \hat{E}_{tot}^{(v)}(\mathbf{r}_n) \, ; \, n = 1, ..., N; \, v = 1, ..., V \right\}$) according to (2.26)

11

$$\Phi_{data}\left\{\hat{\boldsymbol{\Theta}}\right\} = \frac{\sum_{v=1}^{V}\sum_{m=1}^{M}\left|E_{scatt}^{(v)}\left(\mathbf{r}_m^{(v)}\right) - \hat{E}_{scatt}^{(v)}\left(\mathbf{r}_m^{(v)}\right)\right|^2}{\sum_{v=1}^{V}\sum_{m=1}^{M}\left|E_{scatt}^{(v)}\left(\mathbf{r}_m^{(v)}\right)\right|^2} \qquad (2.31)$$

where $\hat{E}_{scatt}^{(v)}\left(\mathbf{r}_m^{(v)}\right)$ is the computed scattered field for the m-th probe under the v-th illumination. Similarly, the "*state*" term of the cost function defined in (2.30) measures the difference between the known incident field inside D_{inv} to the retrieved incident field computed according (2.25) on the basis of the estimated $\hat{\boldsymbol{\Theta}}$

$$\Phi_{state}\left\{\hat{\boldsymbol{\Theta}}\right\} = \frac{\sum_{v=1}^{V}\sum_{n=1}^{N}\left|E_{inc}^{(v)}\left(\mathbf{r}_n\right) - \hat{E}_{inc}^{(v)}\left(\mathbf{r}_n\right)\right|^2}{\sum_{v=1}^{V}\sum_{n=1}^{N}\left|E_{inc}^{(v)}\left(\mathbf{r}_n\right)\right|^2} \qquad (2.32)$$

where $\hat{E}_{inc}^{(v)}\left(\mathbf{r}_n\right)$ is the computed scattered field for the n-th point in D_{inv} under the v-th illumination.

Chapter 3

Multi-Focusing Inexact Newton Method within the Second-Order Born Approximation

In this chapter, the reconstruction of a shallow buried object is addressed by an electromagnetic inverse scattering method based on combining different imaging modalities. In particular, the proposed approach integrates the inexact-Newton method with an iterative multi-scaling approach. Moreover, the use of the second-order Born approximation ($SOBA$) is exploited. A numerical validation is provided concerning the potentialities arising by combining the regularization capabilities of the inexact-Newton method and the effectiveness of the multi-focusing strategy to mitigate the non-linearity and ill-posedness of the inversion problem. Comparisons with the standard "bare" approach in terms of accuracy, robustness, noise levels, and computational efficiency are also included.

3.1 Introduction

The aim of this chapter is to reformulate the integrated $IMSA - IN$ inversion technique [48] in order to deal with subsurface imaging and to evaluate the effectiveness of such an approach when the second-order Born approximation ($SOBA$) is applied. Moreover, a direct comparison in terms of accuracy, robustness against different conditions and noise levels, as well as computational efficiency is given when directly comparing the proposed $IMSA - IN - SOBA$ approach with its standard "bare" implementation ($BARE - IN - SOBA$), as described in [28].

Towards this end, section 3.2 provides the basic mathematical formulation used to model the buried problem under the $SOBA$. In Sect. 3.3 the combined $IMSA - IN - SOBA$ is described. An in-depth numerical validation is then provided in Sect. 3.4 in order to analyze the performance of the proposed approach and to demonstrate its effectiveness and advantages over the $BARE - IN - SOBA$, under monochromatic transverse magnetic (TM) illumination conditions in a cross-borehole setup similar to that used in [37]. Finally, some conclusions are drawn (Sect. 3.5).

3.2 Problem Formulation

Let us consider a cylindrical scatterer buried in a homogeneous half space medium. A cross-borehole measurement configuration is assumed [Fig. 3.1]. Let $\tau(\mathbf{r})$ denote the contrast function inside the inspected area D_{inv}, as defined in equation (2.2). The upper medium is supposed to be air, with dielectric properties equal to those of the vacuum and the position vector $\mathbf{r}$ denotes a point in the transverse plane, i.e., $\mathbf{r} = (x, y)$.

The target, whose cross section is included in the inspected area D_{inv} is illuminated by V incident waves, which are produced by a set of infinite line currents. They generate incident waves of transverse magnetic type, such that $\mathbf{E}_{inc}^{(v)}(\mathbf{r}) = E_{inc}^{(v)}(\mathbf{r})\hat{\mathbf{z}}$, $v = 1, \ldots, V$. Due to the cylindrical geometry, the scattered and total fields results to be z-polarized, too.

The basic equation for this inverse problem is therefore the following scalar integral one

$$E_{scatt}^{(v)}(\mathbf{r}) = E_{tot}^{(v)}(\mathbf{r}) - E_{inc}^{(v)}(\mathbf{r}) = k_B^2 \int_{D_{inv}} \tau(\mathbf{r}') E_{tot}^{(v)}(\mathbf{r}') \mathcal{G}_{buried}(\mathbf{r}, \mathbf{r}') d\mathbf{r}', \quad (3.1)$$

which is a nonlinear ill-posed Lippman-Schwinger equation, whose kernel is the Green's function for the half space [55] with definition given in equation (2.22). In equation (3.1), $E_{tot}^{(v)}$ and $E_{scatt}^{(v)}$ are the z-components of the total and scattered electric fields (for the v-th illumination), respectively. Such equation is approximated by using a second-order Born expansion [27], i.e.,
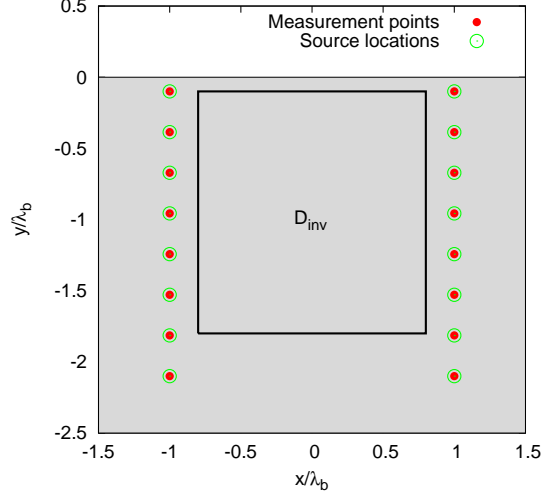
Figure 3.1: Geometry of the problem and imaging setup.

$$E_{scatt}^{(v)}(\mathbf{r}) \cong F_{B1}^{(v)}\tau(\mathbf{r}) + k_B^2 \int_{D_{inv}} \tau(\mathbf{r}') F_{B1}^{(v)}\tau(\mathbf{r}') \mathcal{G}_{buried}(\mathbf{r},\mathbf{r}') d\mathbf{r}' = F_{B2}^{(v)}(\tau)(\mathbf{r}),$$
$$(3.2)$$

where $F_{B1}^{(v)}$ denotes the first order Born operator defined as

$$F_{B1}^{(v)}\tau(\mathbf{r}) = k_B^2 \int_{D_{inv}} \tau(\mathbf{r}') E_{inc}^{(v)}(\mathbf{r}') \mathcal{G}_{buried}(\mathbf{r},\mathbf{r}') d\mathbf{r}'. \qquad (3.3)$$

Consequently, since the contrast function is independent of v, the inverse scattering problem can be formulated as the solution of the following set of equations with respect to the unknown τ

$$F_{B2}(\tau) = \begin{bmatrix} F_{B2}^{(1)}(\tau) \\ \vdots \\ F_{B2}^{(V)}(\tau) \end{bmatrix} = \begin{bmatrix} E_{scatt}^{(1)} \\ \vdots \\ E_{scatt}^{(V)} \end{bmatrix} = E_{scatt} \qquad (3.4)$$

The discrete counterparts of the above equations can be obtained by partitioning them in square subdomains in order to obtain pixelated images of the retrieved distributions of the dielectric parameters inside the inspected area.

3.3   Reconstruction Method

In order to solve equation (3.4), an inner/outer iterative scheme based on an IN method is applied [28]. The operator equation (3.4) is iteratively linearized by using the Frechét derivative of the operator F_{B2}. This step leads to the following linear operator equation

$$F'_{\tau_i} u = E_{scatt} - F_{B2}(\tau_i) \qquad (3.5)$$

where τ_i is the contrast function at the i-th iteration and F'_{τ_i} denotes the Frechét derivative of the operator F_{B2} at τ_i. As detailed in [29], F'_{τ_i} is given by

$$F'_{\tau_i} u = \begin{bmatrix} F'^{(1)}_{\tau_i} u \\ \vdots \\ F'^{(V)}_{\tau_i} u \end{bmatrix} \qquad (3.6)$$

where

$$\begin{aligned} F'^{(v)}_{\tau_i} u\left(\mathbf{r}\right) &= F^{(v)}_{B1} u\left(\mathbf{r}\right) + k_B^2 \int_{D_{inv}} \tau_i\left(\mathbf{r}'\right) F^{(v)}_{B1} u\left(\mathbf{r}'\right) \mathcal{G}_{buried}\left(\mathbf{r}, \mathbf{r}'\right) d\mathbf{r}' \\ &+ k_B^2 \int_{D_{inv}} u\left(\mathbf{r}'\right) F^{(v)}_{B1} \tau_i\left(\mathbf{r}'\right) \mathcal{G}_{buried}\left(\mathbf{r}, \mathbf{r}'\right) d\mathbf{r}' \end{aligned} \qquad (3.7)$$

As it is well known, equation (3.5) turns out the be ill-posed. Consequently, its solution can be obtained in a regularization sense by using a regularization method. In particular, following the approach in [44], a good choice seems to be the use of the Landweber iterative method [61]. In this case, a second loop is obtained by means of the following scheme

$$\begin{aligned} u_{i,0} &= 0 \\ u_{i,q+1} &= u_{i,q} - \rho_i F'^{*}_{\tau_i}\left(F'_{\tau_i} u_{i,q} - E_{scatt} + F_{B2}\left(\tau_i\right)\right), \end{aligned} \qquad (3.8)$$

where $F'^{*}_{\tau_i}$ is the the adjoint of F'_{τ_i} and $0 < \rho_i < 2\left\|F'_{\tau_i}\right\|_s^{-2}$, being $\|\cdot\|_s$ the spectral norm. A regularized solution u_i is obtained by truncating the iterations after a predefined number of steps Q. After the linearized problem is solved, the current contrast function is updated as

$$\tau_{i+1} = \tau_i + u_i \qquad (3.9)$$

and the algorithm is iterated until a predefined stopping criteria is fulfilled. It requires of course an initialization phase, in which an estimate of the dielectric properties of the inspected area is chosen. In most cases, an empty domain is used as initial guess.

As mentioned in Section 3.1, the effectiveness of an integrated procedure that profitably exploits the regularization capabilities of the IN method and the capability of the iterative multi-scaling approach ($IMSA$) [54] to reduce the occurrence of local minima has been already assessed in [48][49] for free-space imaging. Issues such as numerical instabilities caused by the presence of noise on measured data, as well as the *ill-conditioned* and *non-linear* nature of the inversion problem are thus jointly addressed, throughout the synergetic combination of both techniques.

In particular, at each s-th step of the $IMSA$ ($s = 1, ..., S$; s being the step index), the RoI $\Omega^{(s)}$ ($\Omega^{(1)}$ coinciding with D_{inv}) is defined and partitioned according to the Richmond's procedure [56] into N square sub-domains (N being the estimated number of degrees of freedom of the measured data [57][58]) centered at $\mathbf{r}_n^{(s)}$ ($\mathbf{r}_n^{(s)} \in \Omega^{(s)}$, $n = 1, ..., N$). Following the IN method formulation, the non-linear equation (3.4) is iteratively linearized in order to obtain the following

linear operator equation (note the addition of the superscript $^{(s)}$ with respect to
(3.5) to indicate the iterative nature of the multi-scaling approach)

$$\left(F_{\tau_i}^{(s)} \right)' u^{(s)} = E_{scatt} - F_{B2}^{(s)} \left(\tau_i^{(s)} \right) \tag{3.10}$$

As previously detailed, at each IN step, equation (3.10) is solved in a regularized
sense by means of an inner truncated Landweber loop, composed by the following
loop (initialized with $u_{i,0}^{(s)} = 0$)

$$u_{i,q+1}^{(s)} = u_{i,q}^{(s)} - \rho_i^{(s)} \left(F_{\tau_i}^{(s)} \right)'^* \left[\left(F_{\tau_i}^{(s)} \right)' u_{i,q}^{(s)} - E_{scatt} + F_{B2}^{(s)} \left(\tau_i^{(s)} \right) \right], \ q = 0, ..., Q-1 \tag{3.11}$$

The current solution is updated as $\tau_{i+1}^{(s)} = \tau_i^{(s)} + u_{i,Q}^{(s)}$ and the IN method is
iterated (i.e., by letting $i = i + 1$) until a suitable predefined stop criterion is
reached. Once the IN loop has been terminated, a new $IMSA$ step is initialized
(i.e., by letting $s = s + 1$), throughout the update of $\Omega^{(s)}$ and its discretization
with a finer resolution. This step requires to update the barycenters $\mathbf{r}_n^{(s)} \in \Omega^{(s)}$,
$n = 1, ..., N$.
The multi-step process is iterated until the verification of a suitable termination
condition (e.g., $s = S$), and $u^{(S)} = \tau^{(S)}$ is finally assumed as the $IMSA - IN -$
$SOBA$ solution.
It has been pointed out in [49] the importance of defining an efficient stopping
criterion for the $IMSA - IN - SOBA$ when no *a-priori* information on the
object under test is available. To monitor the evolution of the reconstruction
residual, a parameter is introduced, which is defined at each IN iteration i as the
discrepancy between measured and retrieved scattered field at M measurement
locations:

$$\Phi_i = \frac{\sum_{v=1}^{V} \sum_{m=1}^{M} \left\| E_{scatt}^{(v)}(\mathbf{r}_m^{(v)}) - \hat{E}_{scatt,i}^{(v)}(\mathbf{r}_m^{(v)}) \right\|_2^2}{\sum_{v=1}^{V} \sum_{m=1}^{M} \left\| E_{scatt}^{(v)}(\mathbf{r}_m^{(v)}) \right\|_2^2} \tag{3.12}$$

where $E_{scatt}^{(v)}(\mathbf{r}_m^{(v)})$ and $\hat{E}_{scatt,i}^{(v)}(\mathbf{r}_m^{(v)})$ denote the measured and estimated scattered
fields at the measurement point m ($m = 1, ..., M$) for the v-th illumination
($v = 1, ..., V$), while $\|.\|_2$ denotes the l^2-norm operator. The following *stationary
condition*, based on successive observations of the estimated residual, can then
be defined in order to adaptively terminate the IN procedure at each s-th step
of the multi-focusing scheme:

$$\zeta_i = \frac{\left| W\Phi_i - \sum_{j=1}^{W} \Phi_{i-j} \right|}{\Phi_i} \leq \eta \tag{3.13}$$

where η and W denote a fixed numerical threshold and a fixed number of IN
iterations, respectively. The definition of suitable values for both η and W has
clearly a critical impact on the overall performances of the $IMSA - IN - SOBA$,

since both parameters are essential to identify a stagnating behaviour of the residual, which is actually strongly linked to the *semiconvergence* property of the IN method when dealing with the regularization of noisy data [29]. Concerning the regularization capability of IN method algorithm, the number of iterations Q for the Landweber method should also be carefully chosen, as well as the number of multi-scaling iterations S should be set in order to successfully balance computational efficiency and overall quality of the retrieved images.

3.4 Numerical Assessment

This section is aimed at illustrating the potentialities of the proposed $IMSA-IN-SOBA$ method when dealing with the processing of synthetic data produced by both homogeneous and inhomogeneous scatterers buried in a lossy homogeneous half space medium. The significant advantage of the $IMSA-IN$ over the standard IN method has been already highlighted and well documented in [48][49] for the free-space scenario. The applicability of the IN method within the second-order Born approximation to the retrieval of buried objects has been successfully demonstrated in [28], as well. The analysis will thus focus on the advantages of employing the iterative multi-resolution inversion scheme over the "bare" IN method implementation within the $SOBA$ $(BARE-IN-SOBA)$, both in terms of accuracy, robustness when dealing with different scatterers and different noise conditions. Besides the pictorial representation of the retrieved dielectric distributions, the following error indexes will be used in the following to give a quantitative evaluation of the reconstruction accuracy:

$$\Xi_{reg} = \frac{1}{N_{reg}} \sum_{n=1}^{N_{reg}} \frac{|\hat{\tau}(x_n, y_n) - \tau(x_n, y_n)|}{|\tau(x_n, y_n) + 1|} \quad reg = tot, ext, int \qquad (3.14)$$

where N_{reg} indicates the number of cells covering the whole inspected area D_{inv} $(reg = tot, N_{tot} = N)$, or belonging to the background region $(reg = ext)$, or to the support of the buried scatterer $(reg = int; N_{tot} = N_{ext} + N_{int})$. Moreover, the terms $\hat{\tau}$ and τ in equation (3.14) indicate the retrieved and the actual contrast function for the n-th cell belonging to the investigation domain.
The first part of this Section is devoted to a sensitivity analysis of the $IMSA-IN-SOBA$ algorithm, aimed at investigating the effect of each control parameter on the final quality of the retrieved distributions when dealing with noisy data, in order to define a suitable and general setup.

3.4.1 Calibration of the $IMSA-IN-SOBA$

It should be stressed that, as already discussed in Section 3.3, the choice of the control parameters η, W, Q and S should be carefully performed in order to profitably exploit the capabilities of the $IMSA-IN-SOBA$.
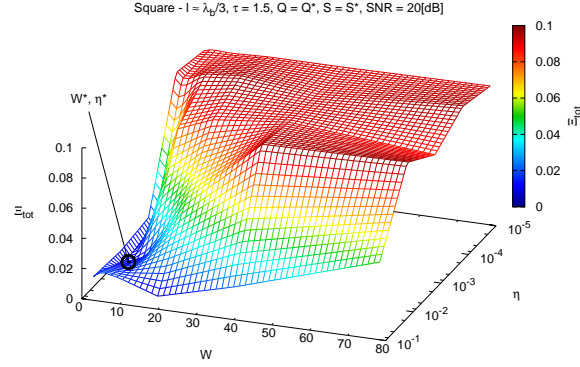
(a)
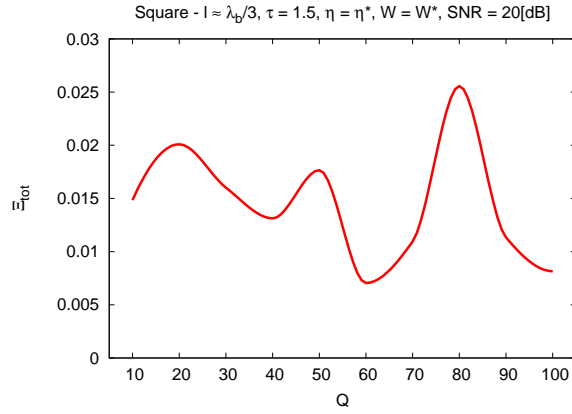
(b)
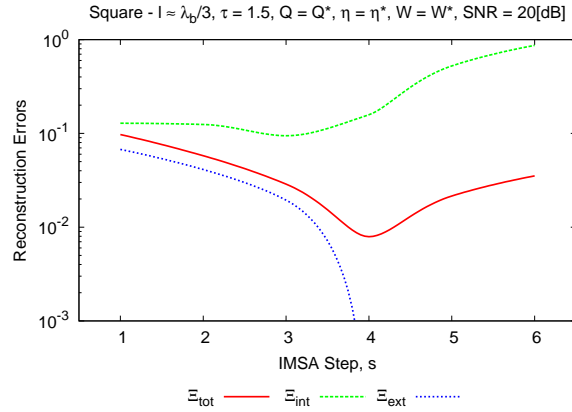
(c)

Figure 3.2: *Sensitivity Analysis (Homogeneous Square Scatterer - $\ell \approx \frac{\lambda_b}{3}$, $\tau = 1.5$, $SNR = 20$ dB)* - Behaviour of the integral error Ξ_{tot} versus η and W when $Q = Q^*$, $S = S^*$ (a), and versus K when $\eta = \eta^*$, $W = W^*$, and $S = S^*$ (b). Plot of the total, internal, and external error as a function of S when $Q = Q^*$, $\eta = \eta^*$, and $W = W^*$ (c).

19

Towards this end, an exhaustive sensitivity analysis on the impact of each control parameter has been performed on noisy field data ($SNR = 20$ dB) collected for an homogeneous lossy off-centered "square" cylinder, with side $l \approx \lambda_b/3$, λ_b being the wavelength inside the background, and $\tau = 0.5$ [Fig. 3.3 (a)]. Moreover, a square investigation domain of side $1.6\lambda_b$ located $0.1\lambda_b$ under the air-soil interface has has been assumed as reference scenario (Fig. 3.1). The homogeneous half space medium, inside which the scatterer is buried, is characterized by a relative dielectric permittivity $\varepsilon_{rB} = 4.0$ and by a conductivity $\sigma_B = 10^{-2}$ S/m. The investigation domain D_{inv} is sequentially illuminated by a set of $V = 16$ transverse-magnetic (TM) monochromatic plane waves generated by two vertical rows of field sources configured in a cross-borehole setup [Fig. 3.1] working at the frequency of $f = 300$ MHz. For each view, the synthetically generated scattered field is collected at $M = 15$ equally spaced measurement points (with $\pm 0.2\lambda_b$ offset along x with respect to the investigation domain [Fig. 3.1]). It is worthwhile to notice that that the values of V and M have been chosen following the guidelines in [57][58] to collect all the available information on D_{inv} from the measured scattered radiation. Moreover, the investigation area has been partitioned into $N = 100$ square sub-domains.

In order to investigate the impact of η and W on the achievable performances of the $IMSA - IN - SOBA$, Fig. 3.2(a) reports the total reconstruction error Ξ_{tot} as a two dimensional function of both parameters, when the number of Landweber and $IMSA$ iterations are respectively set to their optimal values Q^* and S^*.

As it can be observed, a low value of the threshold η (e.g., $\eta = 10^{-4}$) results completely inappropriate, leading to a significant degradation of the quality of the reconstructions, due the so-called *semiconvergence* property of the IN regularization technique [29].

Actually, the best reconstruction is obtained after a given number of IN iterations, while subsequent iterations give rise to worse solutions, since data are affected by noise [28]. Similarly, an high value of η also leads to inaccurate results, causing the premature termination of the inversion procedure. Therefore, a good choice for η is

$$\eta^* = 10^{-2} \tag{3.15}$$

and it has been assumed hereinafter for the $IMSA - IN - SOBA$ inversions. Even if less critical, a suitable value for W should also be carefully selected. As shown in equation (3.13), W defines the number of IN iterations which should be taken into account for the identification of a stagnating behaviour on the residual Φ. Although a small value of W can reduce the capability of filtering out numerical errors affecting the computation of the residual, high values of W give rise to a remarkable degradation of the performances, as depicted in Fig. 3.2(a), whatever the value of the threshold η. Given the above considerations, the optimal value of W has been set to

$$W^* = 5 \tag{3.16}$$

(a)

(b)

(c)
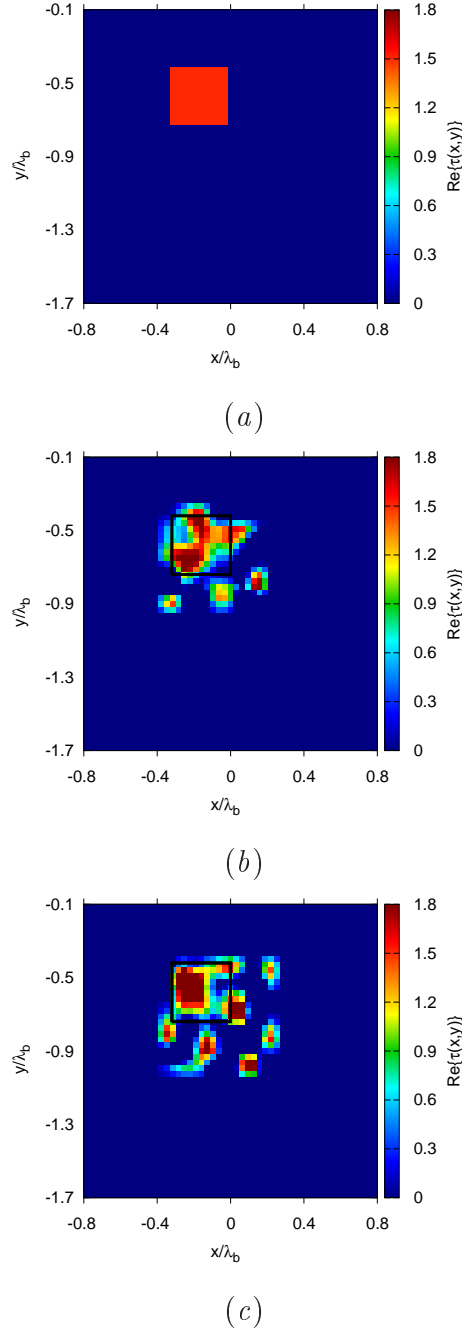
Figure 3.3: *Sensitivity Analysis* (*Homogeneous Square Scatterer* - $\ell \approx \frac{\lambda_b}{3}$, $\tau = 1.5$, $SNR = 20$ dB, $S = S*$) - Actual (a) and retrieved (b)(c) contrast profiles when (b) $Q = Q^*$, $W = W^*$, $\eta = 10^{-4}$; (c) $K = K^*$, $W = 40$, $\eta = \eta^*$.

and it will be used in the following of the discussion. For completeness, and to give the reader a pictorial example of what is the impact of a wrong choice of η and W on the $IMSA - IN - SOBA$ performances, the retrieved profiles

for the "square" cylinder of Fig. 3.3(a) are shown for $\eta = 10^{-4}$ [Fig. 3.3(b)] and $W = 40$ [Fig. 3.3(c)], being the other parameters fixed to their optimal values. The computed total error indexes are $\Xi_{tot}]_{\eta=10^{-4}, W=W^*} \approx 1.27 \times 10^{-1}$ and $\Xi_{tot}]_{\eta=\eta^*, W=40} \approx 2.12 \times 10^{-1}$, while a reduction of more than one order of magnitude on Ξ_{tot} can be achieved when jointly setting η and W to their optimal values ($\Xi_{tot}]_{\eta=\eta^*, W=W^*} \approx 7.92 \times 10^{-3}$) [Fig. 3.2($a$)].

Concerning the dependence of the inversion quality on the number of Landweber iterations, Fig. 3.2(b) shows the behaviour of Ξ_{tot} as a function of Q, when all remaining parameters are set to their optimal values. As a matter of fact, the number of iterations plays the role of a regularization parameter in the iterative Landweber regularization method, representing a heuristic compromise between fast convergence of the IN method (for low values of Q) and noise filtering (for high values of Q) [28]. Therefore, given the above considerations and also following the outcome of the performed sensitivity analysis (Fig. 3.2(b)), the number of inner iterations has been to

$$Q^* = 60 \tag{3.17}$$

an it will be considered for the successive analysis of the algorithm performances. Concerning the stop criterion for the iterative multi-zooming scheme, Fig. 3.2(c) reports the computed error indexes as a function of the $IMSA$ step s ($s = 1, .., 6$) in the case $\eta = \eta^*$, $W = W^*$ and $Q = Q^*$.

As it can be observed, the total error shows a rapid descent until step $s = 4$ is reached ($\Xi_{tot}^{s=1} \approx 9.73 \times 10^{-2}$ vs. $\Xi_{tot}^{s=4} \approx 7.92 \times 10^{-3}$), while a progressive degradation of the accuracy characterizes the remaining successive steps, as verified by the error indexes ($\Xi_{tot}^{s=5} \approx 2.15 \times 10^{-2}$ and $\Xi_{tot}^{s=6} \approx 3.52 \times 10^{-2}$). It is worth noticing that, although the external error reaches its null even before step $s = 4$, the suppression of artifacts inside the background region comes at the cost of a slight increment of the internal error. Given the above considerations, the optimal number of $IMSA$ steps has been identified as

$$S^* = 4 \tag{3.18}$$

and it will be employed as a good compromise for successive test cases. Figures 3.4(b)-3.4(e) illustrate the evolution of the reconstruction throughout the $IMSA - IN - SOBA$ steps, when the optimal values of each control parameter is set to its optimal value. As shown by the single plots, the retrieved profile improves step-by-step, starting from a rough estimation of the buried object support and dielectric characteristics [$s = 1$ - Fig. 3.4(b)] until a satisfactory reconstruction is reached [$s = 4 = S^*$ - Fig. 3.4(e)]. A pictorial representation of the evolution of the residual (equation (3.12)) and of the stationary index (equation(3.13)) throughout the multi-zooming steps is given Fig. 3.4(a).

(a)

(b)

(c)

(d)

(e)
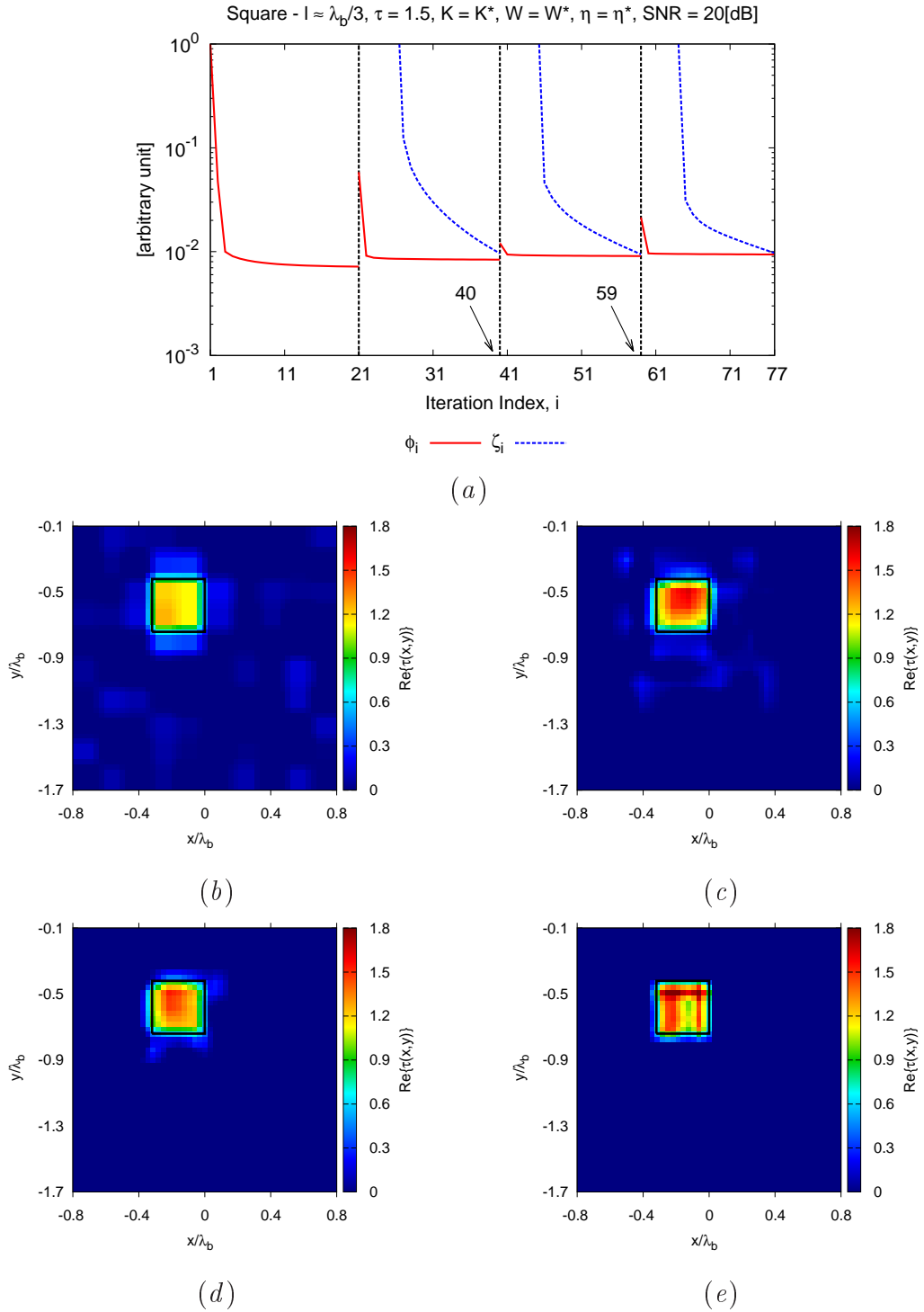
Figure 3.4: *Sensitivity Analysis (Homogeneous Square Scatterer -* $\ell \approx \frac{\lambda_b}{3}$, $\tau = 1.5$, $SNR = 20$ dB, $Q = Q^*$, $W = W^*$, $\eta = \eta^*$) - Behaviour of Φ and ζ versus the $IMSA - IN$ iteration number (a). Plot of the retrieved contrast profiles when (b) $S = 1$, (c) $S = 2$, (d) $S = 3$, (e) $S = 4 = S^*$.

23

3.4.2 Homogeneous "Square" and "L-shaped" Cylinders

The first set of numerical experiments deals with two off-centered lossy homogeneous scatterers having different cross-sections and characterized by a contrast $\tau = 1.5$ ["*Square*" and "*L-shaped*" profiles, - Fig. 3.5]. The $BARE-IN-SOBA$ reconstructions have been carried out by setting $Q = 20$ and $I = 20$ [28], while for the $IMSA-IN-SOBA$ the following parameters have been chosen, according to the previously discussed sensitivity analysis: $\eta = 10^{-2} = \eta^*$, $W = 5 = W^*$, $Q = 60 = Q^*$, and $S = 4 = S^*$. Moreover, the investigation domain D_{inv} has been partitioned into $N = 400$ and $N = 100$ square sub-domains for $BARE-IN-SOBA$ and $IMSA-IN-SOBA$ inversion techniques, respectively. All remaining parameters are kept equal to those employed in the previous paragraph.

Figs. 3.5(b)-3.5(c) show the retrieved profiles by the $BARE-IN-SOBA$, while Figs. 3.5(d)-3.5(e) the corresponding $IMSA-IN-SOBA$ reconstructions, in case the scattered field data is corrupted by an additive zero mean complex Gaussian noise, raising a signal-to-noise ratio equal to $SNR = 10$ dB. As it can be observed, the $IMSA-IN-SOBA$ is able to provide a remarkable improvement in terms of accuracy over the "bare" counterpart even in the presence of a strong noisy component on measurements, as quantitatively confirmed by the lower error ($\Xi_{tot}\rfloor_{"Square"}^{BARE-IN-SOBA} \approx 1.46 \times 10^{-1}$ vs. $\Xi_{tot}\rfloor_{"Square"}^{IMSA-IN-SOBA} \approx 1.24 \times 10^{-1}$ and $\Xi_{tot}\rfloor_{"L-shaped"}^{BARE-IN-SOBA} \approx 1.23 \times 10^{-1}$ vs. $\Xi_{tot}\rfloor_{"L-shaped"}^{IMSA-IN-SOBA} \approx 1.19 \times 10^{-1}$).

To further validate these outcomes, the results from a more exhaustive set of noisy cases have been summarized in Fig. 3.5(a), showing the achieved total reconstruction error Ξ_{tot} for different values of SNR for both the considered homogeneous scatterers. The result is that the $IMSA-IN-SOBA$ overcomes the "bare" IN method implementation in terms of reconstruction accuracy, as pointed out by the error curves in Fig. 3.5(a). Although the reconstruction quality degrades for both $BARE-IN-SOBA$ and $IMSA-IN-SOBA$ for lower signal-to-noise ratios, it turns out that $\Xi_{tot}^{IMSA-IN-SOBA} < \Xi_{tot}^{BARE-IN-SOBA}$ whatever the noise condition.

3.4.3 "O-shaped" Cylinder

In order to prove the general validity of the previously discussed outcomes on the $IMSA-IN-SOBA$ approach when dealing with the retrieval of more complex dielectric shapes with different values of τ, an homogeneous hollow square cylinder ("*O-shaped*" profile) with an outer side equal to $l \approx \lambda_b/2$ has been chosen as a more challenging benchmark geometry. In order to give the reader a full picture on the performance improvement of the $IMSA-IN-SOBA$ over the $BARE-IN-SOBA$, Fig. 3.6 illustrates the behaviour of the total error Ξ_{tot} as a function of τ, for different signal-to-noise ratios on scattered data.
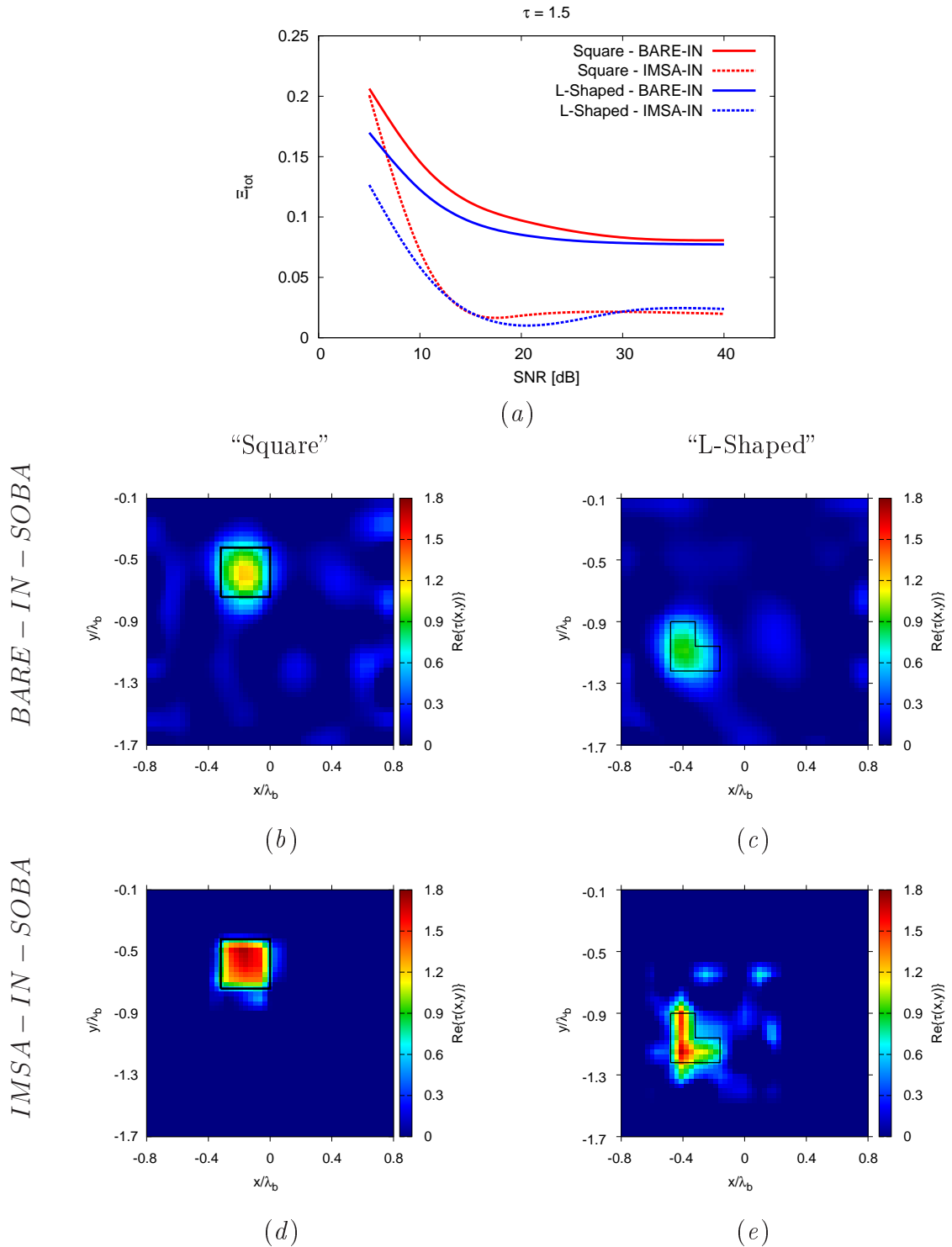
Figure 3.5: *Performance Assessment* ($\tau = 1.5$, $SNR \in [10, 40]$ dB) - Behaviour of the Ξ_{tot} as a function of SNR when dealing with "Square" or "L-Shaped" targets (a). Plot of the contrast profiles retrieved by (b)(c) $BARE - IN - SOBA$ and (d)(e) $IMSA - IN - SOBA$ when $SNR = 10$ dB. (b)(d) "Square" scatterer; (c)(e) "L-Shaped" scatterer.

25
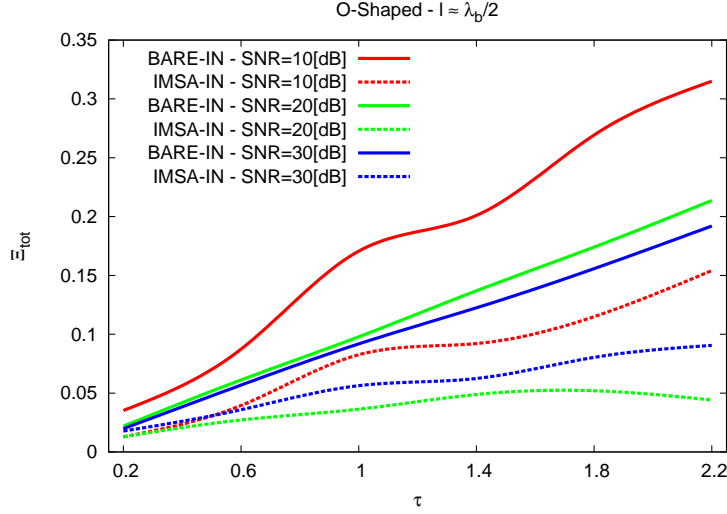
Figure 3.6: *Performance Assessment ("O-Shaped" Scatterer $\ell \approx \frac{\lambda_b}{2}$, $SNR \in [10, 30]$ dB) - Behaviour of the Ξ_{tot} as a function of τ obtained by $BARE-IN-SOBA$ and $IMSA-IN-SOBA$.*

Although the reconstruction accuracy degrades as τ increases, the $IMSA-IN-SOBA$ always provides the lowest error (e.g., $\Xi_{tot}^{BARE-IN-SOBA}\big]_{\tau=2.2} \approx 2.14 \times 10^{-1}$ vs. $\Xi_{tot}^{IMSA-IN-SOBA}\big]_{\tau=2.2} \approx 4.42 \times 10^{-2}$).

It is also worth to notice that, as reported in Fig. 3.6, the error index of the $IMSA-IN-SOBA$ for $SNR = 10$ dB is always lower than the error provided by the "bare" IN method implementation for a significantly higher signal-to-noise ratio ($SNR = 30$ dB). For completeness, the error indexes in Fig. 3.6 are also reported in Tab. 3.1.

$BARE-IN-SOBA$					
SNR dB	$\tau = 0.2$	$\tau = 0.6$	$\tau = 1.0$	$\tau = 1.4$	$\tau = 1.8$	$\tau = 2.2$
30	1.98×10^{-2}	5.68×10^{-2}	9.18×10^{-2}	1.22×10^{-1}	1.56×10^{-1}	1.92×10^{-1}
20	2.20×10^{-2}	6.12×10^{-2}	9.79×10^{-2}	1.37×10^{-1}	1.74×10^{-1}	2.14×10^{-1}
10	3.52×10^{-2}	8.74×10^{-2}	8.87×10^{-2}	2.01×10^{-1}	2.69×10^{-1}	3.15×10^{-1}
$IMSA-IN-SOBA$					
SNR dB	$\tau = 0.2$	$\tau = 0.6$	$\tau = 1.0$	$\tau = 1.4$	$\tau = 1.8$	$\tau = 2.2$
30	1.18×10^{-2}	3.59×10^{-2}	5.63×10^{-2}	6.24×10^{-2}	8.03×10^{-2}	9.06×10^{-2}
20	1.29×10^{-2}	2.72×10^{-2}	3.64×10^{-2}	4.88×10^{-2}	5.20×10^{-2}	4.42×10^{-2}
10	1.28×10^{-2}	3.95×10^{-2}	8.26×10^{-2}	9.21×10^{-2}	1.15×10^{-1}	1.54×10^{-1}

Table 3.1: *Performance Assessment ("O-Shaped" Scatterer $\ell \approx \frac{\lambda_b}{2}$, $SNR \in [10, 30]$ dB) - Error values and computational indexes.*
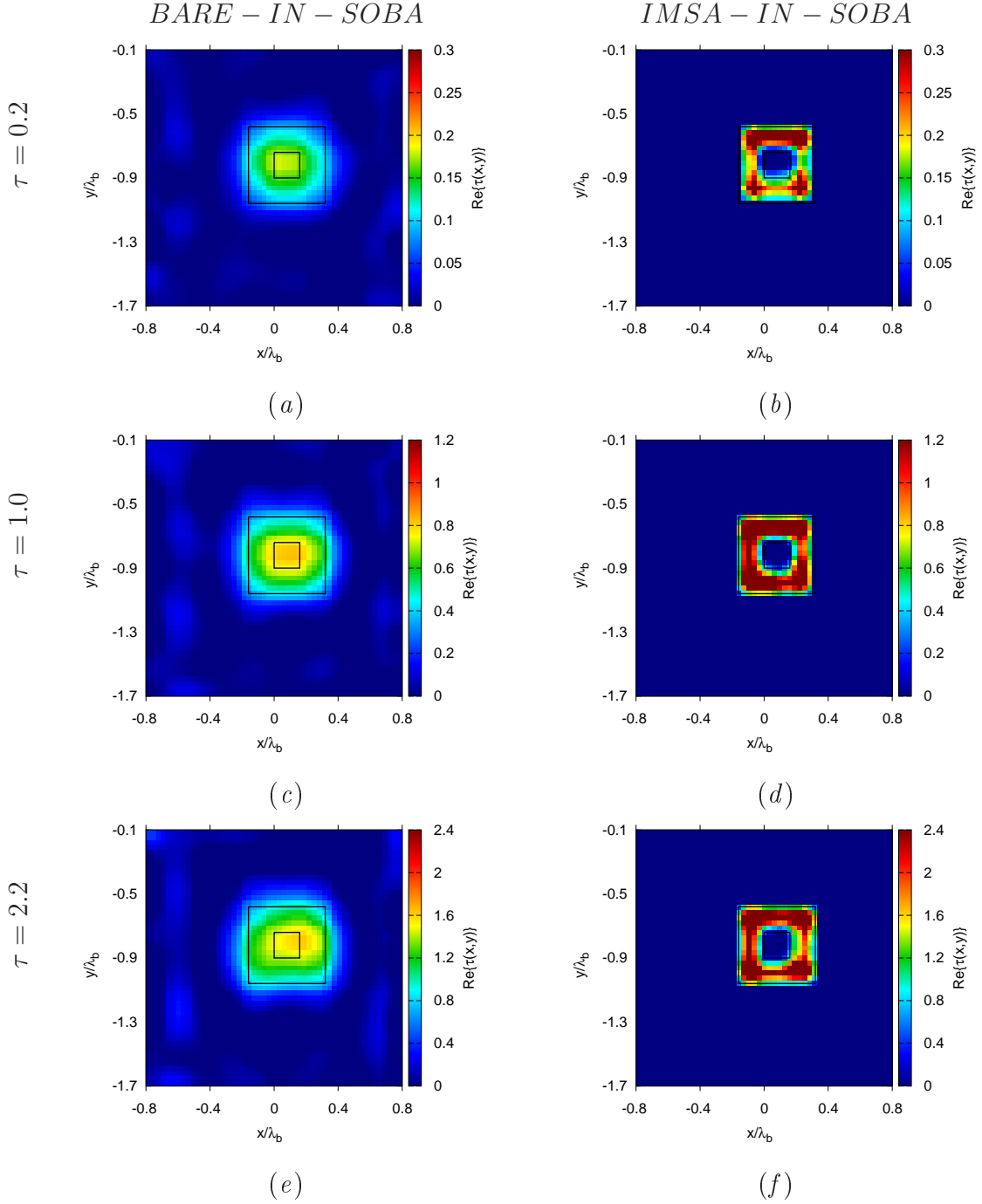
Figure 3.7: *Performance Assessment ("O-Shaped" Scatterer $\ell \approx \frac{\lambda_b}{2}$, $SNR = 20$
dB)* - Plot of the contrast profiles retrieved by $(a)(c)(e)$ $BARE - IN - SOBA$
and $(b)(d)(f)$ $IMSA - IN - SOBA$ when $(a)(b)$ $\tau = 0.2$, $(c)(d)$ $\tau = 1.0$, and
$(e)(f)$ $\tau = 2.2$.

To further confirm the above considerations and provide a qualitative picture

of the retrieved profiles, Fig. 3.7 shows a direct comparison between the reconstructions provided by both $BARE - IN - SOBA$ and $IMSA - IN - SOBA$ for different values of contrast [Figs. 3.7(a)-3.7(b) - $\tau = 0.2$, Figs. 3.7(c)-3.7(d) - $\tau = 1.0$, Figs. 3.7(e)-3.7(f) - $\tau = 2.2$], when $SNR = 20$ dB. As it can be observed, thanks to the increased level of resolution inside the correctly identified RoI, the $IMSA - IN - SOBA$ outperforms its "bare" counterpart, showing not only the capability of better retrieving the external boundaries of the scatterer, suppressing the undesired artifacts inside the background region, but also of recognizing position and shape of the internal cavity.

3.4.4 Inhomogeneous Cylinders

To assess the performances of the $IMSA - IN - SOBA$ when dealing with buried objects characterized by non-homogeneous dielectric distributions, this Section considers the analysis of the two reference profiles in Figs. 3.8(a)-3.8(b). The first inhomogeneous geometry (Fig. 3.8(a), "$Double$-L" cylinder) is characterized by $\tau_{up} = 0.5$ and $\tau_{low} = 1.5$ in the upper and lower portions, respectively, while the second reference distribution (Fig. 3.8(b), "$Concentric$" cylinder) is characterized by $\tau_{ext} = 0.5$ and $\tau_{in} = 1.0$. The second and third rows of Fig. 3.8 illustrate the retrieved dielectric distributions by the $BARE - IN - SOBA$ [Figs. 3.8(c)-(d)] and by the $IMSA - IN - SOBA$ [Fig. 3.8(e)-(f)], when $SNR = 20$ dB. As a matter of fact, the "bare" IN method implementation provides much more "smoothed" profiles than the multi-scaling scheme.

Considering the retrieved profiles for the "$Double$-L" scatterer, the improvement in terms of accuracy provided by the $IMSA - IN - SOBA$ [Fig. 3.8(e)] is confirmed by a remarkable reduction of the reconstruction error ($\Xi_{tot}^{BARE-IN-SOBA} \approx 1.03 \times 10^{-1}$ vs. $\Xi_{tot}^{IMSA-IN-SOBA} \approx 3.35 \times 10^{-2}$). Still considering this particular example, it is quite interesting to notice that the $BARE - IN - SOBA$ seems almost completely unable to identify the presence of two distinct geometrically adjacent distributions of the contrast [Fig. 3.8(c)].

Similar conclusions can be also formulated for the "$Concentric$" configuration [Figs. 3.8(d)-(f)]. Differently from the "bare" counterpart, the $IMSA - IN - SOBA$ correctly identifies the squared shape and the contrast of the inner core, as verified by the lower internal reconstruction error ($\Xi_{int}^{BARE-IN-SOBA} \approx 1.19 \times 10^{-1}$ vs. $\Xi_{int}^{IMSA-IN-SOBA} \approx 7.45 \times 10^{-2}$).

Besides the discussed aspects, it is important to remark that the improved accuracy showed by the $IMSA - IN - SOBA$ comes together with an increased computational efficiency, as emphasized by the evaluation of the inversion times on a standard laptop with 3.20 GHz CPU clock and 4GB of RAM memory. The total time required to obtain the reconstructions in Fig. 3.8 are $\Delta t^{IMSA-IN-SOBA} = 80$ [s] and $\Delta t^{IMSA-IN-SOBA} = 57$ [s] for "$Double$-L" and "$Concentric$" profiles, respectively, while the time required by the $BARE - IN - SOBA$ is $\Delta t^{BARE-IN-SOBA} = 256$ [s] for both distributions.
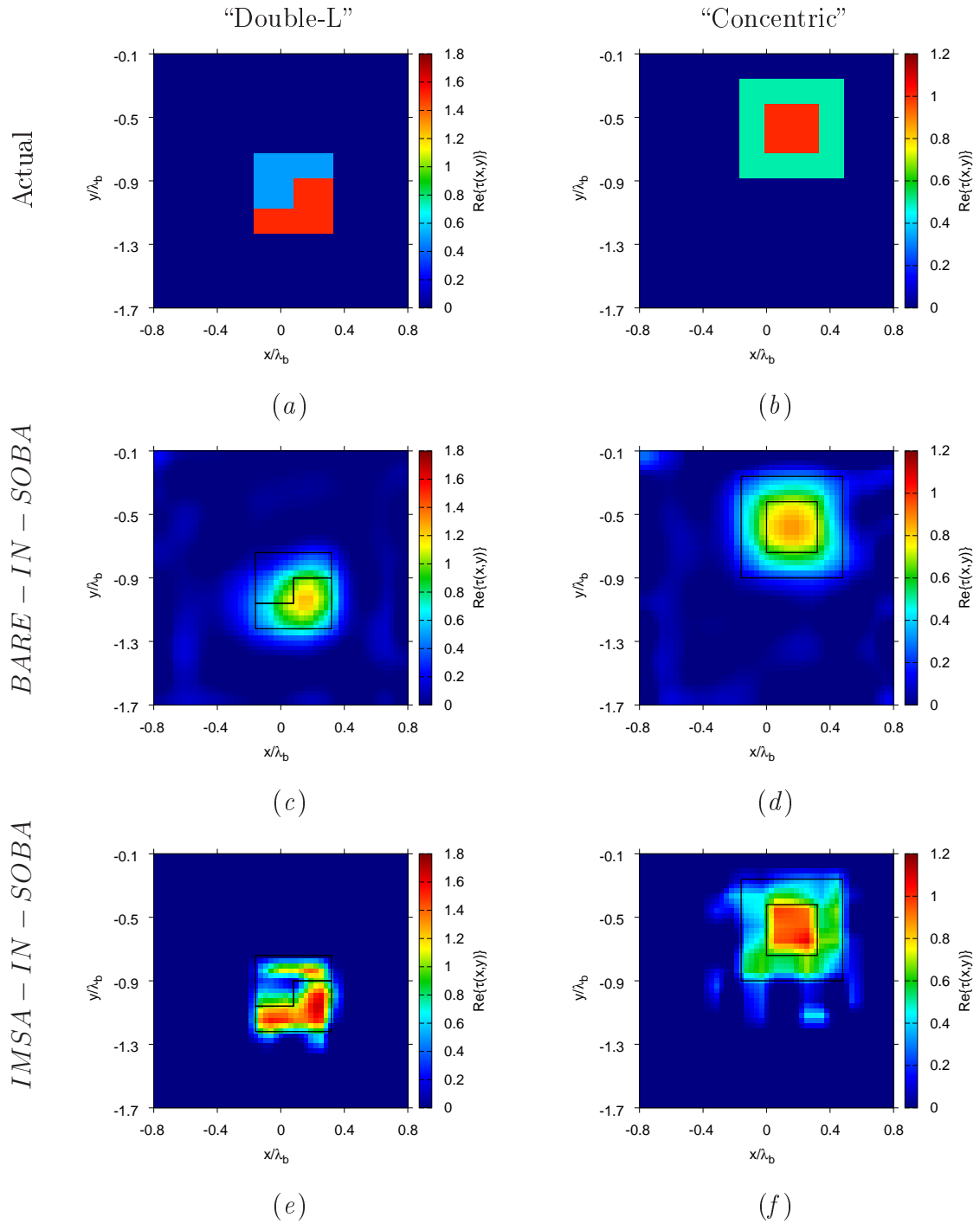
Figure 3.8: *Performance Assessment (Inhomogeneous Scatterers, $SNR = 20$
dB)* - Plot of the actual $(a)(b)$ and retrieved (c)-(f) contrast profiles by $(c)(d)$
$BARE-IN-SOBA$ and $(e)(f)$ $IMSA-IN-SOBA$ for $(a)(c)(e)$ "Double-L"
and $(b)(d)(f)$ "Concentric" targets.

3.4.5 "Square" Cylinder with strong conductivity

The last test case is aimed at further assessing whether the previously discussed performances of the $IMSA-IN-SOBA$ are still valid when the unknown object is characterized by a conductivity σ_c higher than the surrounding background medium. As for the previous results, the geometry and measurement setup of Sect. 3.4 have been maintained, while different values of conductivity $\sigma_c \geq \sigma_B = 10^{-2}$ have been considered for the "Square" cylinder in Fig. 3.3(a). Considering this specific test case, the real part of the scatter contrast is thus kept constant to $\mathcal{R}\{\tau\} = 1.5$, while the effect of considering different values of the imaginary part $\mathcal{I}\{\tau\} = \left[\frac{\sigma_B - \sigma_c}{2\pi f \varepsilon_0}\right]$ is hereinafter investigated. In order to give the reader a full overview of the effectiveness of the $IMSA-IN-SOBA$ and to provide a pictorial comparison in terms of accuracy with respect to the $BARE-IN-SOBA$, Fig. 3.9(a) depicts the behaviour of Ξ_{tot} as a function of the object conductivity σ_c.

In accordance to what has been already observed when considering different values of $\mathcal{R}\{\tau\}$ [Fig. 3.6], the error increases for both methods as the scatterer becomes stronger (i.e., the value of σ_c is increased with respect to the conductivity of the background medium). However, the error curves in Fig. 3.6 clearly highlight the advantages of the $IMSA-IN-SOBA$ when applied to the detection of buried scatterers with strong conductivity, whatever the considered SNR on measured field data. Moreover, the performance gap between the two implementations becomes even more evident as the value of σ_c is increased ($\Xi_{tot}^{BARE}\big|_{\sigma_c=10^{-2}} \approx 9.72 \times 10^{-2}$ vs. $\Xi_{tot}^{IMSA}\big|_{\sigma_c=10^{-2}} \approx 1.83 \times 10^{-2}$ and $\Xi_{tot}^{BARE}\big|_{\sigma_c=10^{-1}} \approx 3.12 \times 10^{-1}$ vs. $\Xi_{tot}^{IMSA}\big|_{\sigma_c=10^{-1}} \approx 7.33 \times 10^{-2}$, for $SNR = 20$ dB). For completeness, the retrieved distributions when $\sigma_c = 10^{-1}$ ($\mathcal{I}\{\tau\} = -5.39$) are also reported for both $BARE-IN-SOBA$ [Fig. 3.9(b)-(d)] and $IMSA-IN-SOBA$ [Fig. 3.9(c)-(e)], for blurred data with $SNR = 20$ dB. As confirmed by the presented outcomes, the linearization properties of the IN are enhanced when exploiting a multi-resolution approach intrinsically devoted to mitigate the undesired effects of a high-nonlinearity (e.g., the occurrence of local minima), as for the case of strong scatterers. The artifacts characterizing the reconstructions of the "bare" IN method (both present in the real [Fig. 3.9(b)] and imaginary [Fig. 3.9(d)] parts of the retrieved contrast) are almost completely suppressed by the $IMSA-IN-SOBA$, as verified by a reduction of the external error by an order of magnitude ($\Xi_{ext}^{BARE-IN-SOBA}\big] \approx 1.73 \times 10^{-1}$ vs. $\Xi_{ext}^{IMSA-IN-SOBA}\big] \approx 2.25 \times 10^{-2}$). Moreover, the total inversion time needed by the multi-zooming technique is significantly reduced when compared to the single-step counterpart ($\Delta t^{BARE-IN-SOBA} = 259$ [s] vs. $\Delta t^{IMSA-IN-SOBA} = 79$ [s]).

(a)

$BARE - IN - SOBA$ $IMSA - IN - SOBA$

(b)   (c)

(d)   (e)
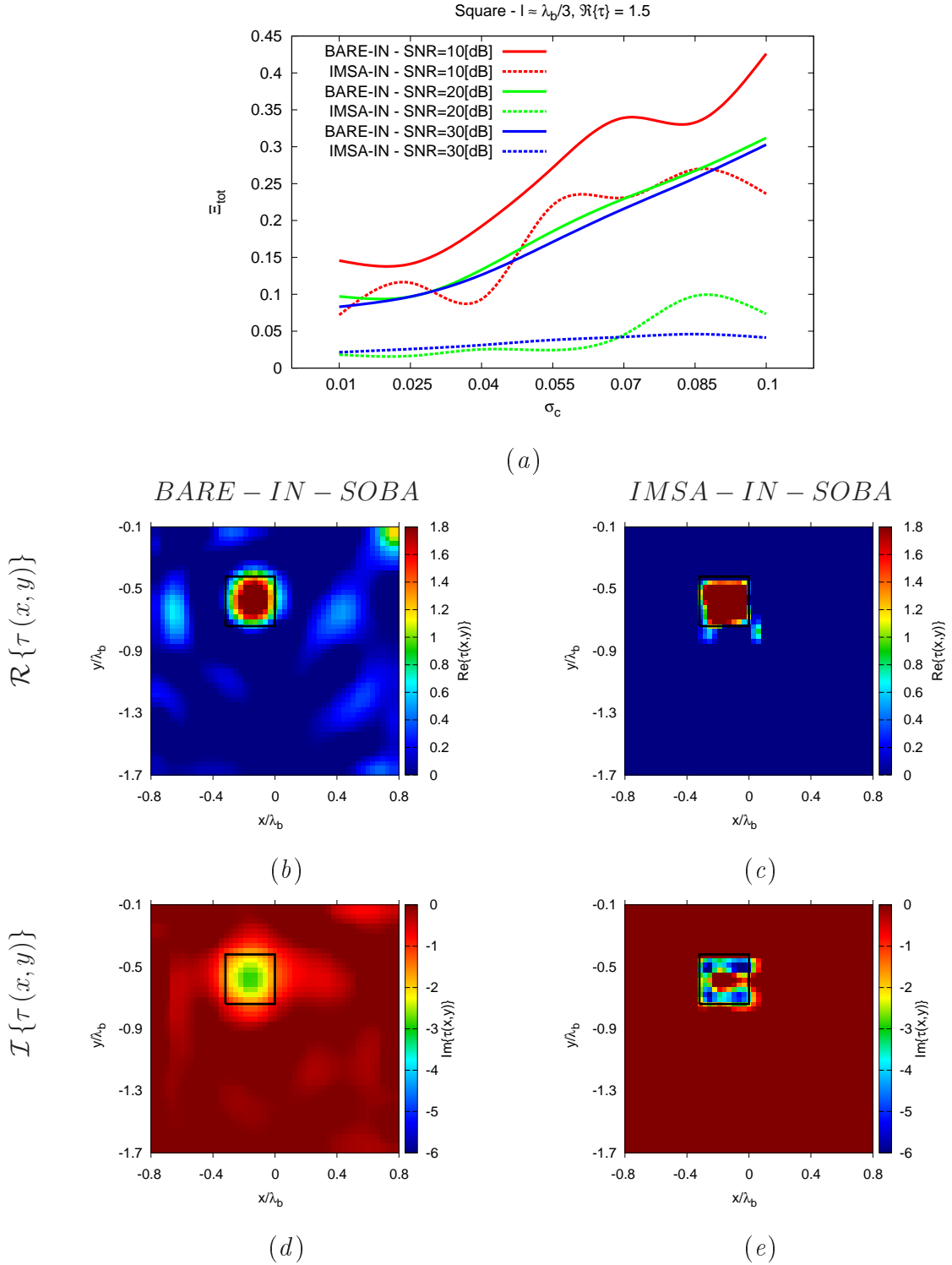
Figure 3.9: *Performance Assessment (Homogeneous Square Scatterer* - $\ell \approx \frac{\lambda_b}{3}$, $\mathcal{R}\{\tau\} = 1.5$, $SNR \in [10, 30]$ dB*)* - Behaviour of the Ξ_{tot} as a function of σ_c (*a*). Plot of the real (*b*)(*c*) and imaginary (*d*)(*e*) parts of the contrast profiles retrieved by (*b*)(*d*) $BARE - IN - SOBA$ and (*c*)(*e*) $IMSA - IN - SOBA$ when $SNR = 20$ dB.

31

3.5 Discussions

In this chapter, a new microwave imaging method for subsurface prospecting has been proposed. The approach combines a multi-focusing strategy with a regularization solution based on the use of an inexact-Newton method. In particular, the inverse problem has been addressed by numerically solving the Lippmann-Schwinger equation under the second-order Born approximation ($SOBA$). The proposed reconstruction method has been validated through an extended set of numerical results involving different types of scatterers and noise conditions. Simulations have highlighted the following key results:

- the proposed technique is able to profitably combine the well assessed regularization capabilities of the adopted local search technique (the inexact-Newton method) with the enhanced exploitation of available information provided by the multi-focusing strategy, which is able to reduce the problem of local minima arising from the *non-linearity* of the involved set of equations.

- Moreover, the combined strategy exhibits advantages over its standard "bare" implementation in terms of achieved accuracy and resolution, whatever the contrast distribution (homogeneous/inhomogeneous), the cross-section geometry and the noise level on measured data.

- Furthermore, the proposed multi-focusing approach overcomes the standard "bare" implementation also in terms of the computational efficiency, thanks to the significant reduction of the problem unknowns at each iterative step, which arises from the use of an adaptive coarse-to-fine discretization of the investigation areas at different levels of resolution.

Chapter 4

Electromagnetic Subsurface Prospecting by a Fully Nonlinear Multi-focusing Inexact Newton Method

In this chapter, an electromagnetic inverse scattering procedure for the reconstruction of shallow buried objects in a homogeneous half-space is proposed. The approach is based on the numerical solution of the integral equations modelling the inverse scattering relationships and it extends to strong scatterers the imaging capabilities of the approach presented in Chapter 3 relying on approximated formulations (i.e., the $SOBA$). The inversion is based on the synergic application of a multi-focusing strategy based on the iterative multi-scaling approach ($IMSA$) along with an efficient regularization scheme based on the inexact-Newton (IN) method. Numerical results corroborate the mathematical description to assess capabilities and current limitations of the proposed fully-nonlinear technique.

4.1 Introduction and motivation

Microwave methods for retrieving buried objects are a key topic of the research area concerned with inversion methods as confirmed by the scientific literature [1]-[4]. Applications range from civil and industrial non-destructive testing [6]-[9] to medical imaging [10]-[12] as well as geophysical applications [13]-[18]. As for these latter, inverse scattering techniques have been widely proposed for the shallow investigation of the Earth's subsurface to extend/better-exploit the capabilities/features of ground penetrating radars (GPRs) [13]-[19]. However, despite several and important results, microwave methods are still quite challenging and far from a real-life use mainly due to the ill-posedness and the nonlinearity of the mathematical relationships that relate the scattered fields to the unknown distributions of the dielectric parameters of the investigation region. Moreover, the information content available from scattered-field data is low [70], especially when dealing with aspect-limited configurations such as those in subsurface prospecting, leading to a reduced data diversity [20]. To properly address these issues, many inversion strategies, both stochastic [34][36][37][40][42][62][71] and deterministic [26][32][63]-[68], have been proposed along with approximate models (e.g., based on Rytov [48] and [26] Born linearizations).

In a recent paper, the authors have introduced the use of a multi-focusing approach associated with an inexact-Newton (IN) method [48]. Indeed, the use of multi-resolution methods has been found to be an effective way to reduce the number of local minima arising in electromagnetic inverse problems due to the severe ill-posedness of the integral equations at hand [54][72]. On the other hand, the IN method has proven to be a regularization approach efficient in several electromagnetic applications, mainly related to tomography in free-space conditions [44][43]. In Chapter 3, the synergic combination of the two methods has been exploited in an effective approach for the reconstruction of buried targets in a shallow subsurface under the second-order Born approximation ($SOBA$) condition [73] by assuming the scattering field nonlinearly depending on the dielectric parameters of the object under test, but independent on the internal total electric field. While such an approximation resulted in a non-negligible computational saving because of the reduction of the problem unknowns (i.e., the dielectric distribution only), the reliability of the reconstruction turns out limited to weak scatterers. Moreover, it is worth pointing out that in practical applications the $SOBA$ extends only partially the range of retrievable dielectric permittivities compared to the classic first order Born approximation where the scattered electric field is expressed in terms of the known incident field (i.e., the field radiated by the source in the background without the unknown scatterer).

In this chapter, the integrated multi-focusing-IN ($IMSA-IN$) strategy is applied for the first time to the exact equations of the inverse scattering problem for buried objects by extending the range of validity of the formulation presented in Chapter 3 as well as the possibility to retrieve strong scatterers. The outline of

the chapter is as follows. In Sect. 4.2, the approach is mathematically described. Section 4.3 reports representative results from several numerical simulations devoted to validate the proposed approach illustrating its potentials and current limitations. Finally, some conclusions are drawn (Sect. 4.4).

4.2 Mathematical formulation

Let us consider the same cylindrical geometry already considered in Chapter 3 whose description is just summarized here. By assuming transmitting and measurement points arranged in a cross-borehole configuration (Fig. 4.1), let V be the set of time-harmonic line currents that generate the incident fields probing the investigation region D_{inv}. For each v-th illumination, the longitudinal component of the scattered electric field vector is collected at M measurements locations ($D_{obs}^{(v)}$, $v = 1, ..., V$, being the set of measurement points at the v-th view).
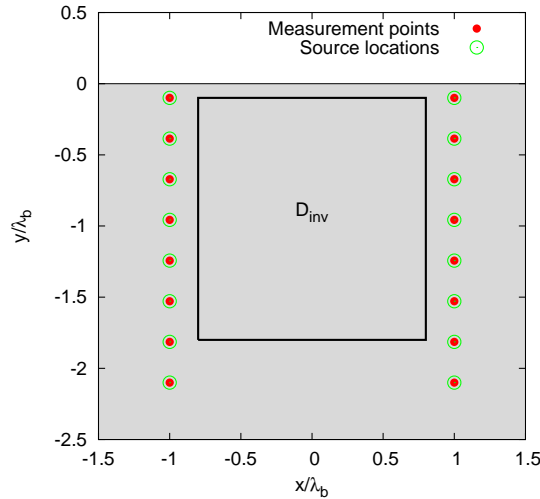
Figure 4.1: Cross-borehole imaging configuration.

To retrieve the unknown dielectric properties of the investigation domain, the inverse scattering problem mathematically described in terms of the following two integral equations of first- (called "*state equation*") and second-kind (called "*data equation*"), respectively [2],

$$E_{tot}^{(v)}(x,y) = E_{inc}^{(v)}(x,y) + k_B^2 \int_{D_{inv}} \tau(x',y') E_{tot}^{(v)}(x',y') \mathcal{G}_{int}(x,y,x',y') \, dx'dy'$$
$$(x,y) \in D_{inv}$$

$$(4.1)$$

$$E_{scatt}^{(v)}(x,y) = k_B^2 \int_{D_{inv}} \tau(x',y') E_{tot}^{(v)}(x',y') \mathcal{G}_{ext}(x,y,x',y') \, dx'dy'$$
$$(x,y) \in D_{obs}^{(v)}$$
$$(4.2)$$

need to be solved. In (4.1) and (4.2), $E_{tot}^{(v)}$, $E_{inc}^{(v)}$, and $E_{scatt}^{(v)}$ denote the z-components of the total, incident, and scattered field vectors for the v-th view, respectively. Moreover, $\mathcal{G}_{ext}$ is the Sommerfeld's Green's function for the half space [55], while the contrast function τ is defined in equation (2.2).

Unlike the theory presented in Chapter 3, where the $SOBA$ approximated formulation has been assumed, the two scattering equations are contemporarily exploited to inspect buried strong scatterers. Towards this end, let us put (4.1) and (4.2) in a functional form as

$$A^{(v)} \left(\tau; E_{tot}^{(v)} \right) = b^{(v)} \quad v = 1, ..., V \tag{4.3}$$

where $b^{(v)}$ includes the known terms (i.e., the incident field in the *state equation* and the measured scattered electric field in the *data equation*)

$$b^{(v)} = \begin{bmatrix} E_{scatt}^{(v)} \\ E_{inc}^{(v)} \end{bmatrix}, \tag{4.4}$$

and let us combine the V equations (4.3) to recast the inverse problem as the solution of the following functional equation

$$A^{(v)} \left(\tau; E_{tot}^{(1)}, ..., E_{tot}^{(V)} \right) = \begin{bmatrix} E_{scatt}^{(1)} \\ E_{inc}^{(1)} \\ \vdots \\ E_{scatt}^{(V)} \\ E_{inc}^{(V)} \end{bmatrix} = \begin{bmatrix} b^{(1)} \\ \vdots \\ b^{(V)} \end{bmatrix}. \tag{4.5}$$

By discretizing (4.5) with square sub-domains and point matching, a nonlinear systems of discrete equations is yielded

$$\mathbf{A} \left(\boldsymbol{\tau}; \mathbf{E}_{tot} \right) = \mathbf{b} \tag{4.6}$$

where $\boldsymbol{\tau}$ is an array whose n-th entry $(n = 1, ..., N)$ is the value of the contrast function at the n-th sub-domain in which the investigation domain D_{inv} has been partitioned, $\mathbf{E}_{tot}$ is an array containing the $V \times N$ values of the electric field in the investigation area, and $\mathbf{b}$ is an array of size $V \times (N + M)$ containing the values of the known samples of the incident and scattered electric fields (see *Appendix* A).

To properly and efficiently solve (4.6), some challenging computational issues have to be carefully addressed. To reduce the computational burden and therefore focusing the attention only on parts of the investigation domain where scatterers are supposed to be present, the *IMSA* approach is adopted. Such a multi-focusing technique has been firstly developed by *A. Massa* and co-workers in [54] and successively deeply analyzed in other papers [48][72][74][75]. At each step

of the *IMSA* ($s = 1, ..., S$), a zoomed investigation domain Ω_s, composed by the combination of the region of interests defined at step $s - 1$, is considered (Ω_1 coincides with the whole investigation area - see Fig. 4.1). Equation (4.6) is then solved by using the *IN* method [44][43] for reconstructing the distributions of the dielectric properties in Ω_s. Such an inversion method is composed by two nested loops. In the external loop, (4.6) is first linearized by means of a Newton approximation, whereas the resulting linear system of equations is solved in a regularized sense with a truncated Landweber method [61]. A maximum number of iterations, $I_{max,s}$, is set for the external loop, while the number of iterations, Q, of the inner loop is fixed for any reconstruction process. A complete discussion on the application of the *IN* method can be found in [45] where it has been shown that the number of external iterations plays the role of a regularization parameter controlling the so-called semi-convergence. Therefore, it is necessary to define a suitable strategy for terminating the iterations in order to guarantee convergence towards the global solution of the functional problem at hand. To this end, let us first define the following residual function

$$\Phi_s^i = \frac{\sum_{v=1}^{V} \sum_{m=1}^{M} \left| E_{scatt}^{(v)} \left(x_m^{(v)}, y_m^{(v)} \right) - E_i^{(v)} \left(x_m^{(v)}, y_m^{(v)} \right) \right|}{\sum_{v=1}^{V} \sum_{m=1}^{M} \left| E_{scatt}^{(v)} \left(x_m^{(v)}, y_m^{(v)} \right) \right|} \tag{4.7}$$

where $E_{scatt}^{(v)} \left(x_m^{(v)}, y_m^{(v)} \right)$ denotes the scattered field component measured at the m-th measurement point $\left(x_m^{(v)}, y_m^{(v)} \right)$ ($m = 1, ..., M$) for the v-th illumination ($v = 1, ..., V$), and $E_i^{(v)} \left(x_m^{(v)}, y_m^{(v)} \right)$ indicates the same quantity estimated at the i-th iteration of the imaging process. Then, at each *IMSA* step, s ($s > 1$), the *IN* solver is stopped when one of the following conditions holds true:

- the fitness goes below the threshold computed at the step s (i.e., $\phi_s^i \leq \phi_s^{th}$);

- the number of outer iterations reaches its maximum (i.e., $I_{max,s>1}$).

As for the threshold at the s-th step, Φ_s^{th}, it is obtained as

$$\Phi_s^{th} \leq \alpha \phi_{s-1}^{final}, \quad s = 2, ..., S \tag{4.8}$$

where Φ_{s-1}^{final} is the final residual at the step $s-1$, α is a setup scaling factor, and S is the total number of *IMSA* steps. Concerning the first *IMSA* step ($s = 1$), the stopping criterion is only determined by the user-defined number of outer iterations (i.e., $I_{max,s=1}$).

4.3 Numerical Results

The proposed approach has been validated by means of several numerical simulations referring to the following benchmark scenario. The investigation area

has been chosen as a square domain of side $1.6\,\lambda_b$ centered at $(0.0,\ -0.9\,\lambda_b)$ with the dielectric properties of the lower half space set to $\varepsilon_{rB} = 4.0$ and $\sigma_B = 0.01$ S/m. A set of $V = 16$ TX/RX antennas, modeled as line-current sources with unit amplitude, has been considered at a working frequency of 300 MHz. The antennas have been supposed to be located into two boreholes beside D_{inv} (as shown in Fig. 4.1) at positions

$$(x_v, y_v) = \begin{cases} \left(-\lambda_b,\ -0.1\,\lambda_b - 2\,\lambda_b \frac{v-1}{\frac{v}{2}-1}\right) & \text{if}\quad v \leq \frac{V}{2} \\ \left(-\lambda_b,\ -0.1\,\lambda_b - 2\,\lambda_b \frac{v--\frac{v}{2}-1}{\frac{v}{2}-1}\right) & \text{if}\quad v > \frac{V}{2} \end{cases},\quad v = 1,...,V. \quad (4.9)$$

When a radiator acted as transmitter, the remaining $M = V - 1$ collected the scattered electric field. The number of views and measurement points has been chosen as suggested in [57][58].

The scattering field samples (i.e., the data of the inversion procedure) have been numerically computed by using a forward solver based on the Method of Moments [76] with a mesh of $N_{fwd} = 40 \times 40$ square subdomains. To simulate a more realistic measurement setup, a Gaussian noise with zero mean value has been added to the computed data. Unless otherwise specified, the signal-to-noise ratio on the total electric field data has been set to $SNR = 20$ dB. As for the inversion procedure, a coarser mesh has been used to avoid inverse crimes. More in detail, $N_{inv}^{IMSA} = 10 \times 10$ subdomains have been adopted at each s-th scaling step of the IMSA, whereas the number of partitions has been set to $N_{inv}^{bare} = 20 \times 20$ pixels for the bare IN approach.

To quantitatively evaluate the performance of the approach, the same error figures used in Chapter 3 have been adopted and are here reported, for completeness

$$\Xi_{reg} = \frac{1}{N_{reg}} \sum_{n=1}^{N_{reg}} \frac{|\hat{\tau}(x_n, y_n) - \tau(x_n, y_n)|}{|\tau(x_n, y_n) + 1|} \quad reg = tot, ext, int \qquad (4.10)$$

where τ and $\hat{\tau}$ are the actual and reconstructed values of the contrast function in the n-th sub-domain[1] and N_{reg} indicates the number of cells covering the whole inspected area D_{inv} ($reg = tot$, $N_{tot} = N$), or belonging to the background region ($reg = ext$), or to the support of the buried scatterer ($reg = int$; $N_{tot} = N_{ext} + N_{int}$).

---

[1]The reconstructions have been obtained by averaging the results over 100 different noise realizations.

4.3.1 Calibration

Figure 4.2: *Calibration (Square Scatterer -* $L = 0.32\,\lambda_b$, $(x_c = -0.16\,\lambda_b$, $y_c = -0.58\,\lambda_b)$, $\varepsilon_r = 5.5$, $\sigma = 0.01$ S/m $[\tau = 1.5]$, $\varepsilon_{rB} = 4.0$, $\sigma_B = 0.01$ S/m, $SNR = 20$ dB) - Actual target used for the algorithm calibration.

As already stated in Chapter 3, the choice of the correct parameters of the inversion procedure is of fundamental importance, thus an analysis of the performances versus such parameters has been firstly performed to identify the best setup. The goal of this calibration has been that of determining the optimal (Q, α) pair for the *IMSA-IN* approach, while the other parameters have been set according to the guidelines already devised in previous works [43][69], namely $I_{max,s=1} = 20$, $I_{max,s>1} = 1000$, and $S = 4$. More in detail, Q and the fitness scaling factor α have been varied within the range $10 - 100$ and between 0.1 and 0.9, respectively. As a reference target, a square cylinder located at $(-0.16\,\lambda_b, -0.58\,\lambda_b)$ with side $L = 0.32\,\lambda_b$, relative dielectric permittivity $\varepsilon_r = 5.5$, and electric conductivity $\sigma = 0.01$ S/m (i.e., $\tau = 1.5$) has been considered (Fig. 4.2).

Figure 4.3: *Calibration* (*Square Scatterer* - $L = 0.32\,\lambda_b$, ($x_c = -0.16\,\lambda_b$, $y_c = -0.58\,\lambda_b$), $\varepsilon_r = 5.5$, $\sigma = 0.01$ S/m [$\tau = 1.5$], $\varepsilon_{rB} = 4.0$, $\sigma_B = 0.01$ S/m, $SNR = 20$ dB) - Total reconstruction error vs. α ($\alpha \in [0.1, 0.9]$) for different values of Q in the range $Q \in [10, 100]$.

Figure 4.4: *Calibration* (*Square Scatterer* - $L = 0.32\,\lambda_b$, ($x_c = -0.16\,\lambda_b$, $y_c = -0.58\,\lambda_b$), $\varepsilon_r = 5.5$, $\sigma = 0.01$ S/m [$\tau = 1.5$], $\varepsilon_{rB} = 4.0$, $\sigma_B = 0.01$ S/m, $SNR = 20$ dB) - Best fitness value for different (Q, α) pairs.

(a)

(b)

Figure 4.5: *Calibration (Square Scatterer* - $L = 0.32\,\lambda_b$, $(x_c = -0.16\,\lambda_b$, $y_c = -0.58\,\lambda_b)$, $\varepsilon_r = 5.5$, $\sigma = 0.01$ S/m $[\tau = 1.5]$, $\varepsilon_{rB} = 4.0$, $\sigma_B = 0.01$ S/m, $SNR = 20$ dB) - (a) Real and (b) imaginary parts of the reconstructed distribution of the contrast function when $Q = Q^{opt} = 50$ and $\alpha = \alpha^{opt} = 0.9$.

The results of the *IMSA-IN* reconstructions are summarized in Fig. 4.3, which reports the values of the total error Ξ_{tot} versus the fitness scaling factor and for different values of the inner iterations of the *IN* algorithm when setting $I_{max,s=1} = 20$ and $S = 4$, being $SNR = 20$ dB. Since the best pair of parameters is defined as that with the minimum value of the total reconstruction error Ξ_{tot},

41

the optimal setup turned out to be: $Q = 50$ and $\alpha = 0.9$. For completeness, Figure 4.4 reports the values of the residual Φ on the data, while Figure 4.5 shows the distribution of the contrast function [real part - Fig. 4.5(a); imaginary part - Fig. 4.5(b)] reconstructed with the optimal parameters.

As it can be observed, the scatterer is faithfully reconstructed with a careful identification of the target shape as well as an estimation of the contrast very close to the actual one.

Figure 4.6: *Calibration (Square Scatterer* - $L = 0.32\,\lambda_b$, ($x_c = -0.16\,\lambda_b$, $y_c = -0.58\,\lambda_b$), $\varepsilon_r = 5.5$, $\sigma = 0.01$ S/m [$\tau = 1.5$], $\varepsilon_{rB} = 4.0$, $\sigma_B = 0.01$ S/m, $SNR = 20$ dB) - Reconstruction errors for different values of $\Delta\varepsilon_{rB}$.

To assess the robustness of the optimal calibration setup against the uncertainties in the medium electromagnetic parameters, the same target has been imaged by assuming that the relative dielectric permittivity $\widehat{\varepsilon}_{rB}$ used by the inversion method is different from its actual value ε_{rB}. The behaviour of the total reconstruction error versus $\Delta\varepsilon_{rB} \triangleq \varepsilon_{rB} - \widehat{\varepsilon}_{rB}$ shows that the accuracy of the proposed approach smoothly degrades as the uncertainty increases (e.g., $\frac{\Xi_{tot}|_{\Delta\varepsilon_{rB}=0.8}}{\Xi_{tot}|_{\Delta\varepsilon_{rB}=0.2}} \approx 2.83$ - Fig. 4.6), and that the total error is below 7% even in the worst case conditions (i.e., when $\Delta\varepsilon_{rB} \approx -1.0$ - Fig. 4.6).

4.3.2 Effects of Noise

To evaluate the effect of the noise on the reconstructions and the robustness of the proposed approach, a set of simulations with levels of noise varying from $SNR = 5$ dB down to ∞ has been performed.

SNR	I_{tot}	Φ^{final}	Ξ_{tot}	Ξ_{int}	Ξ_{ext}	Δt [s]
			$BARE$			
∞ (Noiseless)	600	1.28×10^{-3}	9.46×10^{-2}	2.17×10^{-1}	6.94×10^{-2}	4041
30 [dB]	600	1.80×10^{-3}	9.44×10^{-2}	2.17×10^{-1}	7.04×10^{-2}	4045
20 [dB]	600	4.07×10^{-3}	9.83×10^{-2}	2.21×10^{-1}	7.25×10^{-2}	4042
10 [dB]	600	1.25×10^{-2}	1.35×10^{-1}	2.17×10^{-1}	1.00×10^{-1}	4038
5 [dB]	600	2.20×10^{-2}	1.91×10^{-1}	2.31×10^{-1}	1.37×10^{-1}	4023
			$IMSA$			
∞ (Noiseless)	450	4.45×10^{-3}	5.61×10^{-3}	1.36×10^{-1}	0.00	211
30 [dB]	461	4.53×10^{-3}	5.60×10^{-3}	1.36×10^{-1}	0.00	212
20 [dB]	827	5.39×10^{-3}	2.89×10^{-3}	6.87×10^{-2}	0.00	288
10 [dB]	3020	1.41×10^{-2}	5.21×10^{-3}	1.17×10^{-1}	0.00	795
5 [dB]	3020	2.43×10^{-2}	1.46×10^{-2}	1.97×10^{-1}	5.96×10^{-3}	776

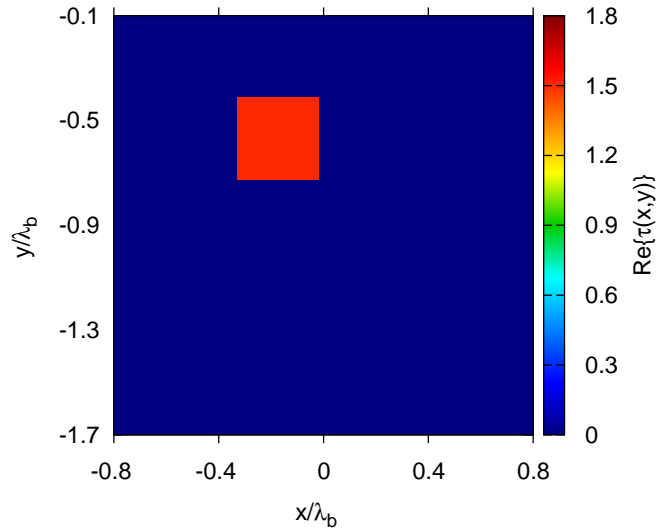Table 4.1: *Performance vs. Noise (Square Scatterer - $L = 0.32\,\lambda_b$, ($x_c = -0.16\,\lambda_b$, $y_c = -0.58\,\lambda_b$), $\varepsilon_r = 5.5$, $\sigma = 0.01$ S/m [$\tau = 1.5$], $\varepsilon_{rB} = 4.0$, $\sigma_B = 0.01$ S/m) - Total number of performed outer iterations, final fitness values, and reconstruction errors for the BARE and the IMSA ($s = S = 4$) IN approaches. Total execution time on a PC with Intel(R) Core(TM)2 CPU 6600 @ 2.40GHz, 2GB RAM.*

Still considering the same target of the previous Section, the inversion results are summarized in Tab. 4.1 where the total number of outer iterations needed to reach the convergence[2], the final residual on the data Φ^{final}, and the reconstruction errors Ξ_{reg} are given along with the inversion time[3]. For comparison purposes, the outcomes from the application of the bare *IN* approach (i.e., the single-step uniform resolution *IN*) is also reported. It is worth noticing that for a fair comparison, the calibration of the control parameters has been carried out for the bare algorithm, as well, with the identification of the following optimal values: $I_{max} = 600$ and $Q = 100$.

As it can noticed (Tab. 4.1), the *IMSA-IN* approach proves to be quite robust to the noise on the data since, even for heavy noise conditions, the arising errors turns out to be quite small and the multi-resolution implementation always outperforms its corresponding single-step uniform resolution counterpart. These indications are also confirmed by the reconstructed distributions of the contrast function (real part - Fig. 4.7; imaginary part - Fig. 4.8).

---

[2]As for the *IMSA*, this number corresponds to the sum of the outer iterations performed on the whole set of iterative scaling steps.

[3]The *IMSA* inversion time is computed as the sum of the execution time for each iterative scaling step.
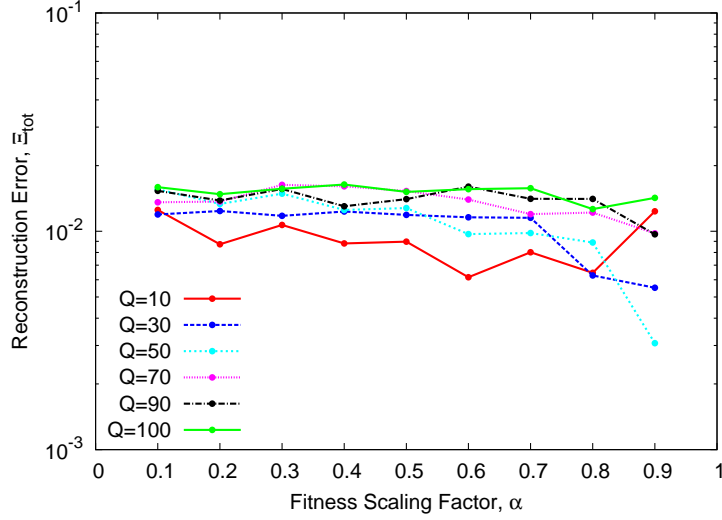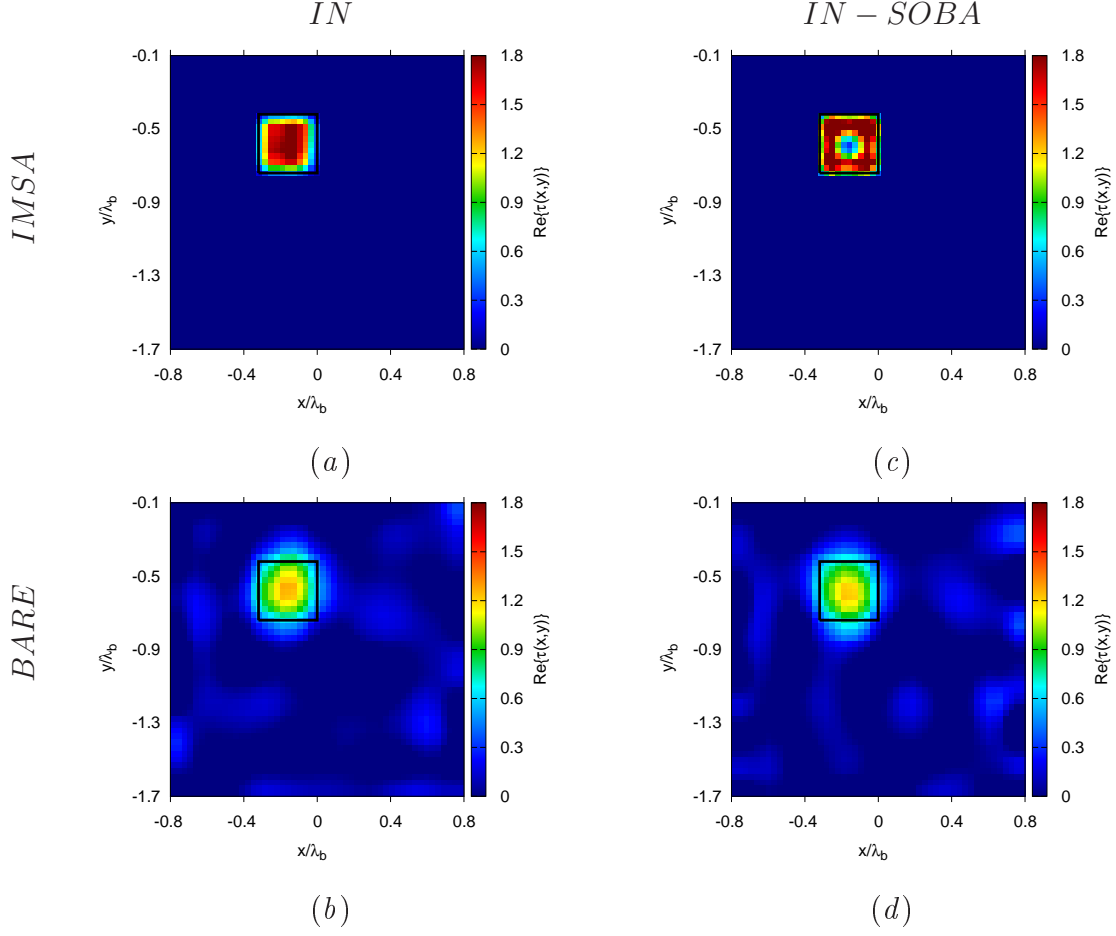
Figure 4.7: *Performance vs. Noise* (*Square Scatterer* - $L = 0.32\,\lambda_b$, ($x_c = -0.16\,\lambda_b$, $y_c = -0.58\,\lambda_b$), $\varepsilon_r = 5.5$, $\sigma = 0.01$ S/m [$\tau = 1.5$], ε_{rB} =4.0, σ_B =0.01 S/m, SNR =10 dB) - Reconstructed distributions of the contrast function (real part) when using (a)(c) *IMSA-IN* and (b)(d) *IN* under (a)(b) full-nonlinear and (c)(d) approximate conditions (*SOBA*).

As a representative example, let us refer to the plots in Fig. 4.7 concerned with the inversion of scattering data blurred with a noise characterized by $SNR = 10$ dB. In particular, Figures 4.7(a) and 4.8(a) show the result yielded with the *IMSA-IN* algorithm, while Figures 4.7(b) and 4.8(b) plot the reconstruction from the bare approach. Figures 4.7(c)-4.7(d) and 4.8(c)-4.8(d) complete the overview by presenting the results under second order Born approximation (i.e., *SOBA* method). As expected, the *IMSA-IN* better shapes the target and the estimated values of the contrast function are closer to the actual ones. On the other hand, the full-approach significantly improves the performance of the approximated one in both *IMSA* [Fig. 4.7(a) vs. Fig. 4.7(c) - $\Xi_{tot}^{IMSA-IN} = 5.21 \times 10^{-3}$ vs. $\Xi_{tot}^{IMSA-SOBA} = 1.83 \times 10^{-2}$] and single-step [Fig. 4.7(b) vs. Fig. 4.7(d) - $\Xi_{tot}^{IN} = 1.35 \times 10^{-1}$ vs. $\Xi_{tot}^{SOBA} = 1.46 \times 10^{-1}$] versions.
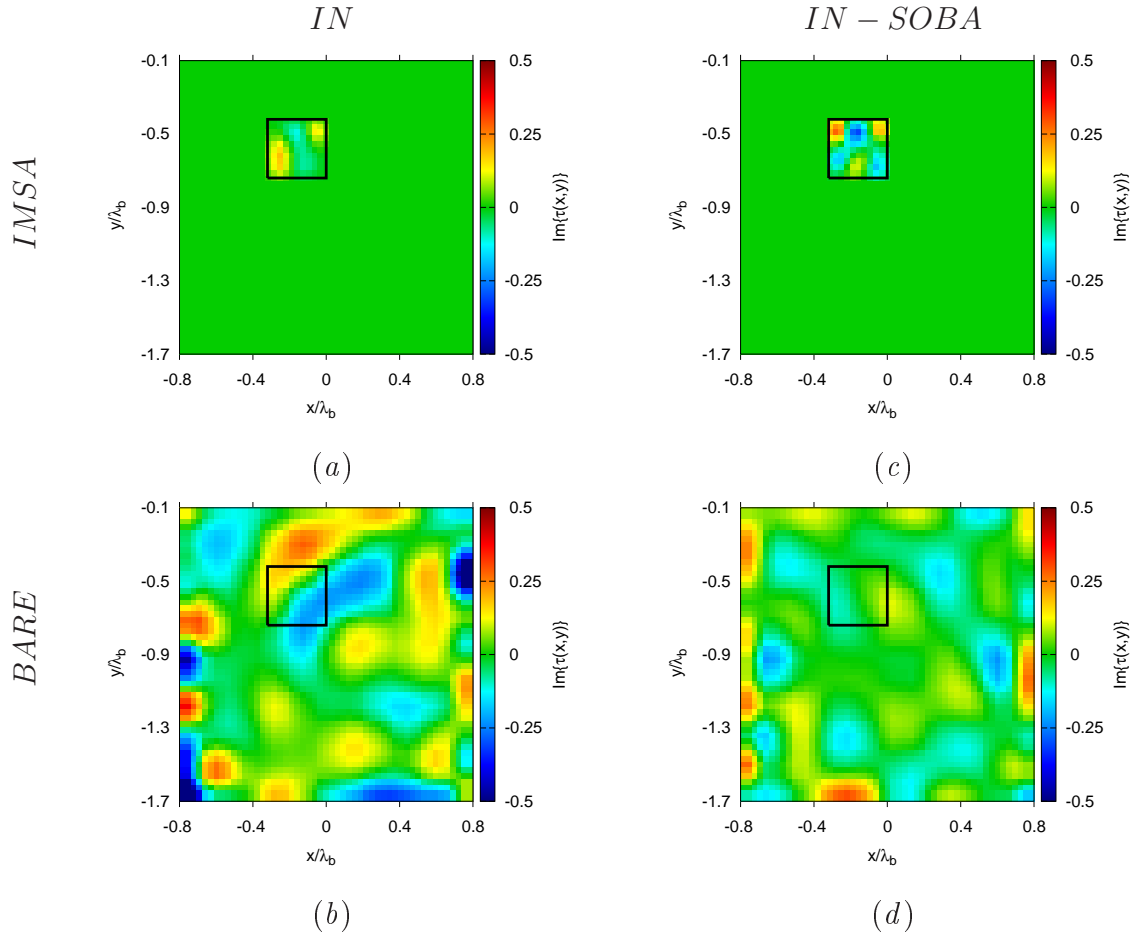
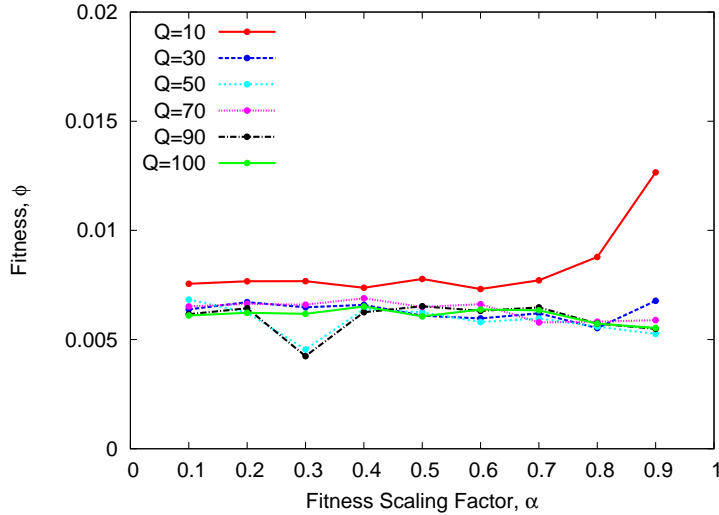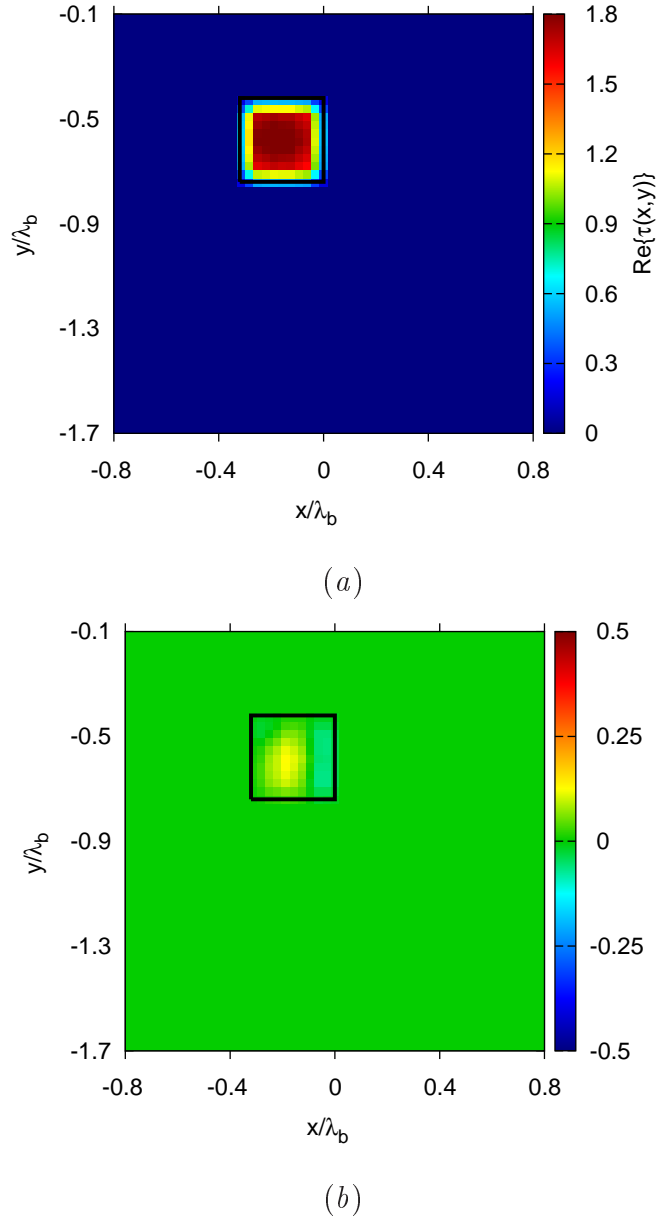Figure 4.8: *Performance vs. Noise* (*Square Scatterer* - $L = 0.32\,\lambda_b$, ($x_c = -0.16\,\lambda_b$, $y_c = -0.58\,\lambda_b$), $\varepsilon_r = 5.5$, $\sigma = 0.01$ S/m [$\tau = 1.5$], $\varepsilon_{rB} = 4.0$, $\sigma_B = 0.01$ S/m, $SNR = 10$ dB) - Reconstructed distributions of the contrast function (imaginary part) when using (a)(c) *IMSA-IN* and (b)(d) *IN* under (a)(b) full-nonlinear and (c)(d) approximate conditions (*SOBA*).

For completeness, Figures 4.9(a)-4.9(b) show the residual on the data and the reconstruction errors versus the outer iteration number, while the behavior of the reconstruction errors at each resolution step of the scaling process is reported in Fig. 4.9(c). As it can be observed, the multi-resolution procedure allows a significant improvement of the reconstruction quality throughout the iterative zooming.
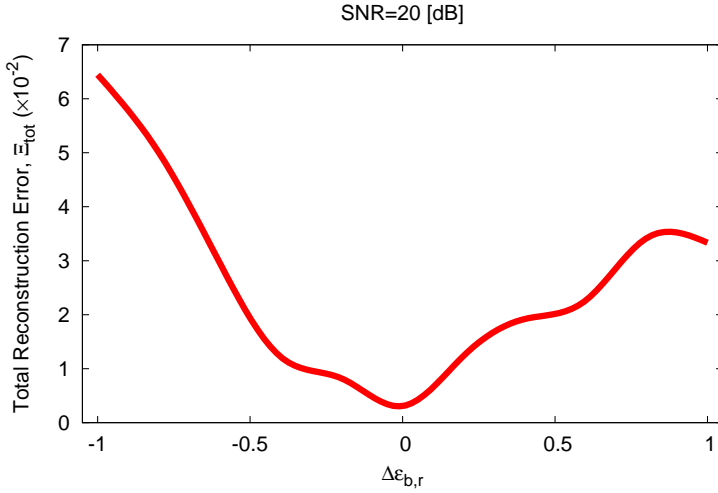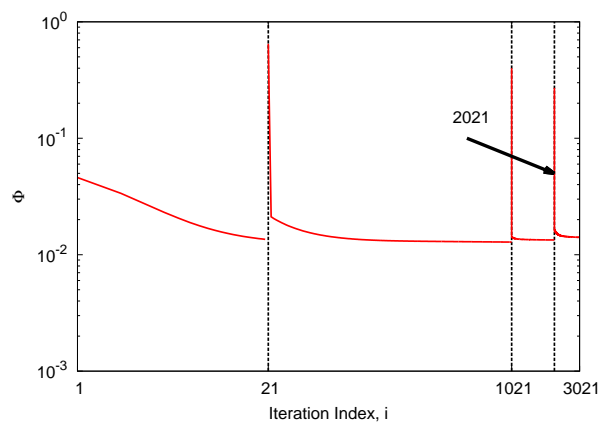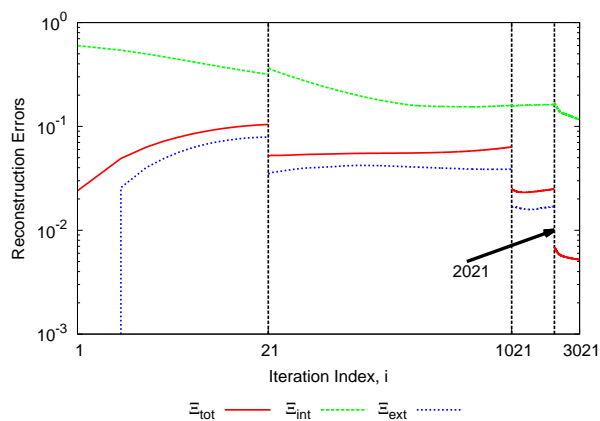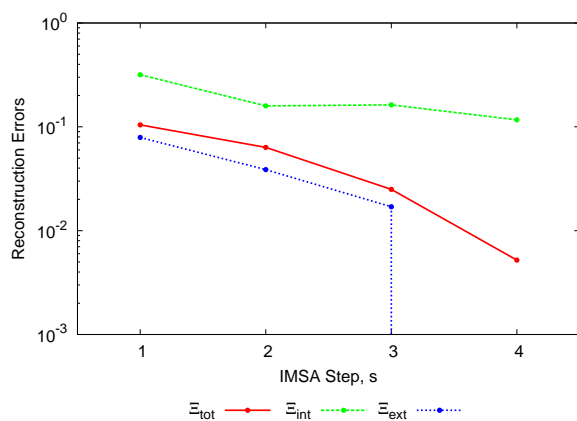
Figure 4.9: *Performance vs. Noise (Square Scatterer - $L = 0.32\,\lambda_b$, ($x_c = -0.16\,\lambda_b$, $y_c = -0.58\,\lambda_b$), $\varepsilon_r = 5.5$, $\sigma = 0.01$ S/m [$\tau = 1.5$], $\varepsilon_{rB} =4.0$, $\sigma_B =0.01$ S/m, $SNR = 10$ dB) - Fitness (a) and reconstruction errors (b) versus outer iterations index, i. (c) Error index values at each focusing step s ($s = 1, ..., S$).*

Finally, it is worth pointing out that the *IMSA-IN* approach requires less *CPU* time than the bare method to reach the convergence solution (Tab. 4.1) since a smaller problem has to be solved at each resolution step.

4.3.3 Effects of the Dielectric Properties of the Target

This Section is aimed at giving some insights on the dependence of the reconstruction accuracy of the proposed approach on the contrast values of the imaged target.
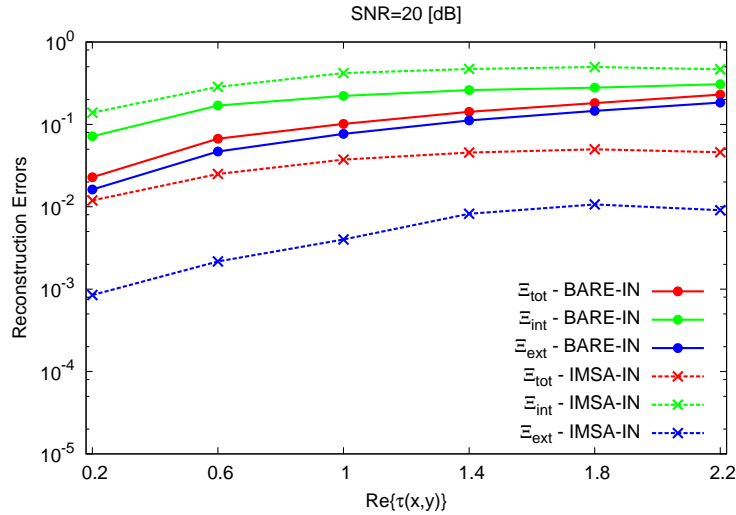
Figure 4.10: *Performance vs. Target Permittivity (Hollow Cylinder -* $L_{ext} = 0.48\,\lambda_b$, $L_{int} = 0.16\,\lambda_b$, $(x_c = 0.08\,\lambda_b$, $y_c = -0.48\,\lambda_b)$, $\sigma = 0.01$ S/m, $\varepsilon_{rB} = 4.0$, $\sigma_B = 0.01$ S/m, $SNR = 20$ dB*) - Reconstruction errors for different values of τ.

A hollow square cylinder has been considered [Fig. 4.11(a)] centered at $(0.08\,\lambda_b, -0.48\,\lambda_b)$ with external side $L_{ext} = 0.48\,\lambda_b$ and internal side $L_{int} = 0.16\,\lambda_b$. The values of the contrast have been changed in the range $\tau \in [0.2,\ 2.2]$. Figure 4.10 gives the inversion results in terms of the total reconstruction error for both the bare and the *IMSA-IN* approaches. It turns out that the two implementations are quite robust against the contrast even though the *IMSA-IN* is able to provide a smaller value of reconstruction error. For illustrative purposes, Figs. 4.11(b) and 4.11(c) show the real part of the contrast function retrieved by the IMSA-IN and the bare approaches when $\tau = 2.2$, while Figs. 4.11(d) and 4.11(e) show the imaginary parts. The plots outline the effectiveness of the multi-resolution approach in both qualitatively and quantitatively imaging the target, while the single-step technique only localizes the target.
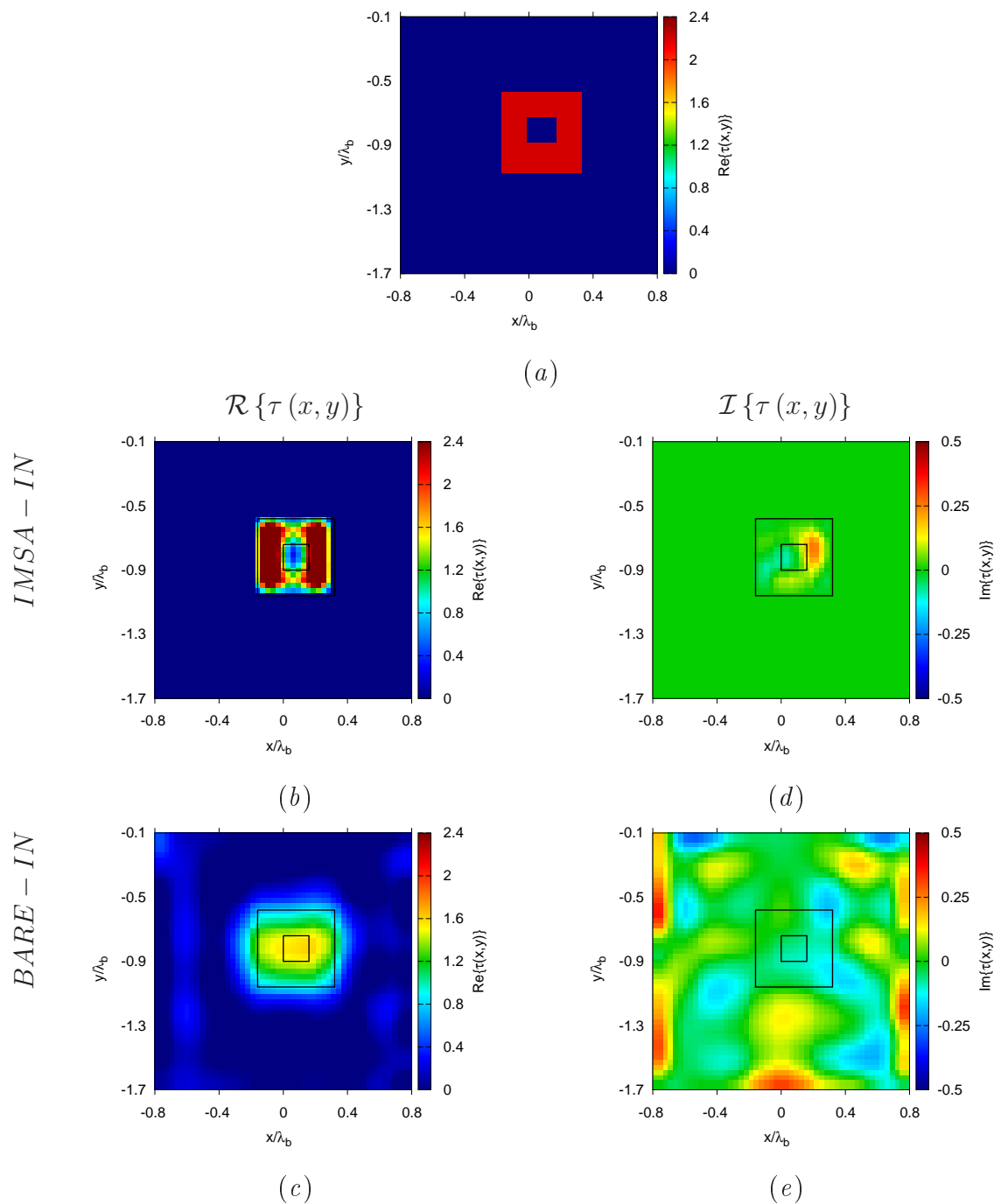
Figure 4.11: *Performance vs. Target Permittivity (Hollow Cylinder -* $L_{ext} = 0.48\,\lambda_b$, $L_{int} = 0.16\,\lambda_b$, ($x_c = 0.08\,\lambda_b$, $y_c = -0.48\,\lambda_b$), $\varepsilon_r = 6.2$, $\sigma = 0.01$ S/m [$\tau = 2.2$], $\varepsilon_{rB} = 4.0$, $\sigma_B = 0.01$ S/m, $SNR = 10$ dB) - Reconstructed distribution of the contrast function. (*a*) Actual configuration and (*b*) real and (*d*) imaginary parts provided by the IMSA-IN strategy and (*c*) real and (*e*) imaginary parts obtained by the BARE-IN.
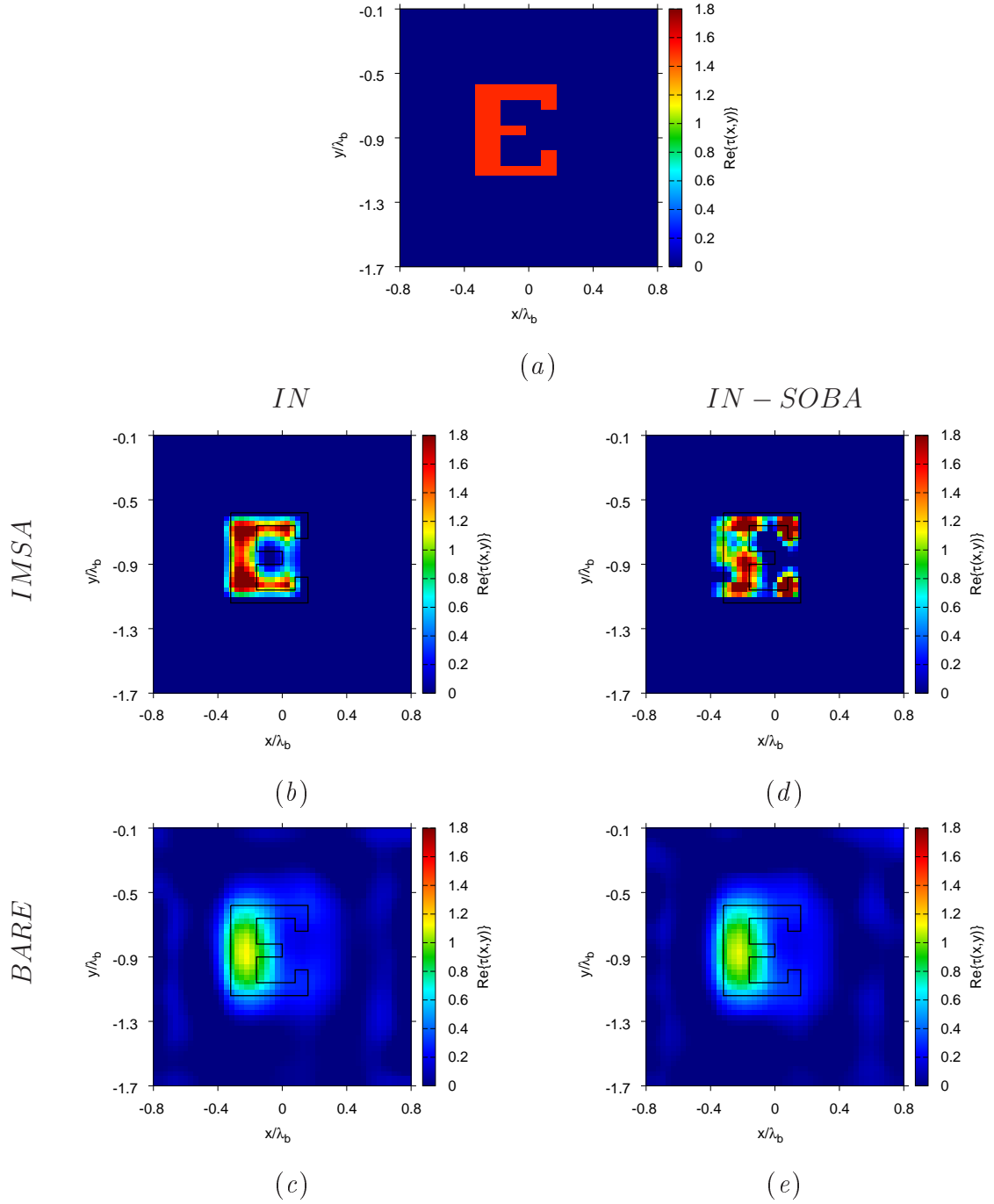
Figure 4.12: *Performance vs. Target Scales* (*E-Shaped Scatterer* - $\varepsilon_r = 5.5$, $\sigma = 0.01$ S/m [$\tau = 1.5$], $\varepsilon_{rB} =$4.0, $\sigma_B =$0.01 S/m, $SNR =$20 dB) - Reconstructed distribution of the contrast function (real part). (*a*) Actual configuration and reconstructions with (*b*)(*d*) *IMSA-IN* and (*c*)(*e*) *IN* under (*b*)(*c*) full-nonlinear and (*d*)(*e*) approximate conditions (*SOBA*).

4.3.4 Reconstruction of Targets with Small Details

The capabilities of the approach in reconstructing target details at dimensions comparable to the inversion grid of the bare technique have been assessed then by considering the object in Fig. 4.12(a). The contrast function retrieved by the *IMSA-IN* algorithm is shown in Fig. 4.12(b) and Fig. 4.13(a) and compared to that from the *IN* method [Fig. 4.12(c) and Fig. 4.13(b)].
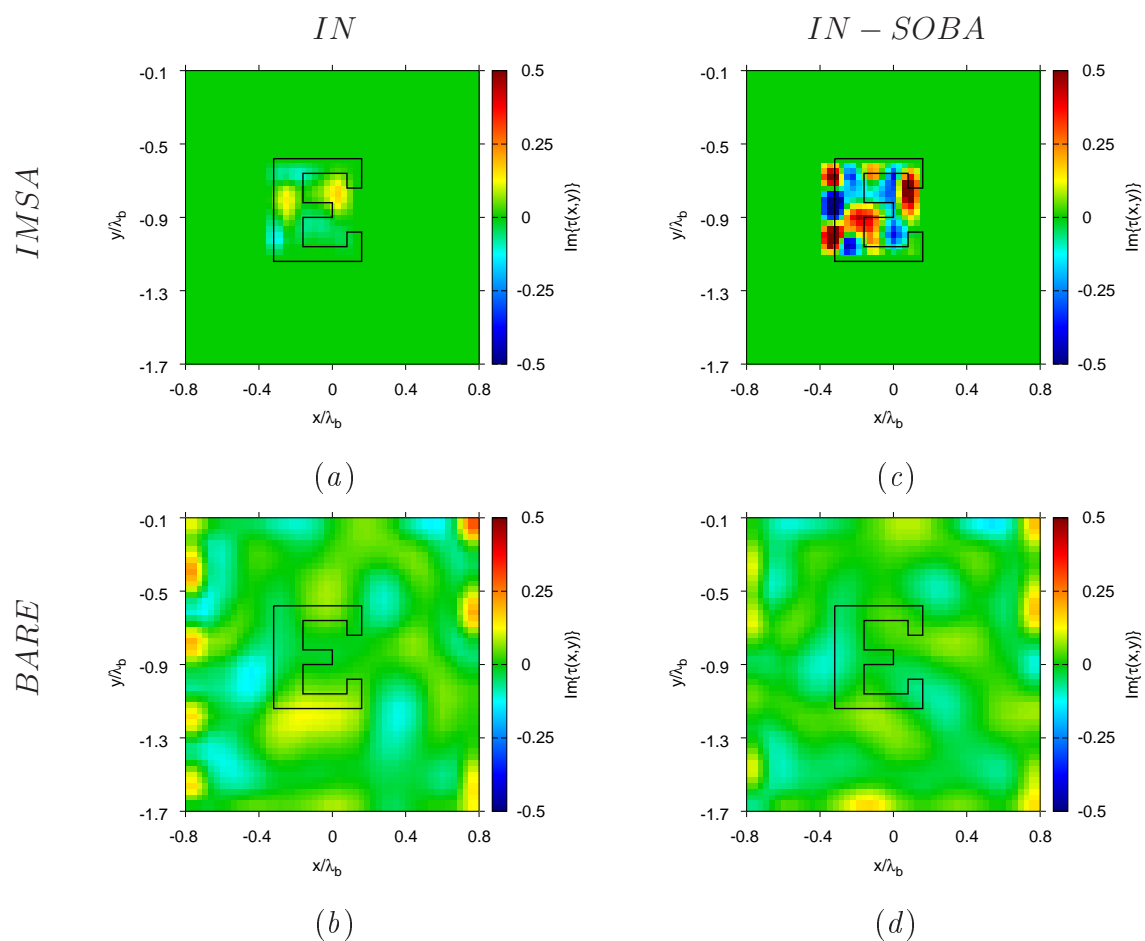
Figure 4.13: *Performance vs. Target Scales (E-Shaped Scatterer -* $\varepsilon_r = 5.5$, $\sigma = 0.01$ S/m [$\tau = 1.5$], $\varepsilon_{rB} = 4.0$, $\sigma_B = 0.01$ S/m, *SNR* =20 dB*) -* Reconstructed distribution of the contrast function (imaginary part) with (a)(c) *IMSA-IN* and (b)(d) *IN* under (a)(b) full-nonlinear and (c)(d) approximate conditions (*SOBA*).

As expected, the multi-scaling strategy provides a quite good reconstruction of the long arms of the E-shaped target because of its intrinsic multi-resolution nature, although the smallest detail in the internal region is not detected probably due to the masking effects of the external region of the scatterer. On the contrary,

the single-step reconstruction significantly gets worse loosing all the object details [Fig. 4.12(c) and Fig. 4.13(b)]. For completeness, the corresponding $SOBA$ implementations are reported in Figs. 4.12(d)-4.12(e) and Figs. 4.13(c)-4.13(d), as well.

4.3.5 Reconstruction of Targets with Higher Conductivity

Finally, the effects of the conductivity of the target have been evaluated. The square object imaged in Sects. 4.3.1 and 4.3.2 has been again considered, but its electric conductivity has been increased to $\sigma = 0.1$ (i.e., $\mathcal{I}\{\tau\} = -5.39$).
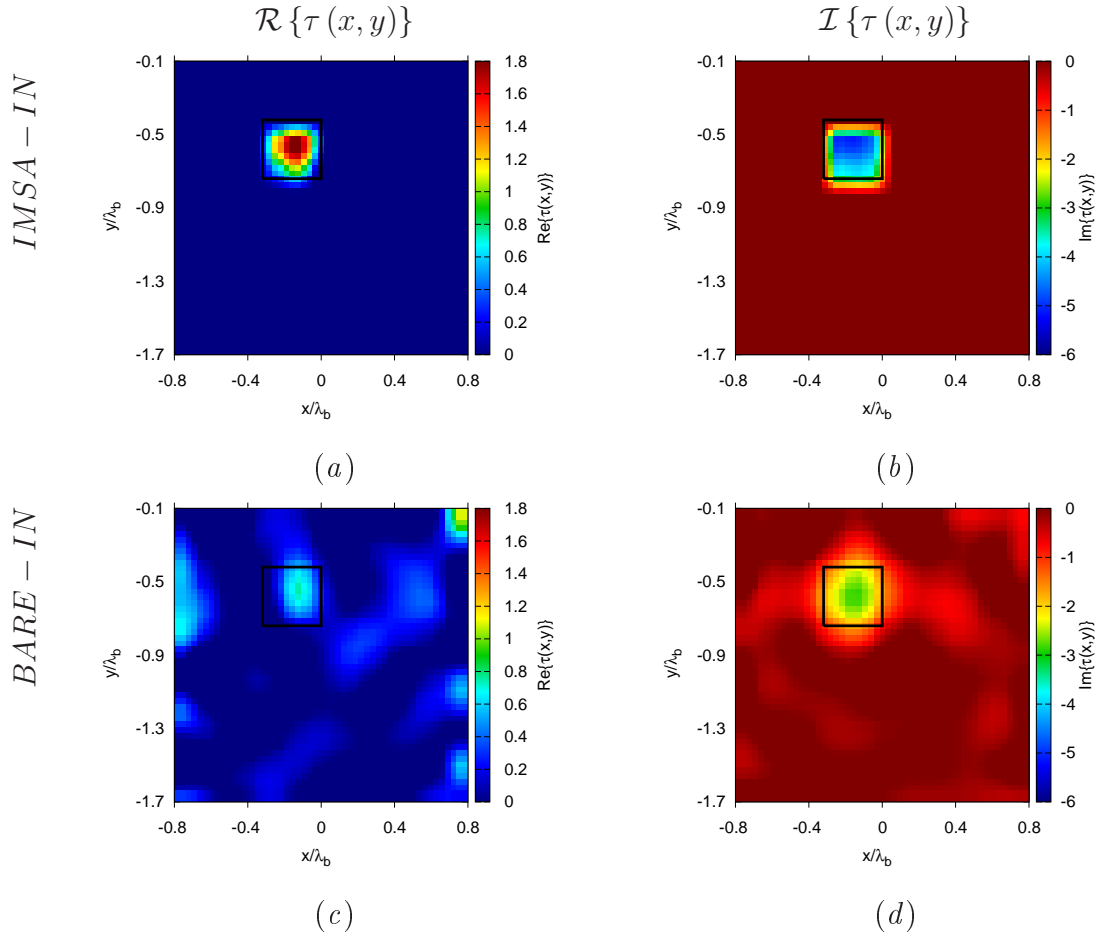
Figure 4.14: *Performance vs. Target Conductivity (Square Scatterer - $L = 0.32\,\lambda_b$, ($x_c = -0.16\,\lambda_b$, $y_c = -0.58\,\lambda_b$), $\varepsilon_r = 5.5$, $\sigma = 0.1$ S/m [$\tau = 1.5 - j5.39$], $\varepsilon_{rB} = 4.0$, $\sigma_B = 0.01$ S/m, $SNR = 10$ dB) - Reconstructed distribution of the contrast function. (a) Real and (b) imaginary parts provided by the IMSA-IN strategy and (c) real and (d) imaginary parts obtained with the bare IN.*

SNR	$\Xi_{tot}\ BARE$	$\Xi_{tot}\ IMSA$
∞ (Noiseless)	3.07×10^{-1}	4.01×10^{-2}
30 [dB]	3.07×10^{-1}	3.98×10^{-2}
20 [dB]	3.14×10^{-1}	1.61×10^{-2}
10 [dB]	3.60×10^{-1}	2.26×10^{-2}
5 [dB]	4.21×10^{-1}	3.97×10^{-2}

Table 4.2: *Performance vs. Target Conductivity (Square Scatterer - $L = 0.32\,\lambda_b$, ($x_c = -0.16\,\lambda_b$, $y_c = -0.58\,\lambda_b$), $\varepsilon_r = 5.5$, $\sigma = 0.1$ S/m [$\tau = 1.5 - j5.39$], $\varepsilon_{rB} = 4.0$, $\sigma_B = 0.01$ S/m) - Reconstruction errors for the bare IN and the IMSA-IN (at step $s = S = 4$) approaches.*

The reconstruction errors for different values of the signal-to-noise ratio are reported in Tab. 4.2 to assess in this case, too, the *IMSA-IN* strategy improvements over to the bare method. This is also visually confirmed by the representative distributions of the contrast function shown in Fig. 4.14, which refer to the case $SNR = 10$ dB. Indeed, both real and imaginary parts of the contrast function are successfully retrieved by the *IMSA-IN* strategy [Figs. 4.14(a)-4.14(b)] being closer to the actual ones. The same accuracy is not achieved by the bare implementation [Figs. 4.14(c)-4.14(d)].

4.4 Discussions

In this chapter, a microwave imaging technique for the reconstruction of shallow buried objects has been presented. The proposed approach extends the strategy presented in Chapter 3 by employing the full non-linear formulation of the scattering problem. In this way, the method is potentially able to deal with strong scatterers, too. The reconstruction performances have been evaluated by means of several numerical simulations. It has been found that the proposed approach provides quite good reconstructions of the considered targets showing a good robustness to the noise, as well. Moreover, the results from the multi-focusing strategy turned out to be better both in terms of reconstruction errors and computational resources than the standard bare inexact-Newton algorithm when applied to the same scattering configurations. Future works will be devoted to an experimental validation of the proposed inversion algorithm.

Chapter 5

GPR Prospecting through an Inverse Scattering Frequency-Hopping Multi-Focusing Approach

In this chapter, an innovative information-acquisition approach to 2D Ground-Penetrating Radar (GPR) prospecting is presented. A microwave inverse-scattering nested approach combining a frequency-hopping (FH) procedure and a multi-focusing (MF) technique is proposed. On the one hand, the FH scheme effectively handles multi-frequency GPR data, while mitigating the non-linearity issues. On the other, MF techniques have proved to be effective tools for reducing the occurrence of multi-local-minima affecting GPR investigations then allowing the use of a local search technique based on the Conjugate Gradient (CG) method to iteratively solve the inverse problem at hand. Selected results are reported and analyzed to give some insights to the interested readers on the advantages and the limitations of such an approach when handling synthetically-generated and experimental GPR data, as well.

5.1 Introduction and Rationale

In the last decades, ground penetrating radars (*GPR*s) have been widely used in subsurface non-destructive testing (*NDT*) problems [1][13][77][78] arising in archaeology, geology, demining, pavement survey, tunnel detection, and police investigation [59][79]-[83]. Such a popularity mainly derives from the superior performance in terms of resolution, depth of investigation, speed, and costs compared to other *NDT* technologies [59][79][80][83]. Unfortunately, retrieving the dielectric properties of buried object from *GPR* data, usually collected in the time domain, is a very challenging task because of the theoretical properties of the associated inverse problems (i.e., ill posedness and non-linearity [84][85]) as well as the dimensionality of the problem at hand [86]. To face such challenges, several *GPR* prospecting algorithms have been proposed in the state-of-the-art literature. Approximate formulations of the complete non-linear problem have been often taken into account [84][86]-[88]. More specifically, weak scatterers have been successfully retrieved through Born [84][86][88][89] or distorted-Born *GPR* approximations [87] by solving the arising linear problem with truncated singular value decomposition (*TSVD*) algorithms [84][86]-[88]. Nevertheless, the derivation of *GPR* prospecting techniques able to faithfully handle strong and/or extended scatterers and deal with related multi-minima issues is still an open challenge [83]. Indeed, even though global search strategies based on Evolutionary Algorithms (*EA*s) could, in principle, successfully address nonlinear problems [34][41], their "bare" use is generally prevented in subsurface imaging because of the size of the domains under investigations and the arising convergence and computational loads.

On the other hand, the generalization of multi-focusing (*MF*) inversion techniques borrowed from "free-space" imaging [54][72][75] is a potentially appealing approach to be adopted since *GPR* time-domain signals are intrinsically multi-frequency data. Historically, *MF* iterative strategies have been specifically introduced to mitigate local minima problems in inverse scattering [51][54][72]. By keeping at each *MF* iteration the number of unknowns as close as possible to the available data information [90], the original complex imaging problem is recast to a sequence of simpler data-mismatching cost function minimizations where the occurrence of local minima is strongly reduced [54][72]. This latter enables as an interesting by-product the possibility to use local optimization strategies that allow a significant computational saving with respect to *EA*s [34][41].

This chapter is then aimed at introducing a robust and efficient complement to existing *GPR* prospecting strategies based on the multi-minima mitigation capabilities of *MF* procedures. Towards this end, subsurface imaging from time-domain *GPR* data is firstly recast to a multi-frequency inversion then a frequency-hopping (*FH*) [91]-[93] iterative scheme is adopted. Since each *GPR* frequency data is associated to a different level of spatial resolution [92], the *FH* approach is suitably integrated in a hierarchical multi-resolution scheme that ex-

ploits a Conjugate Gradient (*CG*) [30][94] local strategy as optimization solver.
The outline of the chapter is as follows. After the formulation of the *GPR*
prospecting problem (Sect. 5.2), the proposed *FHMF-CG* method is introduced
and discussed (Sect. 5.3). It is then assessed against synthetic data generated
through *GprMax* software [95] and comparisons with state-of-the-art techniques
[87][96] are also discussed, while experimental validations [97] follow (Sect. 5.4).
Eventually, some conclusions are reported (Sect. 5.5).

5.2   *GPR* Prospecting - Inverse Scattering Formulation

Let us consider the *GPR* transverse-magnetic problem sketched in Fig. 5.1(*a*)
where two homogeneous, isotropic, and non-magnetic half-spaces are separated
by an interface at $y = 0$. The lower half space of *background* relative permittivity
ε_{rB} and *background* conductivity σ_B, contains a set of scatterers located within
the investigation domain D_{inv} [Fig. 5.1(*a*)] and described by discontinuous (wrt
the background) profiles of permittivity $\varepsilon_r(\mathbf{r})$ and conductivity $\sigma(\mathbf{r})$. The free-
space (ε_0 and $\sigma_0 = 0$) upper half space comprises a set of V z-directed ideal
line sources located at $\mathbf{r}_v = (x_v, y_v > 0)$, $v = 1, .., V$ and excited with the time-
domain current $\chi(t)$ [Fig. 5.1(*b*)] to generate in free space the *radiated* field
[98][99]

$$w_v(\mathbf{r}, t)\widehat{\mathbf{z}} = \left[\frac{1}{2\pi|\mathbf{r} - \mathbf{r}_v|c_0}\delta\left(t - \frac{|\mathbf{r} - \mathbf{r}_v|}{c_0}\right) * h(\mathbf{r} - \mathbf{r}_v, t) * \frac{\partial\chi(t)}{\partial t}\right]\widehat{\mathbf{z}} \quad (5.1)$$

where t stands for the time variable, $*$ is the convolution operator, c_0 is the free-
space speed of light, $\delta(\cdot)$ the Dirac's delta, and $h(\mathbf{r}, t)$ is the transient response
of the antenna source located in $\mathbf{r}$ [99].
From the interactions between the V line sources and the lower half space (i.e.,
the background and the scatterers) the signal (i.e., the *GPR* radargram) collected
by the M ideal probes located in the upper half-space at $\mathbf{r}_m = (x_m, y_m > 0)$,
$m = 1, ..., M$, [Fig. 5.1(*d*)] is given by

$$\widetilde{u}_v(\mathbf{r}_m, t) = u_v(\mathbf{r}_m, t) + q_v(\mathbf{r}_m, t) = e_v(\mathbf{r}_m, t) + s_v(\mathbf{r}_m, t) + q_v(\mathbf{r}_m, t)$$
$$m = 1, ..., M; \ v = 1, ..., V \quad (5.2)$$

where s_v is the *scattered* electric field, q_v is a zero-mean additive Gaussian noise
term modelling the measurement/environment noise, and e_v is the *incident* (i.e.,
the electromagnetic field of the same scenario but without the scatterers) electric
field.

Figure 5.1: *Problem definition* - Geometry of the problem (a), plot of the excitation signal in (b) time domain (i.e., $\chi(t)$) and (c) frequency domain (i.e., $X(f)$), and of a typical *GPR* trace $\widetilde{u}_v(\mathbf{r}_m, t)$ (d) and associated scattered field $\widetilde{s}_v(\mathbf{r}_m, t)$ (e).

In order to retrieve the scatterers profile starting from the *GPR* radargrams,
the *scattered* field data [88] $[\widetilde{s}_v(\mathbf{r}_m,t) \triangleq \widetilde{u}_v(\mathbf{r}_m,t) - e_v(\mathbf{r}_m,t)$ - Fig. 5.1$(e)]$ are
firstly determined by temporal muting the first part of the *GPR* trace $\widetilde{u}_v(\mathbf{r}_m,t)$,
$m = 1,...,M$, $v = 1,...,V$, that accounts for the direct coupling between the
transmitting source antenna and the air-soil interface [Fig. 5.1(d)]

$$\widetilde{s}_v(\mathbf{r}_m,t) = \Gamma[\widetilde{u}_v(\mathbf{r}_m,t)] \quad v = 1,...,V, \tag{5.3}$$

$\Gamma[\cdot]$ being the gating operator [Fig. 5.1(e)]. Indeed, such a pre-processing pro-
cedure is equivalent, for the half-space scenario at hand, to the subtraction of
the *incident* (or unperturbed) field, e_v, from the *total* field, $\widetilde{u}_v$, which is a cus-
tomary operation in microwave inverse scattering experiments under controlled
conditions.
Afterwards, the Fourier transform of the time scattered data is computed in K
frequency samples

$$\widetilde{S}_v^{(k)}(\mathbf{r}_m) \triangleq \int_{-\infty}^{\infty} \widetilde{s}_v(\mathbf{r}_m,t) \exp\left(j2\pi f^{(k)}t\right) dt$$
$$m = 1,...,M; \ v = 1,...,V; \ k = 1,...,K \tag{5.4}$$

to avoid both 'insufficiency' and redundancy in the data as well as reducing the
computational costs and the measurement burden, thus making it possible to
investigate wider domains D_{inv}. In (5.4), $f^{(k)} \in [f_{\min}, f_{\max}]$ is the k-th sam-
pling frequency, $[f_{\min}, f_{\max}]$ being the 3dB bandwidth of the spectrum of the
illuminating pulse $X(f) = \int_{-\infty}^{\infty} \chi(t) \exp(j2\pi ft) dt$ [Fig. 5.1(c)] [88].
In frequency-domain framework, the original retrieval problem becomes then that
of retrieving, in the investigation domain D_{inv}, the object function [84][?]

$$\tau^{(k)}(\mathbf{r}) \triangleq \frac{(\varepsilon_r(\mathbf{r}) - \varepsilon_{rB}) - j\frac{\sigma(\mathbf{r})-\sigma_B}{2\pi f^{(k)}\varepsilon_0}}{\varepsilon_0}, \ k = 1,...,K \tag{5.5}$$

and the *total* field

$$U_v^{(k)}(\mathbf{r}) \triangleq \int_{-\infty}^{\infty} u_v(\mathbf{r},t) \exp\left(j2\pi f^{(k)}t\right) dt \quad v = 1,...,V; \ k = 1,...,K \tag{5.6}$$

starting from the *scattered*, $\widetilde{S}_v^{(k)}(\mathbf{r}_m)$, $m = 1,...,M$, $v = 1,...,V$, $k = 1,...,K$, and
the *radiated*, $E_v^{(k)}(\mathbf{r}) \triangleq \int_{-\infty}^{\infty} e_v(\mathbf{r}_m,t) \exp\left(j2\pi f^{(k)}t\right) dt$, $v = 1,...,V$, $k = 1,...,K$,
field frequency samples. Mathematically, such a problem can be recast to the
minimization of the data-mismatch cost function [84]

$$\Phi^{(k)} = \frac{\sum_{v=1}^{V}\sum_{m=1}^{M}\left|S_v^{(k)}(\mathbf{r}_m)-\widehat{S}_v^{(k)}(\mathbf{r}_m)\right|^2}{\sum_{v=1}^{V}\sum_{m=1}^{M}\left|\widetilde{S}_v^{(k)}(\mathbf{r}_m)\right|^2} + \frac{\sum_{v=1}^{V}\int_{D_{inv}}\left|E_v^{(k)}(\mathbf{r})-\widehat{E}_v^{(k)}(\mathbf{r})\right|^2 d\mathbf{r}}{\sum_{v=1}^{V}\int_{D_{inv}}\left|E_v^{(k)}(\mathbf{r})\right|^2 d\mathbf{r}}$$
$$k = 1,..,K \tag{5.7}$$

where $\widehat{S}_v^{(k)}(\mathbf{r})$ and $\widehat{E}_v^{(k)}(\mathbf{r})$ stand for the *retrieved* versions of $S_v^{(k)}(\mathbf{r})$ and $E_v^{(k)}(\mathbf{r})$,
respectively, and they are related to the estimated quantities $\widehat{\tau}^{(k)}(\mathbf{r})$ and $\widehat{U}_v^{(k)}(\mathbf{r})$

through the *data* [84]

$$\widehat{S}_v^{(k)}\left(\mathbf{r}_m\right) = k_B^2 \int_{D_{inv}} \mathcal{G}_{ext}^{(k)}\left(\mathbf{r}_m, \mathbf{r}'\right) \widehat{U}_v^{(k)}\left(\mathbf{r}'\right) \widehat{\tau}^{(k)}\left(\mathbf{r}'\right) d\mathbf{r}'$$
$$m = 1, .., M, \; k = 1, ..., K, \; v = 1, ..., V \tag{5.8}$$

and the *state* equations [84]

$$\widehat{E}_v^{(k)}\left(\mathbf{r}\right) = \widehat{U}_v^{(k)}\left(\mathbf{r}\right) - k_B^2 \int_{D_{inv}} \mathcal{G}_{int}^{(k)}\left(\mathbf{r}, \mathbf{r}'\right) \widehat{U}_v^{(k)}\left(\mathbf{r}'\right) \widehat{\tau}^{(k)}\left(\mathbf{r}'\right) d\mathbf{r}'$$
$$\mathbf{r} \in D_{inv}, \; k = 1, ..., K, \; v = 1, ..., V \tag{5.9}$$

$\mathcal{G}_{int}^{(k)}\left(\mathbf{r}, \mathbf{r}'\right)$ and $\mathcal{G}_{ext}^{(k)}\left(\mathbf{r}, \mathbf{r}'\right)$ being the 2D internal and external *half-space* Green's functions for the k-th frequency [84], respectively.
The problem of interest can be now summarized/stated as follows

> ***GPR* Inverse Scattering Prospecting Problem** - Given $E_v^{(k)}\left(\mathbf{r}\right)$ and $\widetilde{S}_v^{(k)}\left(\mathbf{r}_m\right)$, $m = 1, ..., M$, $v = 1, ..., V$, $k = 1, ..., K$, find $\widehat{\tau}^{(k)}\left(\mathbf{r}\right)$ and $\widehat{U}_v^{(k)}\left(\mathbf{r}\right)$, $v = 1, ..., V$, $k = 1, ..., K$, within D_{inv} such that (5.7) is minimized.

5.3 *FHMF-CG* Inversion Procedure

The proposed solution procedure is a nested iterative algorithm composed by an external loop ($k = 1, ..., K$) implementing the *FH* strategy, while the internal loop ($s = 1, ..., S$) performs the *MF* (Fig. 5.2).
The external *FH* scheme is essentially an information acquisition process consisting of K successive solutions of (5.7), each cycle being related to the k-th frequency. Although the contrast is a dispersive quantity whether lossy materials are at hand[1] (5.5), the reconstruction yielded at the $(k-1)$-th step can be exploited to provide a profitable initialization for the successive k-th one [91][92][93] (e.g., the scatterer support generally does not change):

$$\begin{cases} \left.\widehat{\tau}^{(k)}\left(\mathbf{r}\right)\right|^{guess} = 0 & k = 1 \\ \left.\widehat{\tau}^{(k)}\left(\mathbf{r}\right)\right|^{guess} = \Re\left\{\widehat{\tau}^{(k-1)}\left(\mathbf{r}\right)\right\} + j\Im\left\{\widehat{\tau}^{(k-1)}\left(\mathbf{r}\right)\right\}\frac{f^{(k-1)}}{f^{(k)}} & k = 2, ..., K. \end{cases} \tag{5.10}$$

In (5.10) the contrast function retrieved at the $(k-1)$-th step is rescaled to the k-th frequency by multiplying its imaginary part by the ratio $f^{(k-1)}/f^{(k)}$. Moreover, the guess *total* field distribution at the k-th external iteration is computed, unlike state-of-the-art *FH* methods [91], as follows

$$\begin{cases} \left.\widehat{U}_v^{(k)}\left(\mathbf{r}\right)\right|^{guess} = E_v^{(k)}\left(\mathbf{r}\right) & k = 1 \\ \left.\widehat{U}_v^{(k)}\left(\mathbf{r}\right)\right|^{guess} = \Psi\left[E_v^{(k)}\left(\mathbf{r}\right), \left.\widehat{\tau}^{(k)}\left(\mathbf{r}\right)\right|^{guess}\right] & k = 2, ..., K \end{cases} \tag{5.11}$$

---

[1] Lossy scenarios are common in *GPR* applications because of the conductive nature of the materials and the soils at hand [79][80][81][82][83].

where $\Psi[\cdot]$ stands for the 2D direct solver operator numerically computed by means of the Method of Moments (*MoM*)[91].
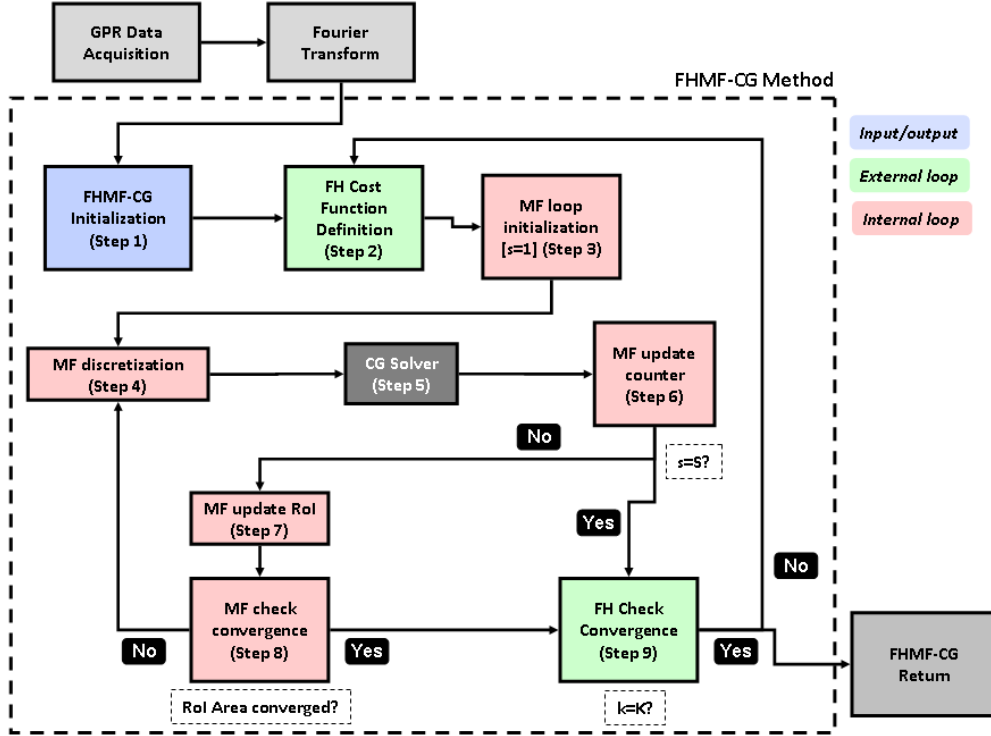
Figure 5.2: FHMF-CG *Inversion Procedure* - Flowchart of the *GPR* prospecting method.

The internal *MF* loop (Fig. 5.2), carried out at each k-th frequency step, is aimed at solving the k-th monochromatic *GPR* problem by numerically minimizing the cost function $\Phi^{(k)}$ (5.7) in S zooming steps starting from the initial ($s = 1$) distributions of the unknowns (5.10)(5.11). Towards this end, the problem unknowns, $\tau^{(k)}(\mathbf{r})$ and $U_v^{(k)}(\mathbf{r})$ in (5.8) and (5.9), are discretized at each s-th step according to a multi-focusing scheme that automatically enhances the spatial resolution in correspondence with the *Regions of Interest* (*RoI*s) of D_{inv} [54][72] where the scatterers have been detected. More in detail, the s-th *RoI* Ω_s ($\Omega_1 = D_{inv}$) is partitioned into N square subdomains centered at $\mathbf{r}_n|_s$ ($\mathbf{r}_n|_s \in \Omega_s$, $n = 1, ..., N$), N being the number of degrees of freedom (*DoF*s) of the scattered field $S_v^{(k)}$ [57], to yield

$$\widehat{U}_v^{(k)}(\mathbf{r})\Big|_s = \sum_{n=1}^{N} \widehat{U}_{v,n}^{(k)}\Big|_s \psi_n^{(k)}(\mathbf{r}')\Big|_s \qquad (5.12)$$

and

$$\left.\widehat{\tau}^{(k)}\left(\mathbf{r}\right)\right|_s = \sum_{n=1}^{N} \left.\widehat{\tau}_n^{(k)}\right|_s \left.\psi_n^{(k)}\left(\mathbf{r}\right)\right|_s \tag{5.13}$$

where $\left.\psi_n^{(k)}\left(\mathbf{r}\right)\right|_s$ is the n-th rectangular pulse basis function at the s-th *MF* step of the k-th frequency, while $\left.\widehat{U}_{v,n}^{(k)}\right|_s$ and $\left.\widehat{\tau}_n^{(k)}\right|_s$ are the corresponding field and contrast unknown coefficients, respectively. By substituting (5.12) and (5.13) in (5.8) and (5.9), the following discretized form of the *data*

$$\widehat{S}_v^{(k)}\left(\mathbf{r}_m\right) = \sum_{n=1}^{N} \left.\widehat{U}_{v,n}^{(k)}\right|_s \left.\widehat{\tau}_n^{(k)}\right|_s \int_{D_{inv}} \mathcal{G}_{ext}^{(k)}\left(\mathbf{r}_m,\mathbf{r}'\right) \left.\psi_n^{(k)}\left(\mathbf{r}'\right)\right|_s d\mathbf{r}'$$
$$m = 1,..,M,\ k = 1,...,K,\ v = 1,...,V \tag{5.14}$$

and the *state* equations

$$\widehat{E}_v^{(k)}\left(\left.\mathbf{r}_n\right|_s\right) = \left.\widehat{U}_{v,n}^{(k)}\right|_s - \sum_{n=1}^{N} \left.\widehat{U}_{v,n}^{(k)}\right|_s \left.\widehat{\tau}_n^{(k)}\right|_s \int_{D_{inv}} \mathcal{G}_{int}^{(k)}\left(\left.\mathbf{r}_n\right|_s,\mathbf{r}'\right) \left.\psi_n^{(k)}\left(\mathbf{r}'\right)\right|_s d\mathbf{r}'$$
$$\mathbf{r} \in D_{inv},\ k = 1,...,K,\ v = 1,...,V \tag{5.15}$$

are obtained to deduce the discretized version of (5.7), $\left.\Phi^{(k)}\right|_s$, to be minimized with a numerically efficient local search algorithm. Owing to the suitable choice of the ratio between measurement data and unknowns according to the *DoF* criterion [57] and the (consequent) reduced occurrence of local minima [90], a *CG*-based deterministic optimization strategy [30][94] is here adopted. Starting from (5.10) and (5.11), such a minimization technique is defined through by the following update equations [30][94]

$$\begin{cases} \left.\widehat{\mathbf{U}}_v^{(k)}\right|_s^{i+1} = \left.\widehat{\mathbf{U}}_v^{(k)}\right|_s^i + \left.\alpha_v^{(k)}\right|_s^i \left.\mathbf{a}_v^{(k)}\right|_s^i \\ \left.\widehat{\boldsymbol{\tau}}_v^{(k)}\right|_s^{i+1} = \left.\widehat{\boldsymbol{\tau}}_v^{(k)}\right|_s^i + \left.\beta_v^{(k)}\right|_s^i \left.\mathbf{b}_v^{(k)}\right|_s^i \end{cases} \tag{5.16}$$

where $i = 1,...,I$ is the minimization iteration index,

$$\left.\widehat{\mathbf{U}}_v^{(k)}\right|_s^i \triangleq \left\{ \left.\widehat{U}_{v,n}^{(k)}\right|_s^i,\ n = 1,...,N \right\} \tag{5.17}$$

and

$$\left.\widehat{\boldsymbol{\tau}}_v^{(k)}\right|_s^i \triangleq \left\{ \left.\widehat{\tau}_n^{(k)}\right|_s^i,\ n = 1,...,N \right\} \tag{5.18}$$

are the unknown total field and contrast vectors, respectively, $\left.\mathbf{a}_v^{(k)}\right|_s^i$ and $\left.\mathbf{b}_v^{(k)}\right|_s^i$ are the corresponding search directions proportional to the gradient of $\left.\Phi^{(k)}\right|_s$ [30][94]), while $\left.\alpha_v^{(k)}\right|_s^i$ and $\left.\beta_v^{(k)}\right|_s^i$ are the associated step lengths.

Once $i = I$ or the cost function stagnation arises[54]), the minimization loop (5.16) is stopped and a new internal *MF* step is performed ($s \leftarrow s + 1$) to update the localization and the size of Ω_s through *filtering* and *clustering* [54].

Successively, the spatial resolution is enhanced within the detected *RoI* by updating $\mathbf{r}_n|_s$ ($s = 2, ..., S$, $\mathbf{r}_n|_s \in \Omega_s$, $n = 1, ..., N$), and the *CG*-based process is carried out again and again until the *MF* process terminates (i.e., $s = S$ or the extension of the *RoI* does not change significantly) [54]. Successively, the estimated coefficients vectors, $\left.\widehat{\boldsymbol{\tau}}_v^{(k)}\right|_S^I$ and $\left.\widehat{\mathbf{U}}_v^{(k)}\right|_S^I$, are substituted in (5.12) and (5.13) and then passed to the successive *FH* step according to (5.10) and (5.11). The whole *FHMF-CG* procedure iterates until the local minimization of the last multi-focusing iteration ($s = S$) of the highest frequency ($k = K$) is completed ($i = I$).

In short, the proposed *GPR* prospecting inverse scattering method can be summarized as follows (Fig. 5.2):

1. **Initialization**. Determine $E_v^{(k)}(\mathbf{r})$ and $\widetilde{S}_v^{(k)}(\mathbf{r}_m)$, $m = 1, ..., M$, $v = 1, ..., V$, $k = 1, ..., K$ from *GPR* radargrams, $\widetilde{u}_v(\mathbf{r}_m, t)$, $m = 1, ..., M$, $v = 1, ..., V$ (see Sect. 5.2). Set $k = 1$;

2. ***FH* Loop**. Define $\Phi^{(k)}$ (5.7) and initialize the unknowns by setting (5.10) and (5.11);

3. ***MF* Loop**. Set $s = 1$, $\Omega_s = D_{inv}$. Compute N according to the *DoF* criterion [57];

4. ***MF* Loop**. Discretize the s-th *RoI* by computing the cell centers, $\mathbf{r}_n|_s \in \Omega_s$, $n = 1, ..., N$. Deduce the *MF* cost function by substituting (5.14) and (5.15) in (5.7);

5. **Deterministic Minimization**. Update $\left.\widehat{\mathbf{U}}_v^{(k)}\right|_s^I$ and $\left.\widehat{\boldsymbol{\tau}}_v^{(k)}\right|_s^I$, $v = 1, ..., V$, according to (5.16) until convergence ($i = I$);

6. ***MF* Loop**. If $s = S$ then return $\left.\widehat{\mathbf{U}}_v^{(k)}\right|_S^I$ and $\left.\widehat{\boldsymbol{\tau}}_v^{(k)}\right|_S^I$ and goto *Step 9*, else goto *Step 7*;

7. ***MF* Loop**. Set $s \leftarrow s + 1$ and update Ω_s with "filtering" and "clustering" procedures [54];

8. ***MF* Loop**. If $\frac{|area\{\Omega_s\} - area\{\Omega_{s-1}\}|}{|area\{\Omega_s\}|} \leq \gamma$ then return $\left.\widehat{\mathbf{U}}_v^{(k)}\right|_s^I$ and $\left.\widehat{\boldsymbol{\tau}}_v^{(k)}\right|_s^I$ and goto *Step 9*, else goto *Step 4*;

9. ***FH* Loop**. If $k = K$ then substitute the final coefficients $\left.\widehat{U}_{v,n}^{(k)}\right|_S = \left.\widehat{U}_{v,n}^{(k)}\right|_S^I$, $n = 1, ..., N$, $v = 1, ..., V$, and $\left.\widehat{\tau}_v^{(k)}\right|_S = \left.\widehat{\tau}_v^{(k)}\right|_S^I$, $v = 1, ..., V$, in (5.12) and (5.13) to determine $\widehat{\tau}^{(k)}(\mathbf{r}) = \left.\widehat{\tau}^{(k)}(\mathbf{r})\right|_S$ and $\widehat{U}_v^{(k)}(\mathbf{r}) = \left.\widehat{U}_v^{(k)}(\mathbf{r})\right|_S$, $k = 1, ..., K$. Otherwise, set $k \leftarrow k + 1$ and goto *Step 2*.

It is worth observing that the *FHMF-CG* approach turns out very flexible since each procedural block (i.e., *FH* scheme, *MF* technique, minimizer) can be easily modified, updated, or substituted without altering the other ones. Analogously, the cost function (5.7) can be easily adapted to take into account additional regularization terms (e.g., multiplicative [101] or sparseness terms [?][23]). However, these investigations are beyond the scope of the current research work and they will be properly addressed in future investigations.

5.4 Numerical and Experimental Validation

5.4.1 Rationale and Figures of Merit

In this section, a set of illustrative experiments is presented to assess the features and the potentialities of the proposed *FHMF-CG* inversion procedure in terms of accuracy, numerical efficiency, and robustness both considering synthetic (Sect. 5.4.2) and measured data (Sect. 5.4.3). Towards this end, the application of the proposed *MF* scheme has been carried out by preprocessing the *GPR* time-domain signals[2] [Fig. 5.1(b)] through a discrete Fourier transform (Fig. 5.2), and then extracting the data sets at K equispaced frequencies within the 3dB bandwidth of the illuminating pulse [Fig. 5.1(c)]. As regards the numerical examples, time-domain synthetic data generated by means of *GprMax* software [95] have been corrupted by zero-mean additive Gaussian noise, and the signal-to-noise ratio (SNR) has been referred to the total field as [102]

$$SNR \triangleq \frac{\sum_{v=1}^{V} \sum_{m=1}^{M} \sum_{k=1}^{K} \left| T_v^{(k)}\left(\mathbf{r}_m\right) \right|^2}{\sum_{v=1}^{V} \sum_{m=1}^{M} \sum_{k=1}^{K} \left| N_v^{(k)}\left(\mathbf{r}_m\right) \right|^2}. \tag{5.19}$$

To assess the quality and efficiency of the method, beyond the visual representation of the retrieved contrast profiles, the integral error figures [54]

$$\Xi_{reg}^{(k)} = \frac{1}{N_{reg}} \sum_{n=1}^{N_{reg}} \frac{\left| \hat{\tau}^{(k)}\left(\mathbf{r}_n\right) - \tau^{(k)}\left(\mathbf{r}_n\right) \right|}{\left| \tau^{(k)}\left(\mathbf{r}_n\right) + 1 \right|} \tag{5.20}$$

[where *reg* indicates if the error computation covers the overall investigation domain ($reg \Rightarrow tot$), the actual scatterer support ($reg \Rightarrow int$) or the background region ($reg \Rightarrow ext$)] have been reported, along with the inversion time Δt. Furthermore, the control parameters of the *MF* and *CG* procedures have been selected according to the guidelines in [30][54][72].

---

[2]It is worth remarking that *GPR* time-domain data, usually available in *radargrams*, have been considered in both synthetic and experimental examples.

5.4.2   Numerical Validation

5.4.2.1   Performance Assessment

The first set of examples is devoted to assess the performance of the proposed *FHMF-CG* method when processing synthetic data. The benchmark 2D *GPR* scenario consists of a square investigation domain of side 0.8 m centered at $(0.00, -0.4)$ m which is illuminated by $V = 20$ sources radiating a time-domain Gaussian monocycle pulse [Fig. 5.1(b)] with spectrum centered at 300 MHz and 3 dB bandwidth covering the [200.0, 600.0] MHz range [Fig. 5.1(c)]. The sources are equally spaced on a 1 m line which is located at $y = 0.1$ m above the soil [Fig. 5.1(a)], which is characterized by $\varepsilon_{rB} = 4.0$, $\sigma_B = 10^{-3}$ S/m. A set of $M = 19$ probes [co-located with the sources[3] - Fig. 5.1(a)] collect the total field, and the Fourier transform is carried out assuming $K = 5$ frequencies.

In order to illustrate the *FHMF-CG* procedure (Sect. 5.3) on a step-by-step basis, a "hollow square" profile (internal side 0.08 m, external side 0.24 m) centered at $(0.12, -0.36)$ m and characterized by $\tau = 1.0$ [Fig. 5.3(a)] has been imaged in noiseless conditions (Fig. 5.3). The reconstructions obtained at the $k = 1$ *FH* iteration (corresponding to the lowest frequency, $f_k = 200$ MHz - Fig. 5.3) show that the multi-focusing procedure starts from the rough $s = 1$ reconstruction [Fig. 5.3(b)], and then progressively zooms on the scatterer support [$s = 2$, Fig. 5.3(c); $s = 3$, Fig. 5.3(d)] until the convergence of the *MF* loop is reached [i.e., $s = S = 4$, Fig. 5.3(e)]. Afterwards, the *FH* loop iterates on the subsequent frequency ($k = 2$, $f_k = 300$ MHz), performing the same iterative process [but exploiting the gathered information from the $k - 1$ step - see (5.10) and (5.11)] to yield the $k = 2$ retrieved profile [Fig. 5.4(b)]. The procedure is then repeated [$k = 3$ - Fig. 5.4(d); $k = 4$ - Fig. 5.4(f)] until $k = K = 5$ [Fig. 5.4(h)]. As regards the accuracy evolution during the *FH* steps, the reconstructions obtained for each k shows that the *GPR* image quality improves as successive iterations are performed [e.g., $k = 1$, Fig. 5.3(e) vs. $k = 5$, Fig. 5.4(h)], as it is also confirmed by the corresponding total error figures (i.e., $\left. \Xi_{tot}^{(k)} \right|_{k=1} = 3.96 \times 10^{-2}$ vs. $\left. \Xi_{tot}^{(k)} \right|_{k=5} = 1.81 \times 10^{-2}$ - Tab. 5.1). Indeed, the size and permittivity of the internal "hollow" region is correctly detected only at the highest frequency [i.e., $k = 5$, $f_k = 600$ MHz - Fig. 5.4(h)], while it appears distorted at the previous *FH* steps [e.g., it seems narrower at $k = 2$, $f_k = 300$ MHz - Fig. 5.4(b)] despite the noiseless scenario.

---

[3]The *GPR* multi-view multi-static setup operates so that when one source is active, the remaining $V - 1 = M = 19$ act as ideal field probes [Fig. 5.1(a)].
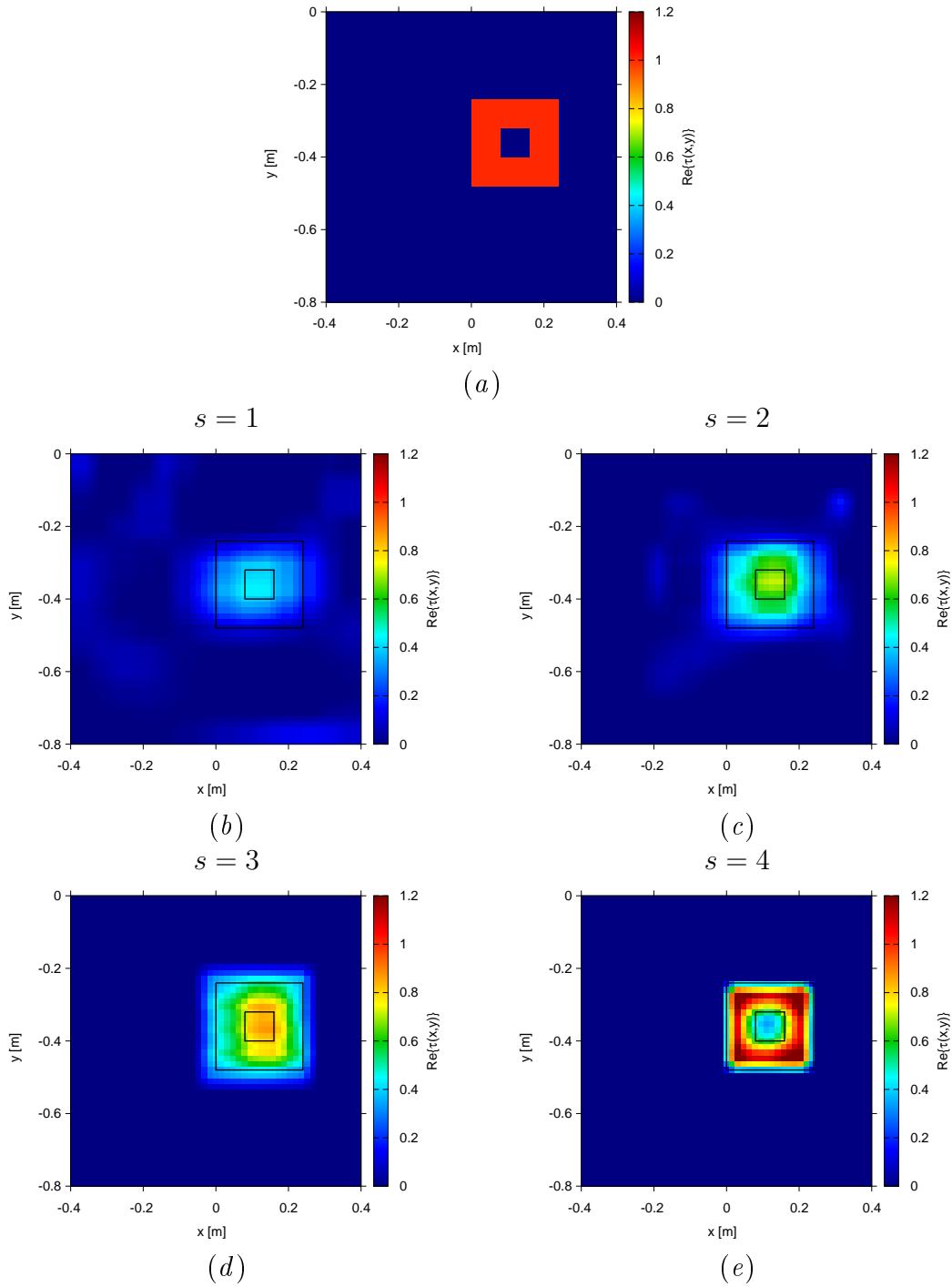
Figure 5.3: *Illustrative Example* ["Hollow square" profile, $\varepsilon_{rB} = 4.0$, $\sigma_B = 10^{-3}$ S/m, $\tau = 1.0$, Noiseless data, $f_1 = 200$ MHz, $k = 1$] Actual (a) and *FHMF-CG* retrieved dielectric profiles when (b) $s = 1$, (b) $s = 2$, (b) $s = 3$, (e) $s = S = 4$.
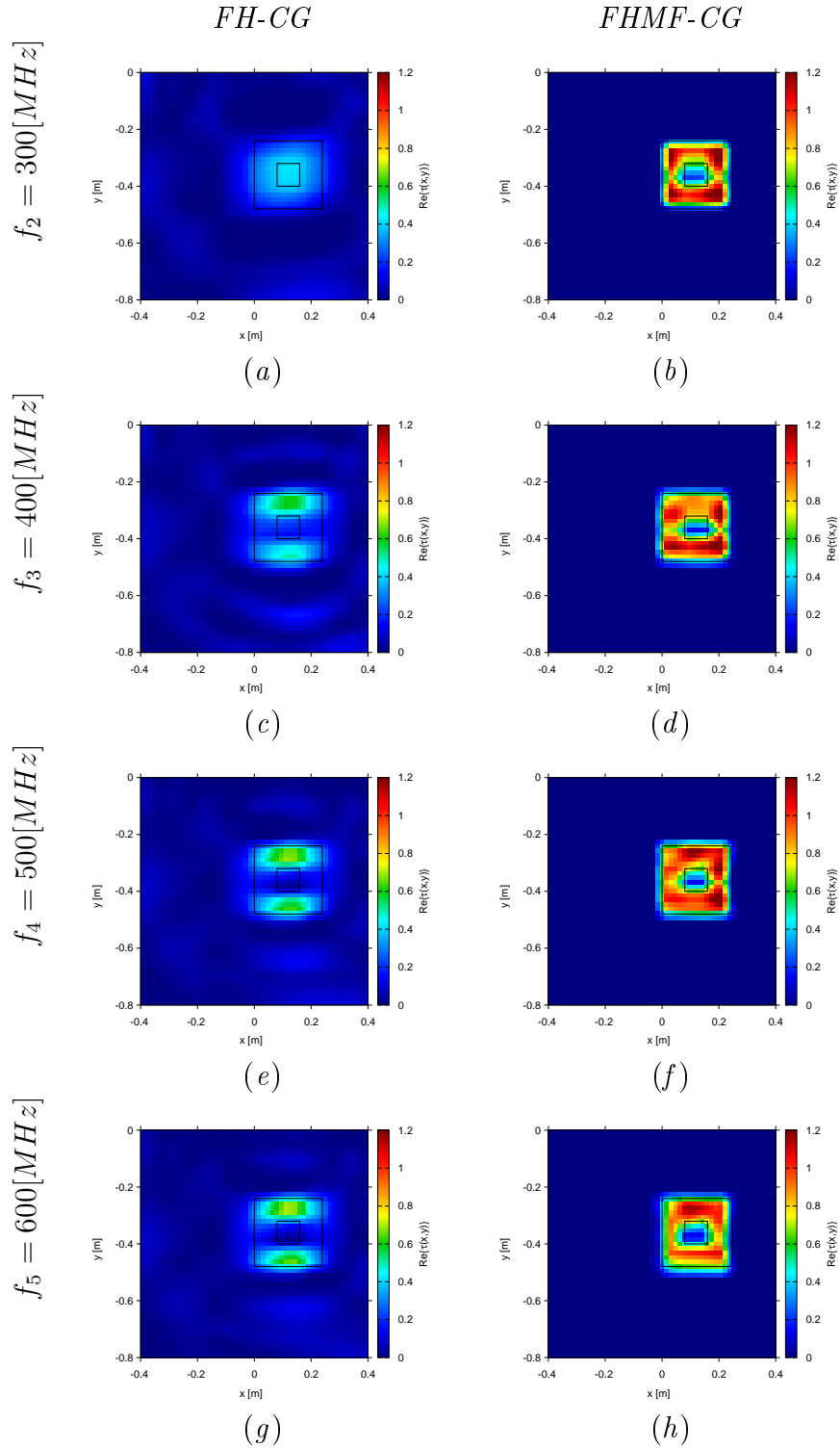
Figure 5.4: *Illustrative Example* ["Hollow square" profile, $\varepsilon_{rB} = 4.0$, $\sigma_B = 10^{-3}$ S/m, Noiseless data] Dielectric profiles retrieved by $(a)(c)(e)(g)$ *FH-CG* and $(b)(d)(f)(h)$ *FHMF-CG* when $(a)(b)$ $q = 2$ $(f_2 = 300$ MHz$)$, $(a)(b)$ $q = 3$ $(f_3 = 400$ MHz$)$, $(a)(b)$ $q = 4$ $(f_4 = 500$ MHz$)$, $(a)(b)$ $q = 5$ $(f_5 = 600$ MHz$)$.

Figure 5.5: *Performance Assessment* ["Hollow square" profile, $\varepsilon_{rB} = 4.0$, $\sigma_B = 10^{-3}$ S/m, $\tau = 1.0$] Behaviour of the integral error vs. the SNR (a), and dielectric profiles retrieved by $(b)(d)$ *FH-CG* and $(c)(e)$ *FHMF-CG* when $(b)(c)$ $SNR = 30$ dB, $(d)(e)$ $SNR = 10$ dB.

The reconstructions obtained with a "bare" *FH* approach (i.e., *FH-CG*), reported in Fig. 5.4 for comparison purposes, remark the effectiveness of the *MF* paradigm. Indeed, even exploiting all the frequency data [i.e., $k = K$], the single-resolution method is only able to roughly detect the location of the scatterer, but completely misses its shape and contrast [i.e., Fig. 5.4(g) vs. Fig. 5.4(h)].

This is further remarked by the corresponding total (e.g., $\Xi_{tot}^{(k)}\Big|_{k=K}^{FHMF-CG} = 1.81 \times 10^{-2}$ vs. $\Xi_{tot}^{(k)}\Big|_{k=K}^{FH-CG} = 1.11 \times 10^{-1}$ - Tab. 5.1), internal (e.g., $\Xi_{int}^{(k)}\Big|_{k=K}^{FHMF-CG} = 1.24 \times 10^{-1}$ vs. $\Xi_{int}^{(k)}\Big|_{k=K}^{FH-CG} = 2.81 \times 10^{-1}$ - Tab. 5.1), and external integral errors (e.g., $\Xi_{ext}^{(k)}\Big|_{k=K}^{FHMF-CG} = 8.71 \times 10^{-3}$ vs. $\Xi_{ext}^{(k)}\Big|_{k=K}^{FH-CG} = 8.78 \times 10^{-2}$ - Tab. 5.1). Even more impressively, the reconstruction obtained at the $k = 1$ step of the *FHMF-CG* are significantly better than those achieved at the $k = K$ step of the *bare* method [i.e., $\frac{\Xi_{tot}^{(k)}\big|_{k=K}^{FH-CG}}{\Xi_{tot}^{(k)}\big|_{k=1}^{FHMF-CG}} \approx 2.8$ - Fig. 5.3(e) vs. Fig. 5.4(g)]. These results support the previous claim concerning the capability of multifocusing approaches to reduce non-linearity issues arising in *GPR* imaging (see Sect. 5.3).

To assess proposed method against noisy data, the same scenario has been investigated assuming $SNR \in [10, 50]$ dB (Fig. 5.5). The plots of the total integral error vs. the noise level show that the *FHMF-CG* provides an accuracy equal to that of the noiseless case until $SNR \approx 40$ dB [i.e., $\frac{\Xi_{tot}^{(K)}\big|^{SNR=40\,dB}}{\Xi_{tot}^{(K)}\big|^{Noiseless}} \approx 1.01$ - Fig. 5.5(a)], while it smoothly degrades for lower SNR values [e.g., $\frac{\Xi_{tot}^{(K)}\big|^{SNR=30\,dB}}{\Xi_{tot}^{(K)}\big|^{Noiseless}} \approx 1.2$ - Fig. 5.5(a)], as it is also confirmed by the profile retrieved when $SNR = 30$ dB [Fig. 5.5(c) vs. Fig. 5.4(h)]. Moreover, the proposed method is able to detect the presence and position of the scatterer even in extreme noise conditions [i.e., $SNR = 10$ dB - Fig. 5.5(e)], although the shape turns out distorted in this case [$\Xi_{tot}^{(K)}\Big|^{SNR=10\,dB} \approx 2.31 \times 10^{-1}$ - Fig. 5.5(a)]. On the contrary, the *FH-CG* single-resolution approach provide unsatisfactory profiles even with moderate noise [$\Xi_{tot}^{(K)}\Big|_{FH-CG}^{SNR=30\,dB} \approx 1.1 \times 10^{-1}$ - Fig. 5.5(b)], and it becomes completely unreliable for lower SNR values [$\Xi_{tot}^{(K)}\Big|_{FH-CG}^{SNR=10\,dB} \approx 7.4 \times 10^{-1}$ - Fig. 5.5(d)].

The robustness of the proposed *FHMF-CG* scheme is then evaluated against a variation of the scatterer contrast. Towards this end, a "square" profile of side 0.16 m centered at $(-0.08, -0.24)$ m has been simulated assuming $\tau \in [1.0, 2.2]$ for different SNR values (Fig. 5.6).

(a)

(b) (c)

(d) (e)
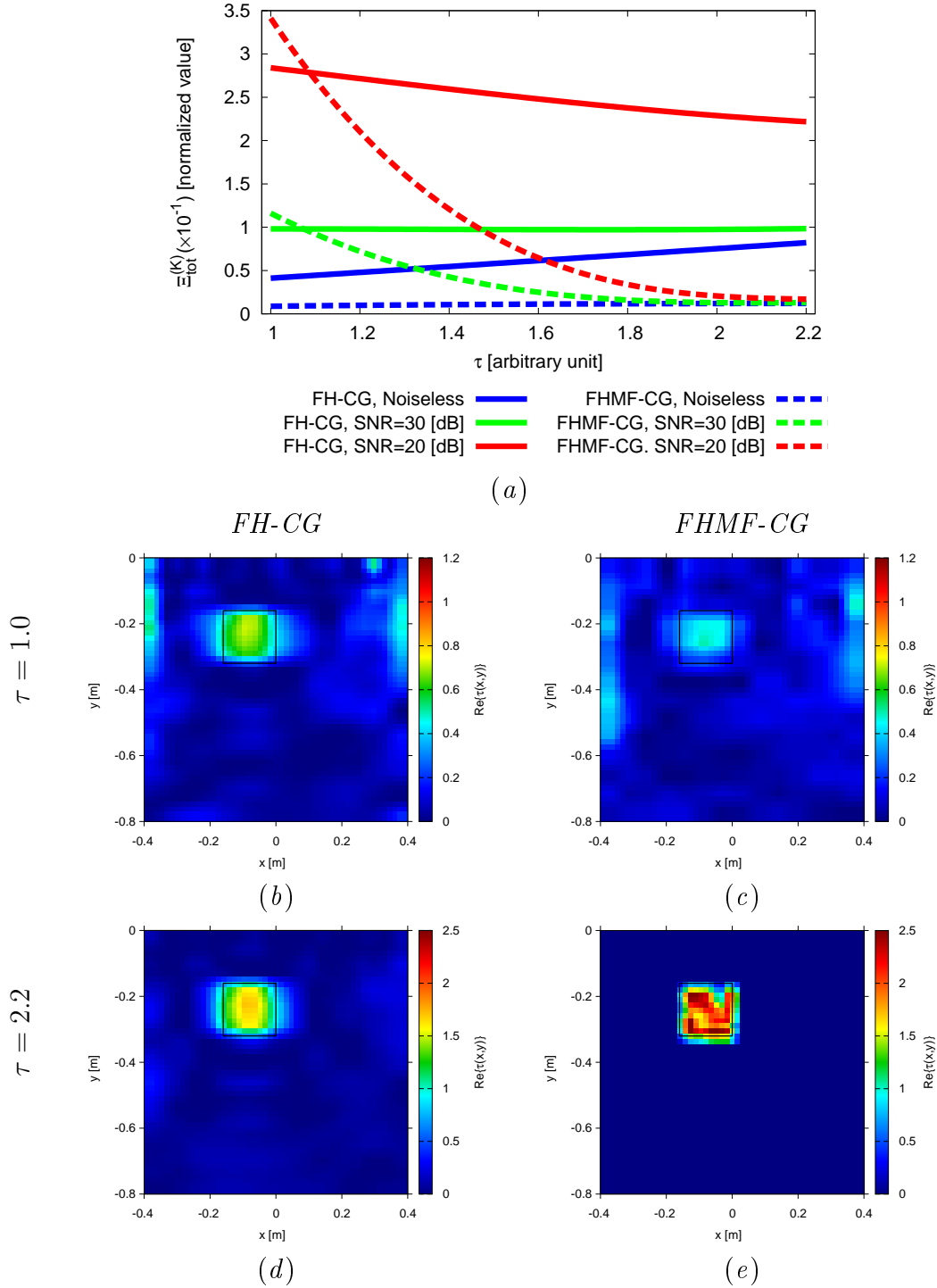
Figure 5.6: *Performance Assessment* ["Square" profile, $\varepsilon_{rB} = 4.0$, $\sigma_B = 10^{-3}$ S/m] Behaviour of the integral error vs. $\t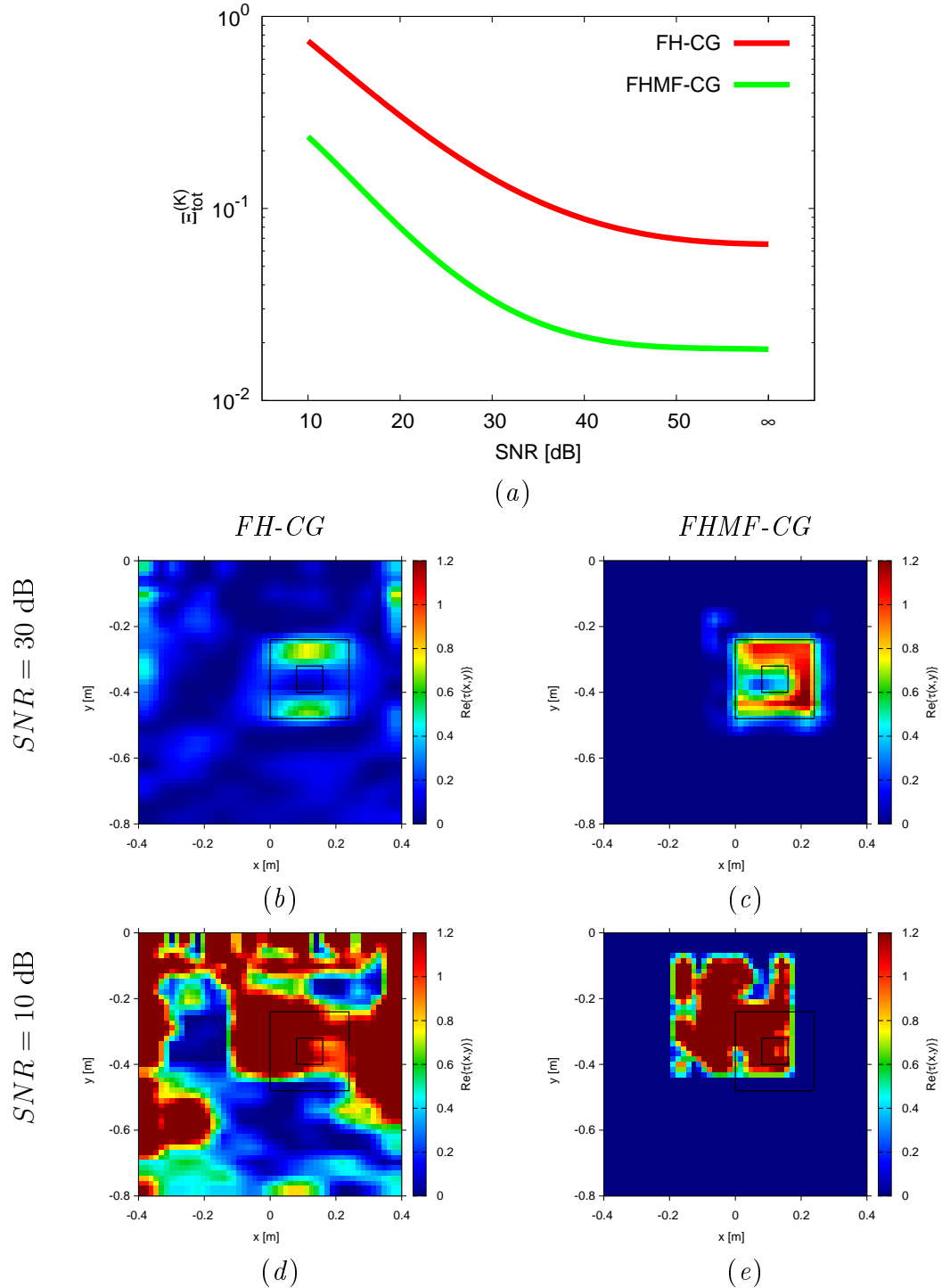au$ (a), and dielectric profiles retrieved by $(b)(d)$ *FH-CG* and $(c)(e)$ *FHMF-CG* when $(b)(c)$ $\tau = 1.0$, $(d)(e)$ $\tau = 2.2$ when $SNR = 30$ dB.

The behaviour of $\Xi_{tot}^{(K)}$ obtained by the *FHMF-CG* in the noiseless case [dashed blue line - Fig. 5.6(a)] shows that an extremely good fidelity is achieved whatever the target contrast [i.e., $\Xi_{tot}^{(K)}\big|_{FHMF-CG} \in [8.7 \times 10^{-3}, 1.2 \times 10^{-2}]$ - Fig. 5.6(a)], which is always significantly better than that shown by the single-resolution method [e.g., $\Xi_{tot}^{(K)}\big|_{FH-CG} \approx 8.2 \times 10^{-2}$ when $\tau = 2.2$ - Fig. 5.6(a)]. However, the *FHMF-CG* accuracy significantly worsens when low τ with moderate noise levels are at hand [$SNR = 30$ dB - green lines, Fig. 5.6(a)].

More in detail, the integral error increases of almost one order of magnitude when $\tau = 2.2 \rightarrow 1.0$ [i.e., $\dfrac{\Xi_{tot}^{(K)}\big|_{FHMF-CG}^{\tau=1.0}}{\Xi_{tot}^{(K)}\big|_{FHMF-CG}^{\tau=2.2}} \approx 9.1$ when $SNR = 30$ dB- Fig. 5.6(a)], reaching a value which is even above that of the corresponding single-resolution method [i.e., $\Xi_{tot}^{(K)}\big|_{FHMF-CG}^{\tau=1.0} \approx 1.16 \times 10^{-1}$ vs. $\Xi_{tot}^{(K)}\big|_{FH-CG}^{\tau=1.0} \approx 9.8 \times 10^{-2}$ - Fig. 5.6(a)]. This behaviour, which is also confirmed when lower SNR values are at hand [$SNR = 20$ dB - red lines, Fig. 5.6(a)], suggests that the multifocusing procedure can exhibit sub-optimal performance when handling low contrast scatterers in high noise scenarios. By analyzing the corresponding reconstructions [$SNR = 30$ dB, $\tau = 1.0$ - Fig. 5.6(c)], it turns out that in this case the *MF* procedure is not able to correctly locate the *RoI* because the artifacts have a contrast whose magnitude is close to that of the actual target [Fig. 5.6(c)]. Accordingly, the *FHMF-CG* method does not effectively allocate the *DoF*s within the domain, resulting in a fidelity similar to that of the single-resolution technique [Fig. 5.6(c) vs. Fig. 5.6(b)]. On the contrary, higher contrast targets are accurately retrieved by the *FHMF-CG* method, since the zooming procedure correctly identifies the *RoI* [e.g., $SNR = 30$ dB, $\tau = 2.2$ - Fig. 5.6(e) vs. Fig. 5.6(d)].

The next set of numerical experiments is devoted to the analysis of the *FHMF-CG* sensitivity to the number of available measurements M (Fig. 5.7). To this end, the retrieval of a "two-bar" profile centered in $(0.16, -0.24)$ m and characterized by $\tau = 1.4$ [Fig. 5.8(a)] has been carried out assuming an increasing number of probes (i.e., $M \in [19, 76]$) in different noise conditions. By observing the plots of the total integral error obtained by the *FHMF-CG* method [Fig. 5.7(b)] for a fixed number of measurements, it turns out that, as expected, the accuracy improves as the SNR enhances [e.g., $\Xi_{tot}^{(K)}\big|_{FHMF-CG}^{SNR=20\,dB} \approx 8.9 \times 10^{-2}$ vs. $\Xi_{tot}^{(K)}\big|_{FHMF-CG}^{SNR=50\,dB} \approx 3.2 \times 10^{-2}$ when $M = 38$ - Fig. 5.7(b)]. Analogously, increasing the number of measurements reduces the error for a fixed SNR [e.g., $\Xi_{tot}^{(K)}\big|_{FHMF-CG}^{M=19} \approx 5.1 \times 10^{-2}$ vs. $\Xi_{tot}^{(K)}\big|_{FHMF-CG}^{M=76} \approx 2.9 \times 10^{-2}$ when $SNR = 30$ dB - Fig. 5.7(b)].
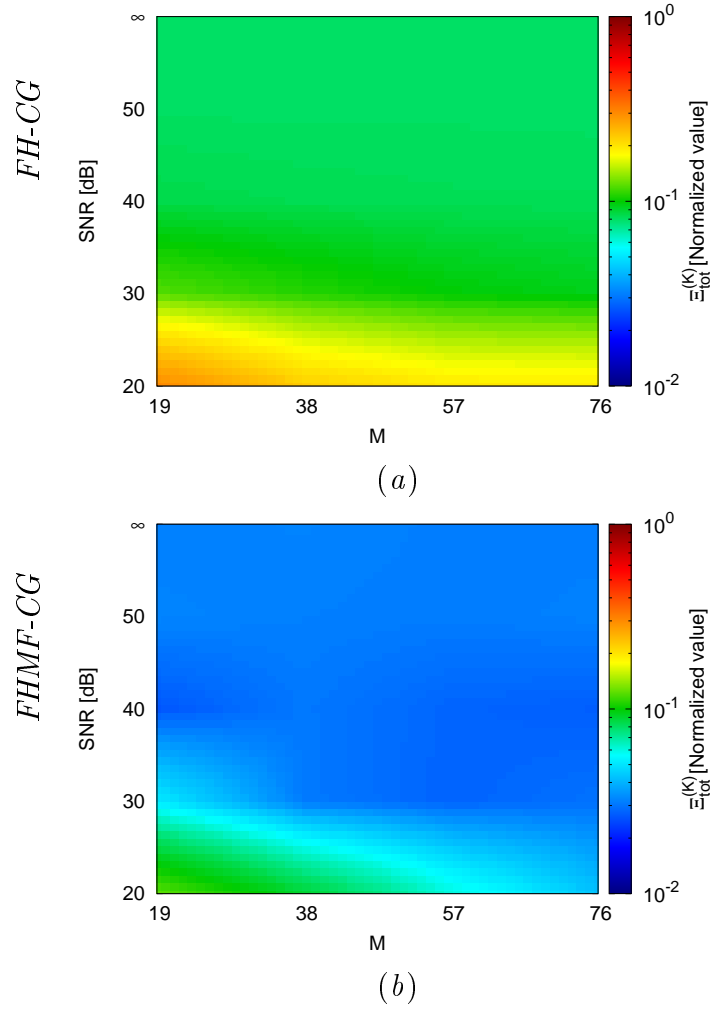
Figure 5.7: *Performance Assessment* ["Two-bar" profile, $\varepsilon_{rB} = 4.0$, $\sigma_B = 10^{-3}$ S/m, $\tau = 1.4$] Behaviour of the total integral error versus M and SNR for (a) *FH-CG* and (b) *FHMF-CG*.
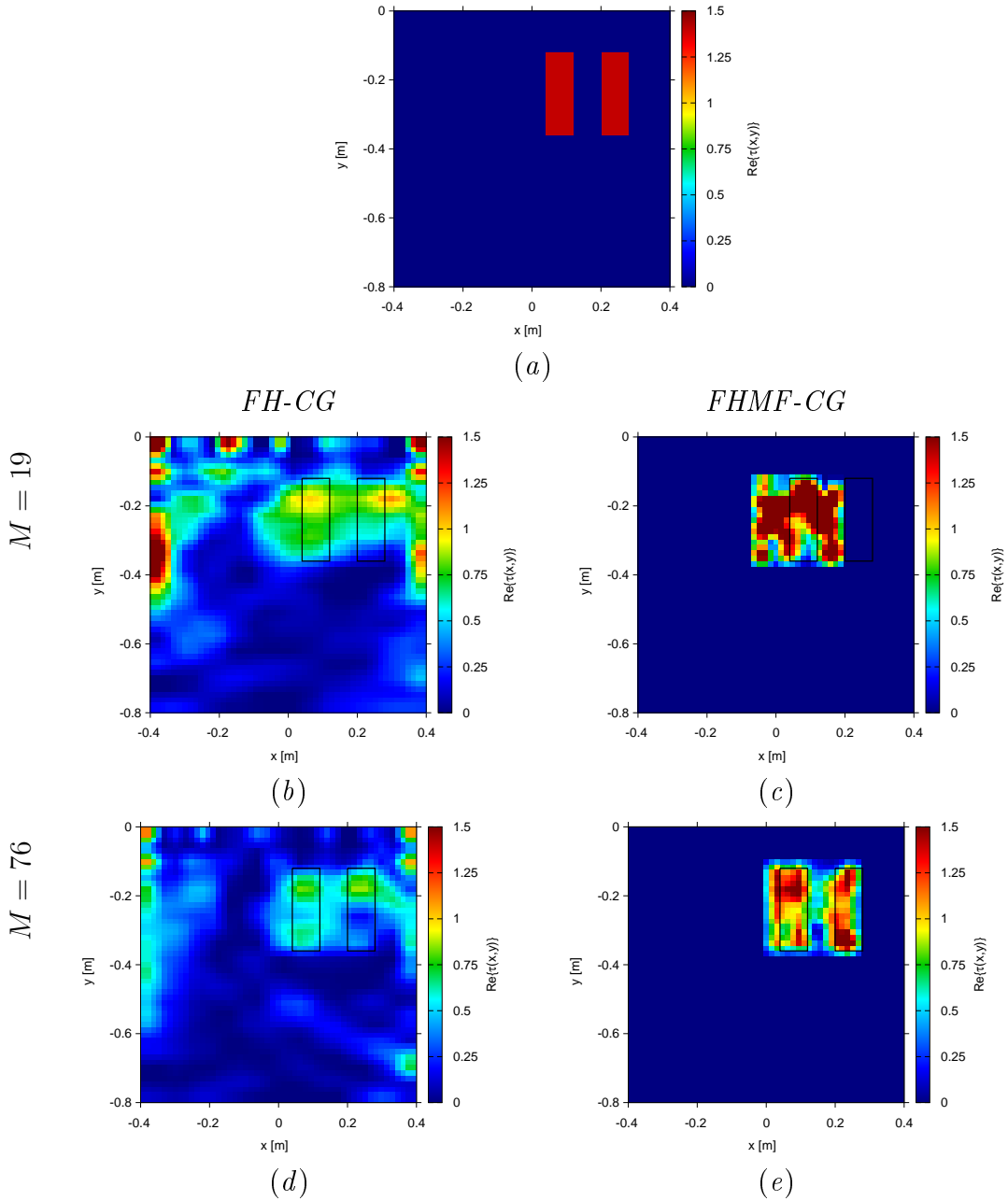
Figure 5.8: *Performance Assessment* ["Two-bar" profile, $\varepsilon_{rB} = 4.0$, $\sigma_B = 10^{-3}$
S/m, $\tau = 1.4$, $SNR = 20$ dB] Actual (a) and dielectric profiles retrieved by
(b)(d) *FH-CG* and (c)(e) *FHMF-CG* when (b)(c) $M = 19$, (d)(e) $M = 76$.

Moreover, the plots in Fig. 5.7 show that (i) the *FHMF-CG* approach never
exceeds a $\approx 10\%$ reconstruction error, even in the worst conditions [i.e., $SNR =$
20 dB, $M = 19$ - Fig. 5.7(b)], and (ii) whatever the noise level and M value,
the multifocusing procedure outperforms the *FH-CG* one [Fig. 5.7(b) vs. Fig.

5.7(a)]. Furthermore, the reconstructions in Fig. 5.8 suggest that the *FHMF-CG* is able to exploit the additional measurements to significantly enhance its fidelity especially in low SNR conditions [i.e., $SNR = 20$ dB - Fig. 5.8(c) vs. Fig. 5.8(e)], therefore achieving a satisfactory accuracy [i.e., $\left.\Xi_{tot}^{(K)}\right|_{FHMF-CG}^{SNR=20\,dB} \approx 4.2 \times 10^{-2}$ when $M = 76$ - Fig. 5.8(e)]. On the contrary, the *FH-CG* technique does not exhibit a sensible performance improvement in this case [Fig. 5.8(b) vs. Fig. 5.8(d)].

f_k [MHz]	FH-CG			FHMF-CG		
	$\Xi_{tot}^{(k)}$	$\Xi_{int}^{(k)}$	$\Xi_{ext}^{(k)}$	$\Xi_{tot}^{(k)}$	$\Xi_{int}^{(k)}$	$\Xi_{ext}^{(k)}$
200.0	1.18×10^{-1}	3.61×10^{-1}	5.24×10^{-2}	3.96×10^{-2}	1.31×10^{-1}	2.98×10^{-2}
300.0	1.06×10^{-1}	3.51×10^{-1}	6.32×10^{-2}	2.79×10^{-2}	1.44×10^{-1}	1.73×10^{-2}
400.0	1.02×10^{-1}	3.01×10^{-1}	7.11×10^{-2}	1.85×10^{-2}	1.72×10^{-1}	5.00×10^{-3}
500.0	9.56×10^{-2}	2.86×10^{-1}	7.18×10^{-2}	1.84×10^{-2}	1.61×10^{-1}	4.50×10^{-3}
600.0	1.11×10^{-1}	2.81×10^{-1}	8.78×10^{-2}	1.81×10^{-2}	1.24×10^{-1}	8.71×10^{-3}
Δt	7.0×10^3 [s]			2.5×10^3 [s]		

Table 5.1: *Illustrative Example* ["Hollow square" profile, $\varepsilon_{rB} = 4.0$, $\sigma_B = 10^{-3}$ S/m, $\tau = 1.0$, Noiseless data] Figures of merit.

Finally, as for the computational issues, Tab. 5.1 also reports the inversion time Δt required when handling the "hollow-square" scatterer in Fig. 5.3(a). For the sake of fairness, all simulations have been performed assuming non-optimized Fortran implementations of the procedures running on a standard Linux laptop (with single-core 2.1 GHz CPU). As it can be noticed, despite the multi-frequency nature of the considered GPR prospecting problem, the proposed *FHMF-CG* approach is able to provide the final reconstruction in less than 42 minutes (i.e., $\Delta t \approx 2.5 \times 10^4$ s - Tab. 5.1), while the single resolution method (which has to solve a larger problem at each FH step [91]) requires above 116 minutes to complete. This result, which does not depend on the target features (similar Δt values have been obtained in all the numerical examples), highlights the efficiency of the considered multi-focusing scheme, which depends on its capability to decompose a large inversion problem in a sequence of smaller ones with reduced nonlinearity [54].

5.4.2.2   Comparisons with State-of-the-Art Methods

The next set of numerical experiments is aimed at assessing the proposed *FHMF-CG* method with respect to comparable state-of-the-art approaches. Towards this end, the setup in [96] has been considered as the first benchmark.
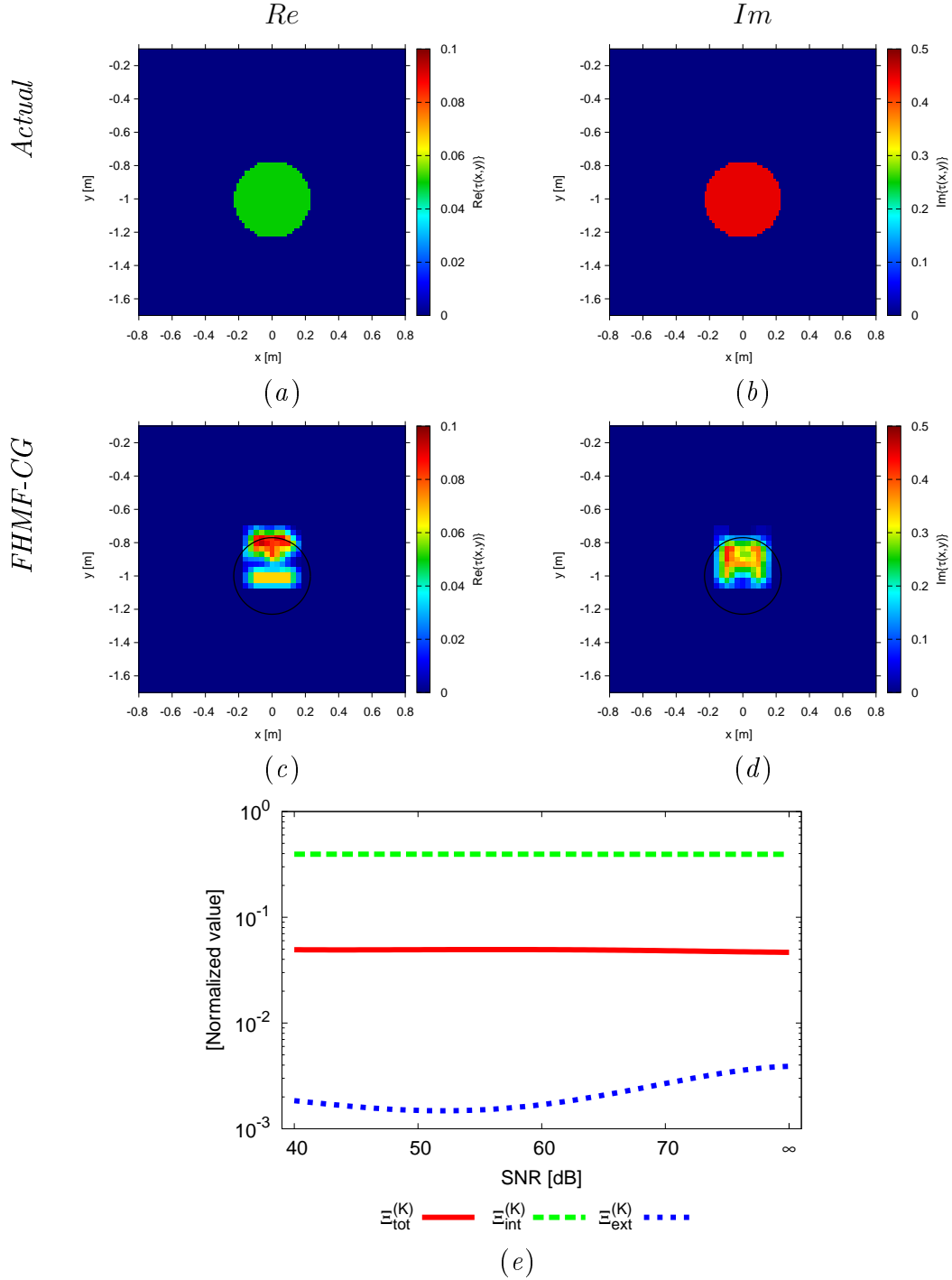
Figure 5.9: *Comparative Assessment* ["Circle" profile [96], $\varepsilon_{rB} = 9.0$, $\sigma_B = 10^{-2}$
S/m, $\varepsilon = 9.05$, $\sigma = 0.0$, $k = K = 3$] Real $(a)(c)$ and imaginary parts $(b)(d)$ of
the actual $(a)(b)$ and *FHMF-CG* retrieved profile when $SNR = 50$ dB $(c)(d)$,
and (e) behaviour of the integral error vs. the SNR.

73

(a)

(b)

(c)
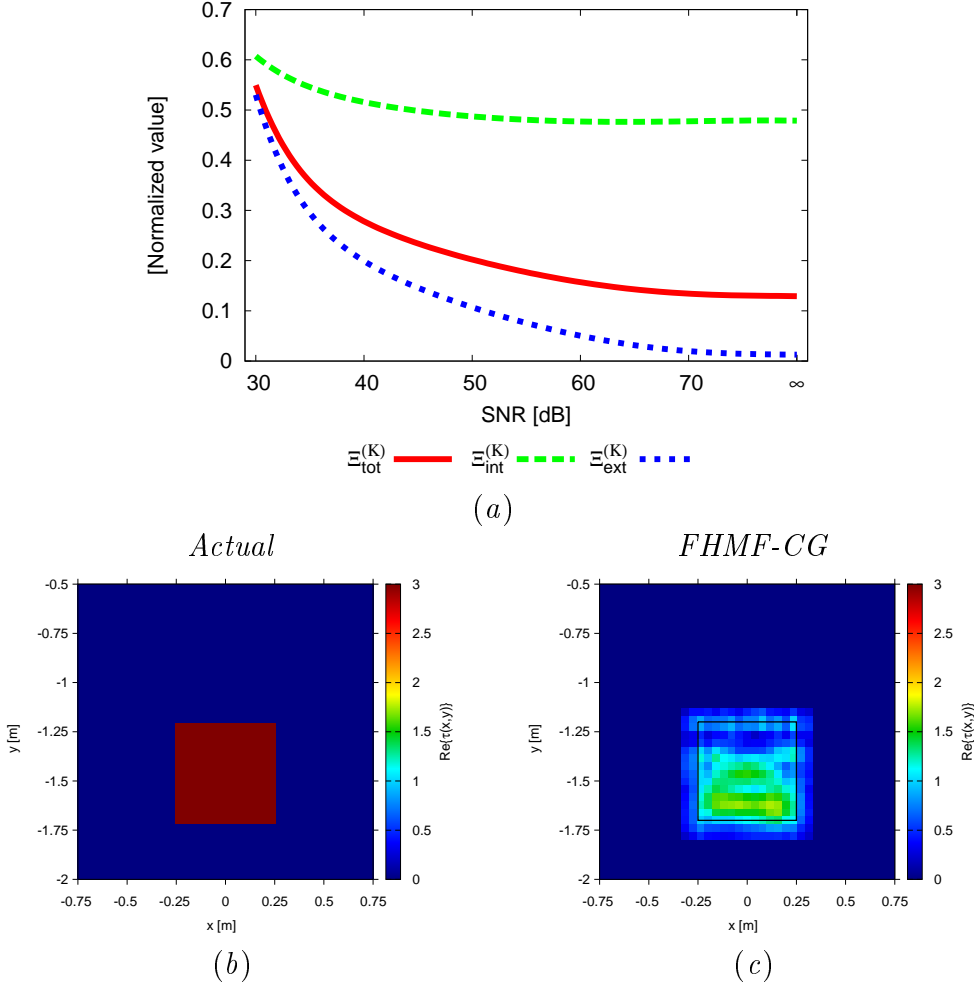
Figure 5.10: *Comparative Assessment* ["Large square" profile [87], $\varepsilon_{rB} = 9.0$, $\sigma_B = 10^{-2}$ S/m, $\tau = 3.0$, $k = K = 6$] (a) Behaviour of the integral error vs. the SNR and (b) actual and (c) *FHMF-CG* retrieved profiles when $SNR = 50$ dB.

More specifically, a "circle-shaped" target centered at $(0.0, -1.0)$ m and with radius 0.23 m [Figs. 5.9(a)-5.9(b)], characterized by $\varepsilon = 9.05$ and $\sigma = 0.0$, has been placed in a square investigation domain of side 1.6 m, centered at $(0.0, -0.9)$ m (i.e., with a -0.1 m offset with respect to the air-soil interface) with background dielectric properties $\varepsilon_{rB} = 9.0$, $\sigma_B = 10^{-2}$ S/m [96]. The scenario has been illuminated by $V = 21$ sources equispaced on a 2 m line placed on the air-soil interface, and the obtained field has been sampled by $M = 25$ probes equally spaced on the same line [96].
The plots of the real [Fig. 5.9(c)] and imaginary part [Fig. 5.9(d)] of the contrast profile obtained at the $k = K = 3$ step assuming the same SNR levels of [96][4] point out that the proposed approach is able to correctly retrieve the number and

---

[4]Since the SNR in [96] is not defined as in (5.19), the "translation" of the employed SNR numerical values has been carried out before performing the numerical simulations, for consis-

position the scatterers, and to approximatively yield also its shape and contrast
[e.g., Fig. 5.9(d) vs. Fig. 5.9(b)] despite the significant losses in the soil (i.e.,
$\sigma_B = 10^{-2}$ S/m). By comparing these results with the one obtained with the
linear *TSVD*-based inversion approach discussed in [96], it turns out that the
proposed method yield a more accurate estimation of the size and location of the
target, as well as a less blurred background [i.e., Fig. 12 in [96] vs. Fig. 5.9(d)].
Indeed, the scatterer center is reliably approximated by the *FHMF-CG* [Figs.
5.9(c)-5.9(d)], while a non-negligible offset was shown in [96]. Moreover, a similar
accuracy can be obtained in a wide set of noise conditions [i.e., $SNR \geq 40$ dB
- Fig. 5.9(e)]. These results suggests that using a fully non-linear methodology
(handled through a multi-focusing approach) can provide an improved accuracy
with respect to approximated formulations (i.e., distorted Born [96]) even in
scenarios where these approximations are acceptable.

Analogous considerations arise when applying the *FHMF-CG* method to the test
case presented in [87]. In this case, a square scatterer of side 0.5 m centered at
$(0.0, -1.45)$ m [$\tau = 3.0$ - Fig. 5.10(b)] has been imaged assuming $V = 21$ sources
and $M = 20$ probes displaced on a 3 m-long line on the air-soil interface [87].
Towards this end, a 1.5×2.0 m $\mathcal{D}$ ($\varepsilon_{Rb} = 9.0$, $\sigma_B = 10^{-2}$ S/m) centered at
$(0.00, -1.25)$ m (0.5 m depth) has been considered [87]. By comparing the plot
of the retrieved profile at the $k = K = 6$ *FH* step [$SNR = 50$ dB - Fig. 5.10(c)]
with the corresponding reconstruction shown obtained with a linear inversion
algorithm under the *Distorted Born Approximation* (i.e., Fig. 7 in [87]) it turns
out that both the shape and the size of the target are more accurately retrieved
by the *FHMF-CG* method.

Moreover, the plot of the integral errors vs. the SNR show that the obtained
performance is quite stable with respect to the noise level [i.e., $\Xi_{tot}^{(K)} < 2.1 \times 10^{-1}$
when $SNR > 50$ dB - Fig. 5.10(a)], and it smoothly degrades for lower and
lower SNRs [Fig. 5.10(a)]. The reduced *FHMF-CG* accuracy when $SNR < 50$
dB [Fig. 5.10(a)] is actually caused by the depth of the considered investigation
domain (i.e., $y \in [-2, -0.5]$ m) and by the lossy nature of the soil (i.e., $\sigma_B = 10^{-2}$
S/m), which cause a very low scattered field to be received by the probes (i.e.,
at $SNR = 30$ dB, the signal-to-noise ratio computed over the scattered field
turns out equal to ≈ 10 dB in this case), despite the non-negligible contrast [i.e.,
$\tau = 3.0$ - Fig. 5.10(b)].

5.4.3   Experimental Validation

The last validations are concerned with the inversion of experimental data. To-
wards this end, the measured *GPR* radargrams in Area 5 of the Near Surface
Geophysical Group (*NSGG*) Test Site 2 [97] using the *MalaX3M GPR* equipment
[103] have been considered [Fig. 5.11(c)].

---

tency.

(a)
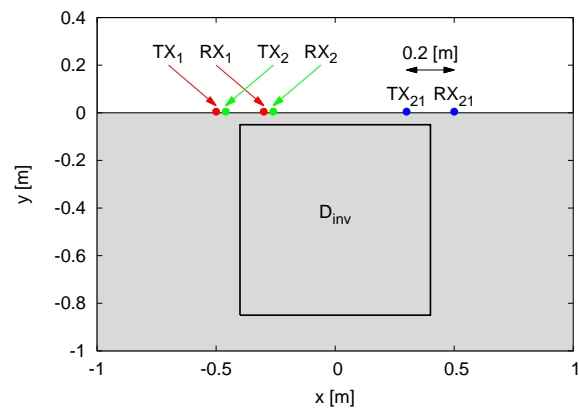
(b)
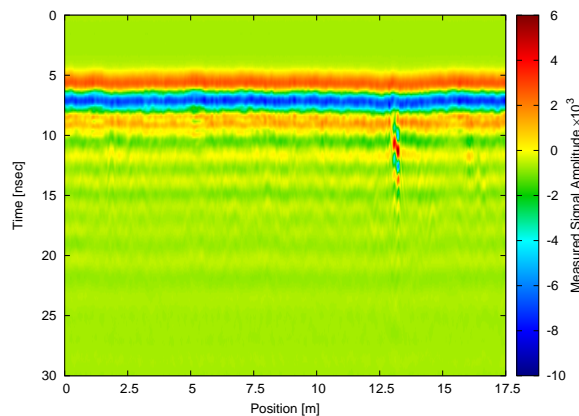
(c)

Figure 5.11: *Experimental Validation - Dataset* [97] - Photo of the experimental setup (courtesy of Prof. M. Guy) (a), geometry of the problem (b), and full measured radargram available in [97] (c).

(a)

(b)
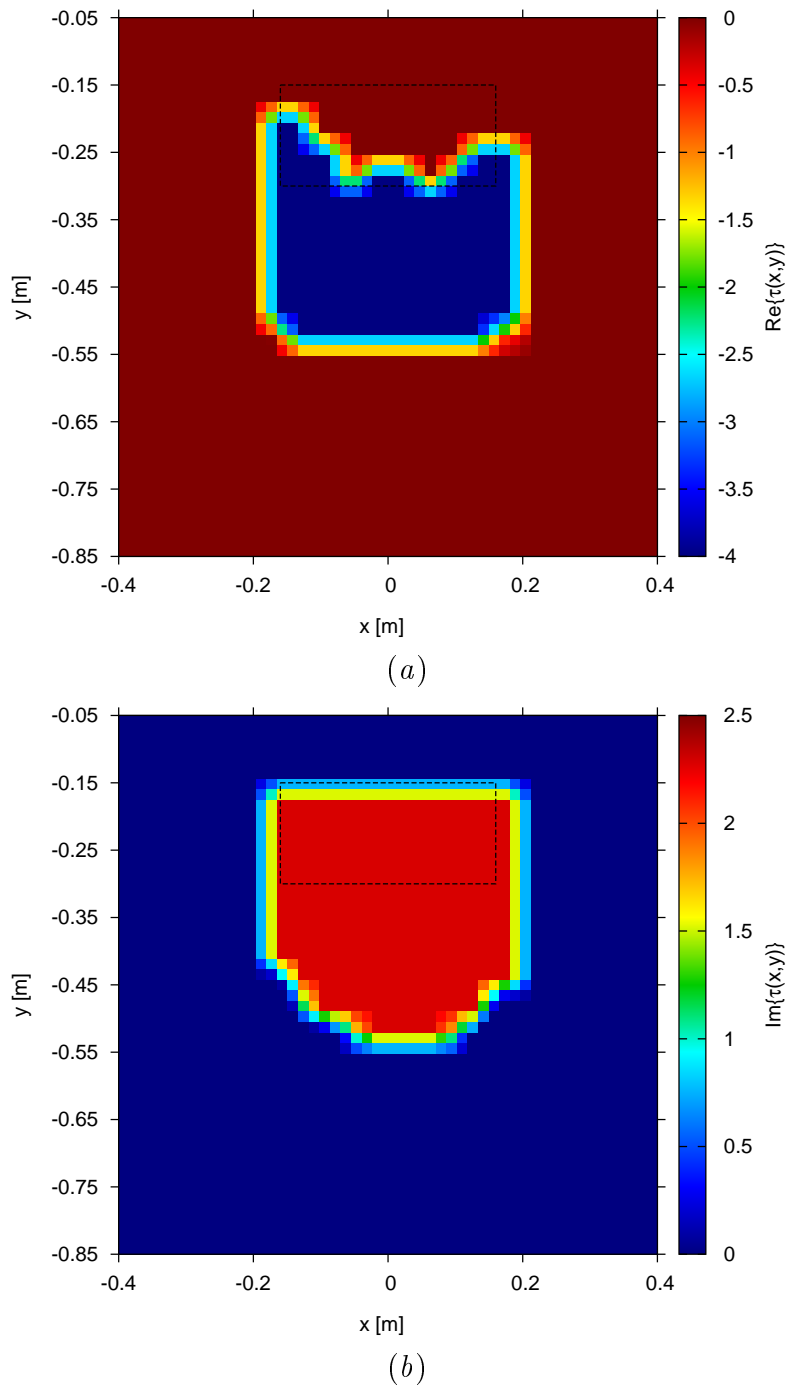
Figure 5.12: *Experimental Validation - Dataset* [97] $[V = 21]$ Real (a) and
imaginary parts (b) of the *FHMF-CG* retrieved profile.

77
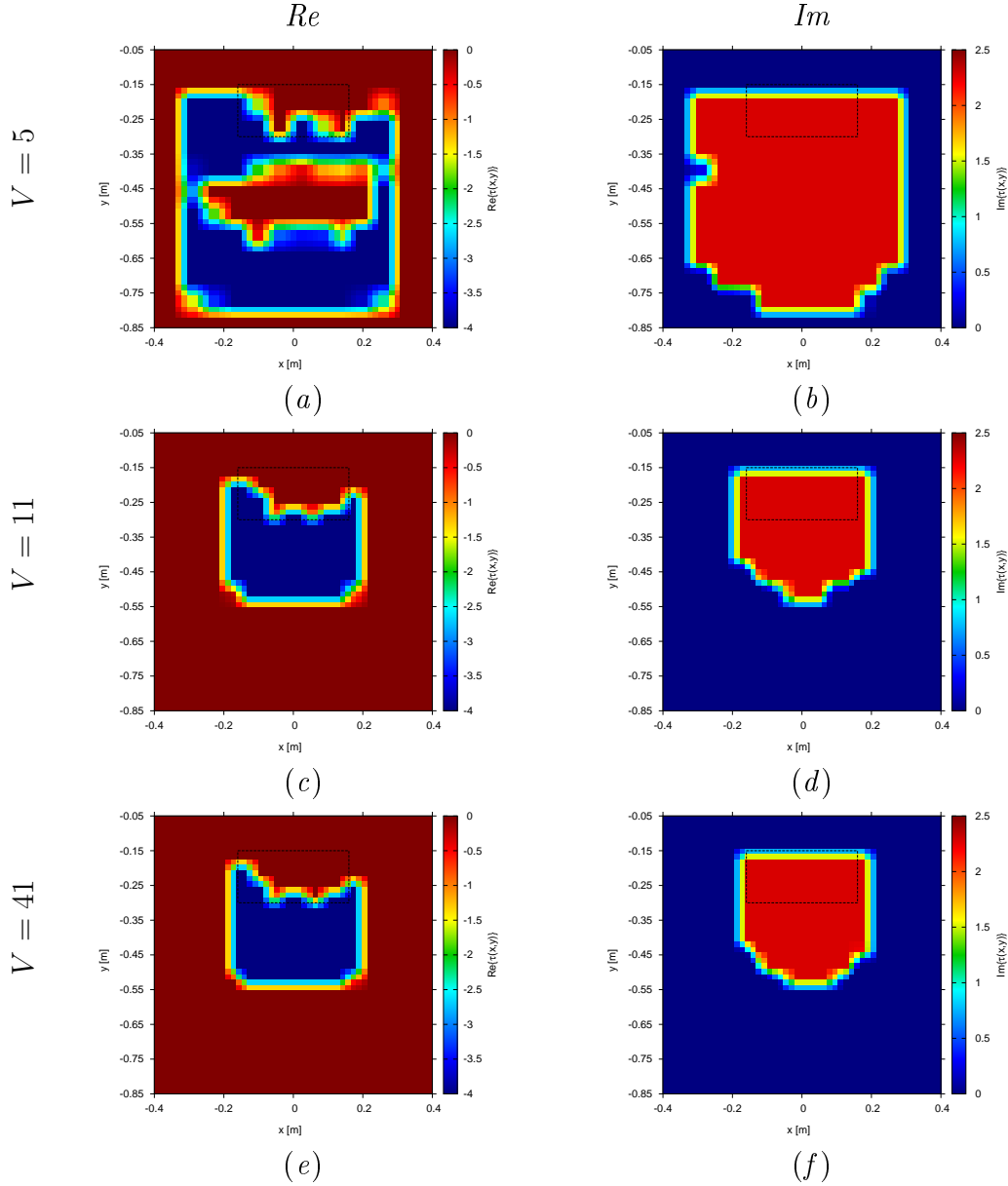
Figure 5.13: *Experimental Validation - Dataset* [97] - Real $(a)(c)(e)$ and imaginary parts $(b)(d)(f)$ of the *FHMF-CG* retrieved profiles when $(a)(b)$ $V = 5$, $(c)(d)$ $V = 11$, and $(e)(f)$ $V = 41$.

The experimental data refer to the setup in Fig. 5.11(a), in which an empty box ($\varepsilon_r = 1.0$, $\sigma = 0.0$ S/m) of size $0.32 \times 0.25 \times 0.15$ m is buried 0.15 m below the soil surface [104], which is assumed to be characterized by $\varepsilon_{rB} = 5.0$, $\sigma_B = 38 \times 10^{-3}$ S/m. The scenario is investigated through a single pair of transmitting-receiving antennas positioned at the air-soil interface, which is moved over the investigation domain [one trace every 0.02 m - Fig. 5.11(b)]. The transmitter radiates a Gaussian monocycle pulse with [100, 300] MHz 3 dB bandwidth [97][104], and the

78

resulting field is collected by the built-in receiver ($M = 1$) which is horizontally
separated by 0.2 m [Fig. 5.11(b)]. A square investigation domain $\mathcal{D}$ of side 0.8
m and centered at $(0.00, -0.45)$ m is considered for the inversion [Fig. 5.11(b)].
The plot of the retrieved real [Fig. 5.12(a)] and imaginary parts of the contrast
[Fig. 5.12(b)] obtained using $V = 21$ source positions [uniformly placed over a 0.8
m range - Fig. 5.11(b)] show that the proposed *FHMF-CG* approach is able to
correctly identify the presence, horizontal extension, and depth of the target [e.g.,
Fig. 5.12(a)], while the vertical extension is overestimated [e.g., Fig. 5.12(b)].
However, this behaviour is mainly related to low number of measurements ($M =
1$), and to the fact that the method does not account for the non-ideal nature of
the source/probe antennas (i.e., shielded bowties [97][104]), and well as for any
roughness or non-homogeneity in the soil.
In order to assess the variation in the retrieval accuracy with the number of ac-
quisitions, the same experiment has been repeated considering $V = \{5, 11, 41\}$
source positions uniformly distributed in the 0.8 m range (Fig. 5.13). By com-
paring the plots of the retrieved profiles when $V = 11$ [Figs. 5.13(c)-5.13(d)]
and $V = 41$ [Figs. 5.13(e)-5.13(f)] it turns out that the number of views does
not significantly affect the *GPR* prospecting accuracy, unless a very few data are
used [$V = 5$ - Figs. 5.13(a)-5.13(b)]. Moreover, it is worth observing that $V = 11$
measurements, corresponding to a spatial sampling rate of 0.08 m, are sufficient
for the *FHMF-CG* method to retrieve the dielectric properties, horizontal size,
and depth of the buried target illuminated through standard *GPR* instruments.

5.5   Discussions

An innovative information acquisition approach based on a nested frequency-
hopping multi-focusing inversion technique has been introduced for the solution
of 2D *GPR* prospecting problems. Towards this end, an external iterative *FH*
procedure has been proposed to handle multi-frequency *GPR* data, and its com-
bination with an internal multi-resolution loop able to mitigate local minima
issues in the associated inverse scattering problem has been presented. To min-
imize the arising multi-focusing cost function, a local search strategy based on
CG has been implemented and integrated. The proposed *FHMF-CG* method
has been validated against synthetic and measured *GPR* data, and a compara-
tive assessment has been discussed.
From the methodological viewpoint, the main contributions of the present work
include (i) the derivation of a multi-focusing scheme that, unlike state-of-the-art
methods [54][72], is suitable for *GPR* prospecting and can handle time-domain
data through Fourier processing, and (ii) the introduction of a frequency-hopping
technique which, at each frequency step, suitably initializes both the total field
[Eq. (5.11)] and the contrast [Eq. (5.10)] using the acquired information, unlike
[91]-[93].
The numerical and experimental validation has pointed out the following main

outcomes:

- the *FHMF-CG* method outperforms its single-resolution counterpart in terms of accuracy whatever the noise level, contrast, measurement setup, and target properties, except for very weak scatterers in low SNR scenarios in which the two methods provide comparable fidelities;

- thanks to its multi-focusing nature, the proposed approach is significantly more numerically efficient than a bare *FH-CG* technique (Tab. 5.1);

- the introduced algorithm favourably compares with state-of-the-art techniques based on linear formulations and *TSVD* solvers (Sect. 5.4.2.2);

- the *FHMF-CG* technique can be effectively used to detect the position, depth, and dielectric properties of buried objects starting from few raw *GPR* experimental measurements without the need to accurately model the actual soil properties and antenna geometries (Sect. 5.4.3).

Future works, beyond the scope of this thesis, will be aimed at extending the proposed methodology to full 3D *GPR* scenarios. Moreover, the possibility to improve the method accuracy through accurate modelling of the employed transmitting/receiving antennas within the inversion process is currently under investigation.

Chapter 6

Conclusions

In this chapter, a final numerical set of simulations is provided and commented with the aim of comparing the different inversion strategies presented in this thesis. Moreover, some final considerations on the presented methodologies for subsurface imaging are drawn, highlighting potentialities and limits of each technique.

6.1 Comparison Between Different Approaches

In order to assess what are the potentialities as well as the limits of the proposed inversion techniques presented in this thesis, a final numerical assessment is here presented. The considered benchmark scenario consists of a square investigation domain of side 0.8 m centered at $(0.00, -0.4)$ m which is illuminated by $V = 16$ sources radiating a time-domain Gaussian monocycle pulse [Fig. 5.1(b)] with spectrum centered at 300 MHz and 3 dB bandwidth covering the $[200.0, 600.0]$ MHz range [Fig. 5.1(c)]. The lower half space is occupied by soil, with $\varepsilon_{rB} = 4.0$ and $\sigma_B = 10^{-3}$ S/m.

(a) $\qquad\qquad\qquad\qquad$ (b)

Figure 6.1: *Comparative Assessment (Square Scatterer at Different Depths - $L =$ 0.16 m, ($x_c = 0.0$ m, $\varepsilon_r = 5.5$, $\sigma = 0.01$ S/m [$\tau = 1.5$], $\varepsilon_{rB} =$4.0, $\sigma_B =$0.01 S/m, $SNR = 20$ dB) - Location of the illuminating sources and of the measurement points for the (a) cross-borehole and (b) half space configurations.*

For comparison purposes, two measurement configurations are considered, both considering a set of $M = 15$ probes [1], co-located with the sources to form a cross-borehole [Fig. 6.1(a)] and a half space [Fig. 6.1(b)] setup. Concerning the cross-borehole setup [Fig. 6.1(a)], the sources/probes are equally spaced along two vertical lines at coordinates $x = \pm 0.5$ m, starting from a depth of $y_{min} = -1.0$ [m] up to a depth of $y_{max} = 0.0$ m. For the half space setup [Fig. 6.1(b)] the sources/probes are equally spaced on a 1 m line which is located at $y = 0.04$ m above the interface. As a benchmark profile, a "square" profile of side 0.16 m [Fig. 6.2] centered at $x_c = 0.0$ m and located at different depths inside D_{inv} has been simulated assuming a contrast function of $\tau = 1.5$. More precisely, the target barycentre is located at a depth of $y_c = -0.16$ m for the "*top*" configuration [Fig. 6.2(a)], $y_c = -0.4$ m for the "*intermediate*" configuration [Fig. 6.2(b)] and $y_c = -0.64$ m for the "*bottom*" configuration.

---

[1] The *GPR* multi-view multi-static setup operates so that when one source is active, the remaining $V - 1 = M = 15$ act as ideal field probes.

(a)

(b)

(c)

Figure 6.2: *Comparative Assessment (Square Scatterer at Different Depths -* $L = 0.16\,m$, ($x_c = 0.0\,m$, $\varepsilon_r = 5.5$, $\sigma = 0.01$ S/m [$\tau = 1.5$], $\varepsilon_{rB} = 4.0$, $\sigma_B = 0.01$ S/m, $SNR = 20$ dB) - Actual target used for the comparison for (a) "*top*" ($y_c = -0.16\,m$), (b) "*intermediate*" ($y_c = -0.4\,m$) and (c) "*bottom*" ($y_c = -0.64\,m$) configurations.

The SNR computed according to (5.19) is such that a resulting $SNR = 20$ dB can be estimated on the scattered field at the central frequency of 300 MHz.

As a first analysis, we consider the retrieved profiles when the single-frequency $IMSA-IN$ technique presented in Chapter 4 is employed in order to recover the electromagnetic distributions of the investigated targets [Fig. 6.3]. The $IMSA-IN-SOBA$ method presented in Chapter 3 will not be considered here, since it has been already widely verified in Chapter 4 that its performances are lower wrt the full non-linear approach (i.e., without the $SOBA$ approximation). Moreover, the same parameters considered for the numerical results shown in Chapter 4 are considered (i.e., $N = 100$, $Q = 50$, $\alpha = 0.9$, $I_{max,s=1} = 20$, $I_{max,s>1} = 1000$ and $S = 4$). In particular, the retrieved profiles are shown when using both a cross-borehole [Fig. 6.3(a)(b)(c)] and a half space [Fig. 6.3(d)(e)(f)] measurement configuration. By looking at the retrieved profiles in Fig. 6.3, it is clear that the performances achievable with a cross-borehole setup significantly overcome those obtainable with a half space setup. Moreover, if on the one hand the performances for the cross-borehole setup seem quite constant when changing the depth of the unknown target, on the other hand the retrieved contrasts when using a half space setup undergo a significant and progressive degradation when increasing the depth of the scatterer inside D_{inv} [i.e., passing from Fig. 6.3(d) to Fig. 6.3(e) and to Fig. 6.3(f)]. As a matter of fact, when the scatterer is at a depth of $y_c = -0.64$ m [i.e., corresponding to $1.28\lambda_b$ at the considered frequency of 300 MHz, Fig. 6.3(f)], the inversion technique turns out to be absolutely uncapable to recover the shape and the electromagnetic characteristics of the target. Such a behaviour can be motivated by the fact that half space setups are strongly aspect-limited, given the fact that sources and measurement points are both located only above the interface [Fig. 6.1(b)], thus allowing the collection of a very limited amount of information to perform the inversion. On the contrary, a cross-borehole setup [Fig. 6.1(a)], even if still aspect-limited, allows the collection of a larger amount of information with the same number of sources V and measurements M, since transmissions can "cross" the investigation domain D_{inv} and hence the targets buried within it. Moreover, sources and measurement points are located at different depths inside the soil, so that more information can be collected for targets which are buried at significant depths inside D_{inv}. The above considerations are further confirmed by the total reconstruction error Ξ_{tot} obtained by the $IMSA-IN$ method for the two setups. In fact, we have for the "top" configuration [Fig. 6.2(a)] $\Xi_{tot}|_{cross-borehole}^{"top"} \approx 8.66 \times 10^{-3}$ [Fig. 6.3(a)] vs. $\Xi_{tot}|_{half\,space}^{"top"} \approx 1.83 \times 10^{-2}$ [Fig. 6.3(d)], for the "$intermediate$" configuration [Fig. 6.2(b)] $\Xi_{tot}|_{cross-borehole}^{"intermediate"} \approx 3.72 \times 10^{-3}$ [Fig. 6.3(b)] vs. $\Xi_{tot}|_{half\,space}^{"intermediate"} \approx 2.91 \times 10^{-2}$ [Fig. 6.3(e)], while for the "$bottom$" configuration [Fig. 6.2(c)] $\Xi_{tot}|_{cross-borehole}^{"bottom"} \approx 4.12 \times 10^{-3}$ [Fig. 6.3(c)] vs. $\Xi_{tot}|_{half\,space}^{"bottom"} \approx 4.22 \times 10^{-2}$ [Fig. 6.3(f)]. The reconstruction error obtained for this latter configuration appears more that one order of magnitude larger when considering an half space setup wrt a cross-borehole setup.

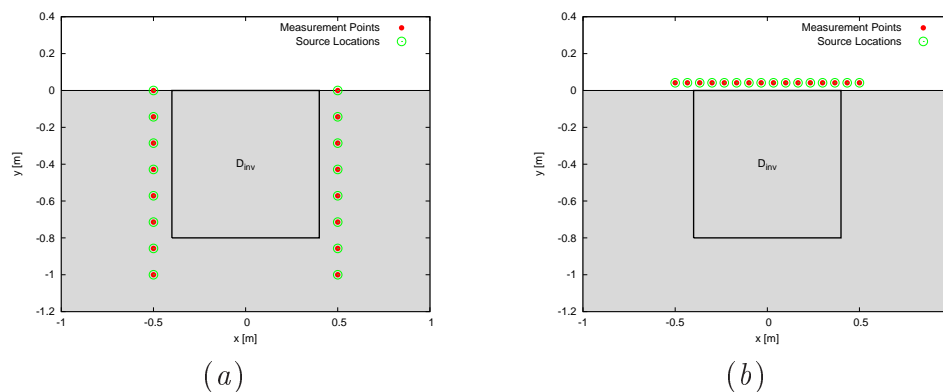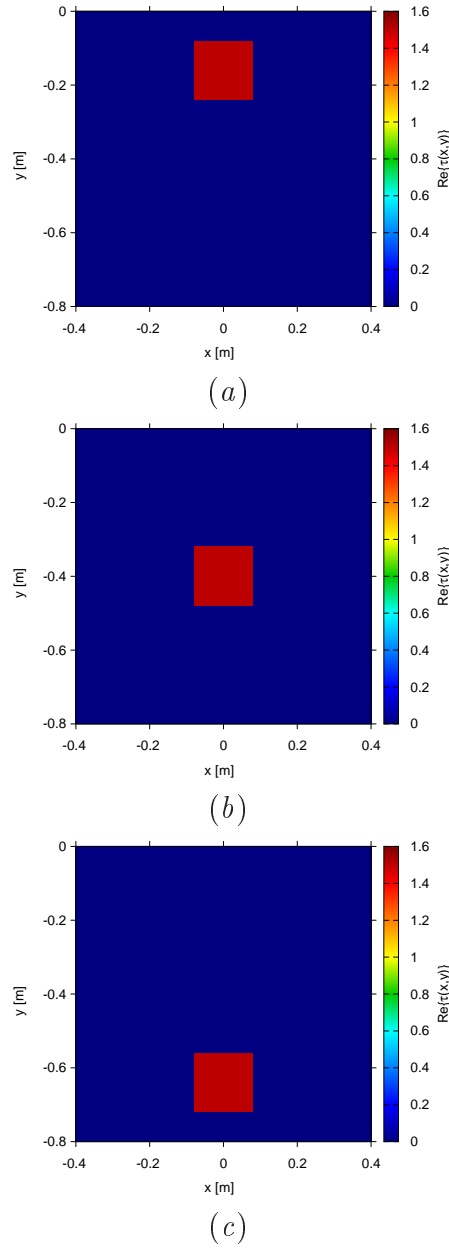$IMSA-IN$ cross-borehole $IMSA-IN$ half space

Figure 6.3: *Comparative Assessment (Square Scatterer at Different Depths -* $L = 0.16\,m$, *(*$x_c = 0.0\,m$, $\varepsilon_r = 5.5$, $\sigma = 0.01$ S/m [$\tau = 1.5$], $\varepsilon_{rB} = 4.0$, $\sigma_B = 0.01$ S/m, $SNR = 20$ dB*)* - Final reconstruction obtained by the $IMSA-IN$ method when considering a $(a)(b)(c)$ cross-borehole and $(d)(e)(f)$ an half space setup.

It is however mandatory to remember that cross-borehole setups (as the one depicted in Fig. 6.1(a)) require in real applications the drilling of the background medium in order to displace the probes below the interface. However, there are

a lot of practical scenarios when drilling is actually impossible (e.g., for the investigation of ancient ruins or historical buildings) or, even more, it can cause severe safety problems to the involved operators in critical applications such as demining [16]. For these reasons, in a lot of practical scenarios a half space [Fig. 6.1(b)] is not only preferrable but it is also the only possible choice. Given that, the strongly limited amount of information that can be collected by using such a prospecting configuration should be improved by trying to "add" information coming from other "*information sources*". In this thesis, this is effectively done by exploiting the available frequency diversity of real GPR measurements through the use of the $FHMF - CG$ technique presented in Chapter 5. In order to give the reader a more clear idea of what is the achievable performance when using the multi-frequency $FHMF - CG$ method, the same benchmark scenario considered for the previous analysis is used hereinafter (i.e., by keeping the same position and number of the V sources and M probes), but focusing the attention only on the half space setup [Fig. 6.1(b)]. More in details, Figs. 6.4(a)(b)(c) show the reconstructions obtained by using the single-frequency version of this technique, denoted as $MF - CG^2$. As it can be observed, the overall quality of the reconstructions obtained for different depths of the unknown scatterer is higher wrt that of the reconstructions obtained by the $IMSA - IN$ [Figs. 6.3(d)(e)(f)]. It is also evident that, even for the "*bottom*" scenario, the single-frequency $MF - CG$ is able to correctly identify the location of the target, even if it fails in properly reconstructing its electromagnetic characteristics [Fig. 6.4(c)]. These considerations are confirmed by the lower internal reconstruction error Ξ_{int}: $\Xi_{int}|_{MF-CG}^{"bottom"} \approx 4.21 \times 10^{-1}$ [Fig. 6.4(c)] vs. $\Xi_{int}|_{IMSA-IN}^{"bottom"} \approx 6.04 \times 10^{-1}$ [Fig. 6.3(f)]. The performance improvement in this case is due to the approximated nature of the IN method, as the "*inexact*" word suggests, while the CG approach handles the full derivation of the cost function without any kind of approximation.

Last but not least, the remarkable improvement in terms of reconstruction accuracy coming from the exploitation of multi-frequency data is visually confirmed by the reconstructions obtained by the $FHMF - CG$ method (Chapter 5) shown in Figs. 6.4(d)(e)(f). Thanks to the exploitation of $K = 5$ equally spaced frequency components of the GPR measured spectrum via the Frequency-Hopping (FH) scheme, the $FHMF - CG$ technique is able to correctly determine both the shape and the dielectric characteristics of the buried target [Figs. 6.4(d)(e)(f)] with an overall reconstruction accuracy significantly higher wrt its single-frequency counterpart [Figs. 6.4(a)(b)(c)]. Moreover, the information coming from different frequencies is able to "balance" the loss of information due to the use of a half space measurement configuration, as verified by the reconstruction obtained for the deepest target ["*bottom*", Fig. 6.4(f)]. In this case,

---

[2]In order to allow a fair comparison between the different inversion approaches, the same number of discretization cells $N = 100$ has been assumed for all the test cases presented in this section.

the internal error is $\Xi_{int}|_{FHMF-CG}^{"bottom"} \approx 2.21 \times 10^{-1}$, which is significantly lower if compared to the reconstruction obtained by the single-frequency $IMSA - IN$ [Fig. 6.3(f)] and by the single-frequency $MF - CG$ [Fig. 6.4(c)].
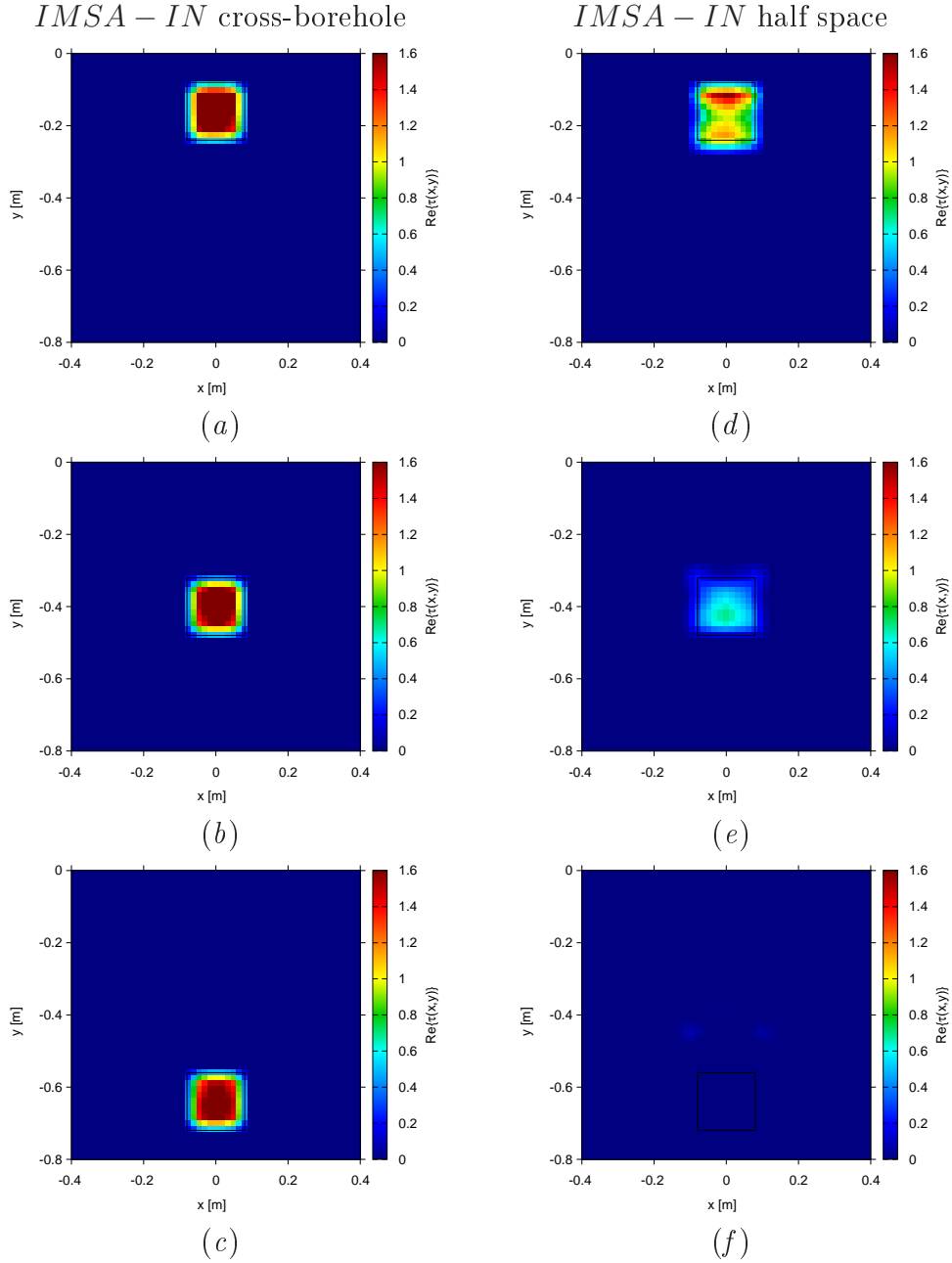
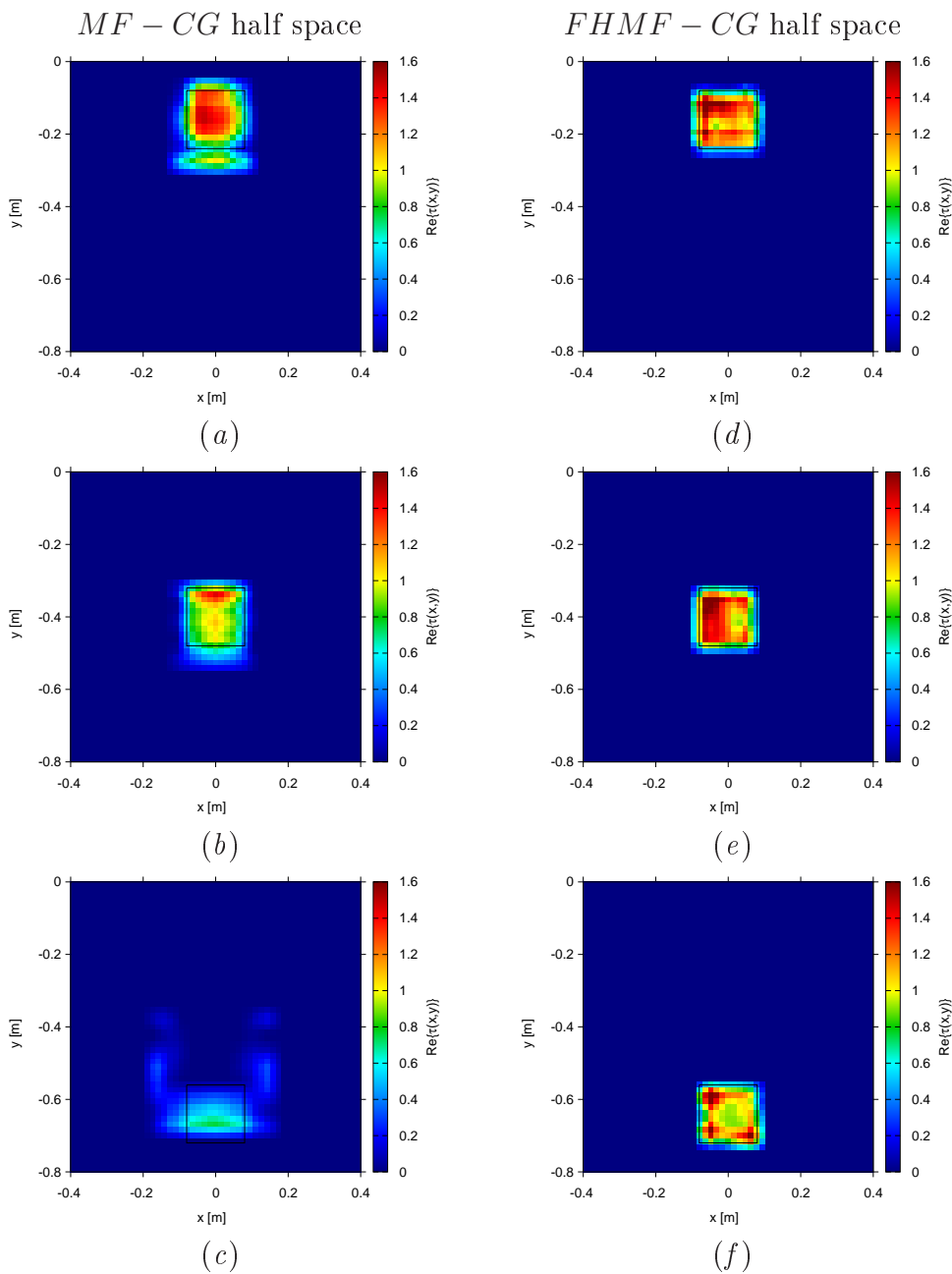Figure 6.4: *Comparative Assessment (Square Scatterer at Different Depths -* $L = 0.16\,m$, *($x_c = 0.0\,m$,* $\varepsilon_r = 5.5$, $\sigma = 0.01$ S/m $[\tau = 1.5]$, $\varepsilon_{rB} = 4.0$, $\sigma_B = 0.01$ S/m, $SNR = 20$ dB) - Final reconstruction obtained by the *(a)(b)(c)* single-frequency $MF{-}CG$ and by the *(d)(e)(f)* multi-frequency $FHMF{-}CG$ methods when considering a half space measurement setup.

6.2   Final Remarks

In this thesis, a new set of microwave imaging methods for subsurface prospecting has been introduced. Chapters 3 and 4 presented two single-frequency approaches based on the use of an inexact-Newton method. In particular, the inverse problem has been addressed in Chapter 3 by numerically solving the Lippmann-Schwinger equation under the second-order Born approximation. The proposed $IMSA-IN-SOBA$ reconstruction method has been validated through an extended set of numerical results involving different types of scatterers and noise conditions. Simulations have highlighted the following key results

- the proposed technique is able to profitably combine the well assessed regularization capabilities of the adopted local search technique (the inexact-Newton method) with the enhanced exploitation of available information provided by the multi-focusing strategy, which is able to reduce the problem of local minima arising from the *non-linearity* of the involved set of equations.

- Moreover, the combined strategy exhibits advantages over its standard "bare" implementation in terms of achieved accuracy and resolution, whatever the contrast distribution (homogeneous/inhomogeneous), the cross-section geometry and the noise level on measured data.

- Furthermore, the proposed multi-focusing approach overcomes the standard "bare" implementation also in terms of the computational efficiency, thanks to the significant reduction of the problem unknowns at each iterative step, which arises from the use of an adaptive coarse-to-fine discretization of the investigation areas at different levels of resolution.

The approach presented in Chapter 4 extends this approximated strategy by employing the full non-linear formulation of the scattering problem. In this way, the $IMSA-IN$ method is potentially able to deal with strong scatterers, too. The reconstruction performances have been evaluated by means of several numerical simulations. It has been found that

- the proposed approach provides quite good reconstructions of the considered targets showing a good robustness to the noise, as well;

- a significant performance improvement in terms of reconstruction accuracy can be observed wrt the $SOBA$-based approach presented in Chapter 3, especially for the retrieval of targets characterized by high values of the contrast function;

- the results from the multi-focusing strategy turned out to be better both in terms of reconstruction errors and computational resources than the standard bare inexact-Newton algorithm when applied to the same scattering configurations.

Finally, Chapter 5 presented an innovative information acquisition approach based on a nested frequency-hopping multi-focusing inversion technique for the solution of 2D *GPR* prospecting problems. Towards this end, an external iterative *FH* procedure has been proposed to handle multi-frequency *GPR* data, and its combination with an internal multi-resolution loop able to mitigate local minima issues in the associated inverse scattering problem has been presented. To minimize the arising multi-focusing cost function, a local search strategy based on *CG* has been implemented and integrated. The proposed *FHMF-CG* method has been validated against synthetic and measured *GPR* data, and a comparative assessment has been discussed. From the methodological viewpoint, the main contributions of this thesis include

1. the derivation of a multi-focusing scheme that, unlike state-of-the-art methods [54][72], is suitable for *GPR* prospecting and can handle time-domain data through Fourier processing;

2. the introduction of a frequency-hopping technique which, at each frequency step, suitably initializes both the total field [Eq. (5.11)] and the contrast [Eq. (5.10)] using the acquired information, unlike [91]-[93].

The numerical and experimental validation has pointed out the following main outcomes:

- the *FHMF-CG* method outperforms its single-resolution counterpart in terms of accuracy whatever the noise level, contrast, measurement setup, and target properties, except for very weak scatterers in low SNR scenarios in which the two methods provide comparable fidelities;

- thanks to its multi-focusing nature, the proposed approach is significantly more numerically efficient than a bare *FH-CG* technique;

- the introduced algorithm favourably compares with state-of-the-art techniques based on linear formulations and *TSVD* solvers;

- the *FHMF-CG* technique can be effectively used to detect the position, depth, and dielectric properties of buried objects starting from few raw *GPR* experimental measurements without the need to accurately model the actual soil properties and antenna geometries.

Moreover, it has been demonstrated that exploiting different frequency components of the measured GPR spectrum can effectively counterbalance the loss of information due to a strongly aspect-limited measurement setup, where sources and probes are both located above the interface. In practical scenarios where the drilling of the background medium for installing a cross-borehole measurement system is forbidden or simply prohibitive, an half space is the only possibile

choice. Given that, it has been proven that the capabilities of single-frequency approaches can be significantly enhanced by using multi-frequency strategies, as confirmed by the numerical results in Sect. 6.1.

Future works, beyond the scope of this thesis, will be aimed at extending the proposed methodologies to full 3D *GPR* scenarios, as well as at further assess their potentialities and limitations in dealing with experimental data of different nature. Moreover, the possibility to improve the accuracy of the methods through accurate modelling of the employed transmitting/receiving antennas within the inversion process is currently under investigation.

Bibliography

[1] R. Zoughi, *Microwave nondestructive testing and evaluation* (Kluwer Academic, 2000).

[2] M. Pastorino, *Microwave imaging* (John Wiley, 2010).

[3] G. C. Giakos, M. Pastorino, F. Russo, S. Chiwdhury, N. Shah and D. Davros, "Noninvasive imaging for the new century," IEEE Instrum. Meas. Mag. **2**, 32-35 (1999).

[4] O. Dorn and D. Lesselier, Special issue on "Electromagnetic inverse problems: emerging methods and novel applications," Inverse Probl. **26** (2010).

[5] M. Bertero and P. Boccacci, *Introduction to inverse problems in imaging* (IOP Press, 1998).

[6] Y. J. Kim, L. Jofre, F. De Flaviis, and M. Q. Feng, "Microwave reflection tomographic array for damage detection of civil structures," IEEE Trans. Antennas Propag. **51**, 3022-3032 (2003).

[7] S. Kharkovsky and R. Zoughi, "Microwave and millimeter wave nondestructive testing and evaluation - overview and recent advantages," IEEE Instrum. Meas. Mag. **10**, 26-38 (2007).

[8] G. Bozza, C. Estatico, M. Pastorino, and A. Randazzo, "Microwave Imaging for Nondestructive Testing of Dielectric Structures: Numerical Simulations Using an Inexact Newton Technique," Materials Evaluation **65**, 917-922 (2007).

[9] M. Benedetti, M. Donelli, A. Martini, M. Pastorino, A. Rosani, and A. Massa, "An innovative microwave-imaging technique for nondestructive evaluation: Applications to civil structures monitoring and biological bodies inspection," IEEE Trans. Instrum. Meas. **55**, 1878-1883 (2006).

[10] P. Kosmas, C. M. Rappaport, and E. Bishop, "Modeling with the FDTD method for microwave breast cancer detection," IEEE Trans. Microw. Theory Techn. **52**, 1890-1897 (2004).

[11] P. Kosmas and C. M. Rappaport, "FDTD-based time reversal for microwave breast cancer detection-localization in three dimensions," IEEE Trans. Microw. Theory Techn. **54**, 1921- 1927 (2006).

[12] G. Bozza, M. Brignone and M. Pastorino, "Application of the no-sampling linear sampling method for breast cancer detection," IEEE Trans. Biomed. Eng. **57**, 2525-2534 (2010).

[13] C.-C. Chen, J. T. Johnson, M. Sato and A. G. Yarovoy, Special issue on "Subsurface sensing using ground penetrating radar," IEEE Trans. Geosci. Remote Sensing, **45** (2007).

[14] R. Firoozabadi, E. L. Miller, C. M. Rappaport, and A. W. Morgenthaler, "Subsurface sensing of buried objects under a randomly rough surface using scattered electromagnetic field data," IEEE Trans. Geosci. Remote Sensing **45**, 104-117 (2007).

[15] T. Isernia, L. Crocco, and M. D'Urso, "New tools and series for forward and inverse scattering problems in lossy media," IEEE Geosci. Remote Sensing Lett. **1**, 327- 331 (2004).

[16] F. Soldovieri, O. Lopera, S. Lambot, "Combination of advanced inversion techniques for an accurate target localization via GPR for demining applications," IEEE Trans. Geosci. Remote Sensing **49**, 451-461 (2011).

[17] I. Catapano, L. Crocco, and T. Isernia, "Improved sampling methods for shape reconstruction of 3-D buried targets," IEEE Trans. Geosci. Remote Sensing, **46**, 3265-3273 (2008).

[18] A. P. Anderson and P. J. Richards, "Microwave imaging of subsurface cylindrical scatters from crosspolar backscatter," Electron. Lett. **13**, 617-619 (1977).

[19] F. Soldovieri, R. Solimene, L. Lo Monte, M. Bavusi, "Sparse reconstruction from GPR data with applications to rebar detection," IEEE Trans. Instr. Meas. **60**, 1070-1079 (2011).

[20] T. M. Habashy and A. Abubakar, "A general framework for constraint minimization for the inversion of electromagnetic measurements," PIER **46**, 265-312 (2004).

[21] G. Oliveri, P. Rocca, and A. Massa, "A Bayesian compressive sampling-based inversion for imaging sparse scatterers," IEEE Trans. Geosci. Remote Sens. **49**, 3993-4006 (2011).

[22] L. Poli, G. Oliveri, P. Rocca, and A. Massa, "Bayesian Compressive Sensing approaches for the reconstruction of two-dimensional sparse scatterers under TE illuminations", IEEE Trans. Geosci. Remote Sens., **51**, 2920-2936 (2013).

[23] L. Poli, G. Oliveri, F. Viani, and A. Massa, "MT-BCS-based microwave imaging approach through minimum-norm current expansion," IEEE Trans. Antennas Propag. **61**, 4722-4732 (2013).

[24] G. Oliveri, L. Poli, P. Rocca, and A. Massa, "Bayesian compressive optical imaging within the Rytov approximation," Opt. Lett. **37**, 1760-1762 (2012).

[25] L. Poli, G. Oliveri, and A. Massa "Microwave imaging within the first-order Born approximation by means of the contrast-field Bayesian compressive sensing," IEEE Trans. Antennas Propag. **60**, 2865-2879 (2012).

[26] T. J. Cui, W. C. Chew, A. A. Aydiner and S. Chen, "Inverse scattering of two-dimensional dielectric objects in a lossy earth using the distorted Born iterative method," IEEE Trans. Geosci. Remote Sensing **39**, 339-346 (2001).

[27] R. Pierri and G. Leone, "Inverse scattering of dielectric cylinders by a second-order Born approximation," IEEE Trans. Geosci. Remote Sens. **37**, 374-382 (1999).

[28] G. Bozza, C. Estatico, M. Pastorino, and A. Randazzo, "Application of an inexact-Newton method within the second-order Born approximation to buried objects," IEEE Geosci. Remote Sensing Lett. **4**, 51-55 (2007).

[29] C. Estatico, M. Pastorino, and A. Randazzo, "An inexact-Newton method for short-range microwave imaging within the second-order Born approximation," IEEE Trans. Geosci. Remote Sensing **43**, 2593-2605 (2005).

[30] H. Harada, D. J. N. Wall, T. Takenaka, and T. Tanaka, "Conjugate gradient method applied to inverse scattering problems," IEEE Trans. Antennas Propag. **43**, 784-792 (1995).

[31] T. Takenaka, H. Zhou and T. Tanaka, "Inverse scattering for a three-dimensional object in the time domain," J. Opt. Soc. Am. A **20**, 1867-1874 (2003).

[32] P. M. van Den Berg and A. Abubakar, "Contrast source inversion method: state of the art," PIER **34**, 189-218 (2001).

[33] S. Caorsi, A. Massa, M. Pastorino, and A. Randazzo, "Electromagnetic detection of dielectric scatterers using phaseless synthetic and real data and the memetic algorithm," IEEE Trans. Geosci Remote Sens **41**, 2745-2753 (2003).

[34] P. Rocca, G. Oliveri, and A. Massa, "Differential evolution as applied to electromagnetics," IEEE Antennas Propag. Magazine **53**, 38-49 (2011).

[35] M. Pastorino, A. Massa, and S. Caorsi, "A microwave inverse scattering technique for image reconstruction based on a genetic algorithm," IEEE Trans. Instrum. Meas. **49**, 573- 578 (2000).

[36] S. Caorsi, A. Massa, and M. Pastorino, "A computational technique based on a real-coded genetic algorithm for microwave imaging purposes," IEEE Trans. Geosci. Remote Sens. **38**, 1697-1708 (2000).

[37] A. Massa, M. Pastorino, and A. Randazzo, "Reconstruction of two-dimensional buried objects by a hybrid differential evolution method," Inverse Probl. **20**, 135-150 (2004).

[38] M. Pastorino, S. Caorsi, A. Massa, and A. Randazzo, "Reconstruction algorithms for electromagnetic imaging," IEEE Trans. Instrum. Meas. **53**, 692-699 (2004).

[39] A. Qing, "Dynamic differential evolution strategy and applications in electromagnetic inverse scattering problems," IEEE Trans. Geosci. Remote Sensing **44**, 116-125 (2005).

[40] A. Semnani, I. T. Rekanos, M. Kamyab and T. G. Papadopoulos, "Two-dimensional microwave imaging based on hybrid scatterer representation and differential evolution," IEEE Trans. Antenas Propag. **58**, 3289-3298 (2010).

[41] P. Rocca, M. Benedetti, M. Donelli, D. Franceschini, and A. Massa, "Evolutionary optimization as applied to inverse scattering problems," Inverse Problems **25**, 1-41 (2009).

[42] M. Pastorino, "Stochastic optimization methods applied to microwave imaging: A review," IEEE Trans. Antennas Propag. **55**, 538-548 (2007).

[43] G. Bozza, C. Estatico, M. Pastorino, and A. Randazzo, "An inexact Newton method for microwave reconstruction of strong scatterers," IEEE Antennas Wireless Propag. Lett. **5**, 61-64 (2006).

[44] C. Estatico, G. Bozza, A. Massa, M. Pastorino, and A. Randazzo, "A two-step iterative inexact-Newton method for electromagnetic imaging of dielectric structures from real data," Inverse Problems **43**, S81-S94 (2005).

[45] G. Bozza, C. Estatico, A. Massa, M. Pastorino, and A. Randazzo, "Short-range image-based method for the inspection of strong scatterers using microwaves," IEEE Trans. Instrum. Meas. **56**, 1181-1188 (2007).

96

[46] G. Bozza and M. Pastorino, "An inexact Newton-based approach to microwave imaging within the contrast source formulation," IEEE Trans. Antennas Propag. **57**, 1122-1132 (2009).

[47] A. Randazzo, G. Oliveri, A. Massa, and M. Pastorino, "Electromagnetic inversion with the multiscaling inexact-Newton method - experimental validation," Microw. Opt. Tech. Lett. **53**, 2834-2838 (2011).

[48] G. Oliveri, L. Lizzi, M. Pastorino and A. Massa, "A nested multi-scaling inexact-Newton iterative approach for microwave imaging," IEEE Trans. Antennas Propag. **60**, 971-983 (2012).

[49] G. Oliveri, A. Randazzo, M. Pastorino and A. Massa, "Electromagnetic imaging within the contrast-source formulation by means of the multiscaling inexact Newton method," J. Opt. Soc. America A **29**, 945-958 (2012).

[50] M. Lambert and D. Lesselier, "Binary-constrained inversion of a buried cylindrical obstacle from complete and phaseless magnetic fields," Inv. Probl. **16**, 563-576 (2000).

[51] A. Baussard, E. L. Miller, and D. Lesselier, "Adaptive multiscale reconstruction of buried objects," Inverse Problems **20**, S1-S15 (2004).

[52] D. Franceschini, A. Massa, M. Pastorino, and A. Zanetti, "Multi-resolution iterative retrieval of real inhomogeneous targets," Inverse Problems **21**, 51-63 (2005).

[53] G. Oliveri, Y. Zhong, X. Chen, and A. Massa, "Multi-resolution subspace-based optimization for inverse scattering," J. Opt. Soc. America A **28**, 2057-2069 (2011).

[54] S. Caorsi, M. Donelli, D. Franceschini, and A. Massa, "A new methodology based on an iterative multiscaling for microwave imaging," IEEE Trans. Microwave Theory Tech. **51**, 1162-1173 (2003).

[55] D. C. Stinson, *Intermediate mathematics of electromagnetics* (Prentice-Hall, 1976).

[56] J. H. Richmond, "Scattering by a dielectric cylinder of arbitrary cross shape," IEEE Trans. Antennas Propag. **13**, 334-341 (1965).

[57] O. M. Bucci and G. Franceschetti, "On the degrees of freedom of scattered fields," IEEE Trans. Antennas Propag. **37**, 918- 926 (1989).

[58] O. M. Bucci, L. Crocco, T. Isernia and V. Pascazio, "Subsurface inverse scattering problems: quantifying qualifying and achieving the available information," IEEE Trans. Geosci. Remote Sensing **39**, 2527-2538 (2001).

[59] R. Persico, *Introduction to Ground Penetrating Radar: Inverse Scattering and Data Processing*, London, (Wiley-IEEE Press, 2014).

[60] C. A. Balanis, *Advanced Engineering Electromagnetics* (John Wiley & Sons, 1989).

[61] L. Landweber, "An iteration formula for Fredholm integral equations of the first kind," American Journal of Mathematics **73**, 615-624 (1951).

[62] C.-H. Huang, C.-C. Chiu, C.-L. Li, and K.-C. Chen, "Time domain inverse scattering of a two-dimensional homogenous dielectric object with arbitrary shape by particle swarm optimization," *Prog. Electromagn. Res.* **82**, 381-400 (2008).

[63] F. Li, Q. H. Liu, and L.-P. Song, "Three-dimensional reconstruction of objects buried in layered media using Born and distorted Born iterative methods," *IEEE Geosci. Remote Sens. Lett.* **1**, 107-111 (2004).

[64] T. G. Papadopoulos and I. T. Rekanos, "Time-domain microwave imaging of inhomogeneous Debye dispersive scatterers," *IEEE Trans. Antennas Propag.* **60**, 1197-1202 (2012).

[65] C. Yu, M. Yuan, and Q. H. Liu, "Reconstruction of 3D objects from multifrequency experimental data with a fast DBIM-BCGS method," *Inverse Probl.* **25**, 024007 (2009).

[66] D. W. Winters, B. D. Van Veen, and S. C. Hagness, "A sparsity regularization approach to the electromagnetic inverse scattering problem," *IEEE Trans. Antennas Propag.* **58**, 145-154 (2010).

[67] C. Gilmore, P. Mojabi, and J. LoVetri, "Comparison of an enhanced distorted Born iterative method and the multiplicative-regularized contrast source inversion method," *IEEE Trans. Antennas Propag.* **57**, 2341-2351 (2009).

[68] C. Estatico, M. Pastorino, and A. Randazzo, "A novel microwave imaging approach based on regularization in Lp banach spaces," *IEEE Trans. Antennas Propag.* **60**, 3373-3381 (2012).

[69] M. Salucci, G. Oliveri, A. Randazzo, M. Pastorino, and A. Massa, "Electromagnetic subsurface prospecting by a multifocusing inexact Newton method within the second-order Born approximation," *J. Opt. Soc. Am. A* **31**, 1167-1179 (2014).

[70] R. Solimene, M. A. Maisto, and R. Pierri, "Role of diversity on the singular values of linear scattering operators: The case of strip objects," *J. Opt. Soc. Am. A* **30**, 2266-2272 (2013).

[71] J. M. Johnson and V. Rahmat-Samii, "Genetic algorithms in engineering electromagnetics," *IEEE Antennas Propag. Mag.* **39**, 7-21 (1997).

[72] S. Caorsi, M. Donelli, and A. Massa, "Detection, location, and imaging of multiple scatterers by means of the iterative multiscaling method," *IEEE Trans. Microw. Theory Tech.* **52**, 1217-1228 (2004).

[73] G. Leone, R. Persico, R. Solimene, "A quadratic model for electromagnetic subsurface prospecting," *AEU-Int. J. Electron. Commun.* **57**, 33-46 (2003).

[74] M. Donelli, G. Franceschini, A. Martini, and A. Massa, "An integrated multiscaling strategy based on a particle swarm algorithm for inverse scattering problems," *IEEE Trans. Geosci. Remote Sens.* **44**, 298-312 (2006).

[75] D. Franceschini, M. Donelli, R. Azaro, and A. Massa, "Dealing with multifrequency scattering data through the IMSA," *IEEE Trans. Antennas Propag.* **55**, 2412-2417 (2007).

[76] R. Harrington, *Field Computation by Moment Methods* (IEEE Press, 1993).

[77] D. Lesselier and T. Habashy, Special issue on "Electromagnetic imaging and inversion on the Earth's subsurface," *Inverse Prob.* **16** (2000).

[78] W. C. Chew and D. Lesselier, Special issue on "Electromagnetic characterization of buried obstacles," *Inverse Prob.* **20** (2004).

[79] L. Peters, J. J. Daniels, and J. D. Young, "Ground penetrating radar as a subsurface environmental sensing tool," *IEEE Proc.* **82**, 1802-1822 (1994).

[80] X. Xu, E. L. Miller, C. M. Rappaport, and G. D. Sower, "Statistical method to detect subsurface objects using array ground-penetrating radar data," *IEEE Trans. Geosci. Remote Sens.* **40**, 963-976 (2002).

[81] R. Wu, X. Li, and J. Li, "Continuous pavement profiling with ground-penetrating radar," *IEE Proc. Radar Sonar Navig.*, vol. 149, no. 4, pp. 183-193, Aug. 2002.

[82] C. Le Bastard, V. Baltazart, Y. Wang, and J. Saillard, "Thin-pavement thickness estimation using GPR with high-resolution and superresolution methods," *IEEE Trans. Geosci. Remote Sens.* **45**, 2511-2519 (2007).

[83] L. Crocco, M. Pieraccini, M. Sato, and F. Soldovieri, "Foreword to the special issue on Ground Penetrating Radar: modeling tools, imaging methods and systems concepts," *IEEE J. Sel. Topics Appl. Earth Obs.* **4**, 735-738 (2011).

[84] R. Persico, R. Bernini, and F. Soldovieri, "The role of the measurement configuration in inverse scattering from buried objects under the Born approximation," *IEEE Trans. Antennas Propag.* **53**, 1875-1887 (2005).

[85] R. Persico, "On the role of measurement configuration in contactless GPR data processing by means of linear inverse scattering," *IEEE Trans. Antennas Propag.* **54**, 2062-2071 (2006).

[86] R. Persico and F. Soldovieri, "A microwave tomography approach for a differential configuration in GPR prospecting," *IEEE Trans. Antennas Propag.* **54**, 3541-3548 (2006).

[87] F. Soldovieri, R. Persico, and G. Leone, "Frequency diversity in a linear inversion algorithm for GPR prospecting," *Proc. 10th International Conference on GPR*, 21-24 June, Delft, The Netherlands, pp. 87-90, 2004.

[88] R. Persico and F. Soldovieri, "Effects of background removal in linear inverse scattering," *IEEE Trans. Geosci. Remote Sens.* **46**, 1104-1114 (2008).

[89] P. Meincke, "Efficient calculation of Born scattering for fixed-offset ground-penetrating radar surveys," *IEEE Geosci. Remote Sensing Lett.* **4**, 88-92 (2007).

[90] T. Isernia, V. Pascazio, and R. Pierri, "On the local minima in a tomographic imaging technique," *IEEE Trans. Geosci. Remote Sens.* **39**, 1596-1607 (2001).

[91] W. C. Chew and J.-H. Lin, "A frequency-hopping approach for microwave imaging of large inhomogeneous bodies," *IEEE Microw. Guided Wave Lett.* **5**, 439-441 (1995).

[92] R. Ferraye, J. Dauvignac, and C. Pichot, "An inverse scattering method based on contour deformations by means of a level set method using frequency hopping technique," *IEEE Trans. Antennas Propag.* **51**, 1100-1113 (2003).

[93] D. A. Woten, M. R. Hajihashemi, A. M. Hassan, and M. El-Shenawee, "Experimental microwave validation of level set reconstruction algorithm," *IEEE Trans. Antennas Propag.* **58**, 230-233 (2010).

[94] W. H. Press, S. A. Teukolsky, W. T. Vetterling, and B. P. Flannery, *Numerical Recipes: The Art of Scientific Computing*, 3rd Edition (Cambridge University Press, 2007).

[95] A. Giannopoulos (2014), *GprMax Software* [Online] Available online: *http://www.see.ed.ac.uk/drupal/gprmax*

[96] F. Soldovieri, R. Persico, and G. Leone, "Frequency diversity in a linear inversion algorithm for GPR prospecting," *Subsurface Sensing Technol. Appl.*, **6**, 25-42 (2005).

[97] I. Hill (2013), *NSGG Geophysics Test Sites* [online] Available: *www.nsgg.org.uk/test-sites*

[98] G. Franceschetti and C. H. Papas, "Pulsed antennas," *IEEE Trans. Antennas Propag.* **22**, 651-661 (1974).

[99] W. Wiesbeck, G. Adamiuk, and C. Sturm, "Basic properties and design principles of UWB antennas," *Proc. IEEE* **97**, 372-385 (2009).

[100] F. Soldovieri, G. Prisco, and R. Persico, "A strategy for the determination of the dielectric permittivity of a lossy soil exploiting GPR surface measurements and a cooperative target," *J. Appl. Geophys.* **64**, 288-295 (2009).

[101] P. M. van den Berg and A. Abubakar, "Linear and nonlinear inversion of GPR data," *Proc. International Workshop on Advanced Ground Penetrating Radar*, pp. 156-163, 14-16 May 2003.

[102] T. Tanaka, N. Kuroki, and T. Takenaka, "Filtered forward-backward time-stepping method applied to reconstruction of dielectric cylinders," *J. Electromagn. Waves Appl.* **17**, 253-270 (2003).

[103] MALA GPR Australia (2014), *MALA X3M system datasheet* [online]. Available: *malagpr.com.au/products/mala-x3m*

[104] Geomatrix Earth Science Ltd. (2013), *NSGG UXO Test Site* [online] Available: *www.geomatrix.co.uk/tools/nsgg-uxo-test-site.php*

Appendix A

Derivation of Eq. (4.5) and Eq. (4.6)

This appendix reports the details of the discretized version of the functional Eq. (4.5) [i.e., Eq. (4.6)]. In order to numerically solve the inverse problem at hand, the investigation area at a given scale s, Ω_s, is partitioned into N square subdomains. In each n-th cell, both the contrast function and the incident field are assumed to be piecewise constant such as their distributions in Ω_s turn out to be

$$\tau\left(x, y\right) = \sum_{n=1}^{N} \tau_n \psi_n\left(x, y\right) \tag{A.1}$$

$$E_{inc/tot}^{(v)}\left(x, y\right) = \sum_{n=1}^{N} E_{inc/tot,n}^{(v)} \psi_n\left(x, y\right) \tag{A.2}$$

where $\psi_n\left(x, y\right)$ is a rectangular pulse basis function [56]. By testing the scattering equations using Dirac's delta functions centered at the measurement points $\left(x_m^{(v)}, y_m^{(v)}\right)$, $m = 1, ..., M$, $v = 1, ..., V$, equations (4.1) and (4.2) become

$$E_{tot,n}^{(v)} = E_{inc,n}^{(v)} + \sum_{l=1}^{N} \tau_l E_{tot,l}^{(v)} \int_{\Omega_{s,l}} \mathcal{G}_{int}\left(x_n, y_n, x', y'\right) dx' dy' \tag{A.3}$$

$$E_{scatt,m}^{(v)} = \sum_{l=1}^{N} \tau_l E_{tot,l}^{(v)} \int_{\Omega_{s,l}} \mathcal{G}_{ext}\left(x_m^{(v)}, y_m^{(v)}, x', y'\right) dx' dy' \tag{A.4}$$

where $E_{scatt,m}^{(v)} = E_{scatt}^{(v)}\left(x_m^{(v)}, y_m^{(v)}\right)$ and (x_n, y_n) is the center of the n-th subdomain of Ω_s (i.e., $\Omega_{s,n}$).
By considering all the measurement points and rewriting the equations in a matrix form, the following equation is obtained

$$\mathbf{A}^{(v)}\left(\boldsymbol{\tau}; \mathbf{E}_{tot}^{(v)}\right) = \begin{bmatrix} \mathbf{G}_{data}^{(v)} diag\left(\boldsymbol{\tau}\right) \mathbf{E}_{tot}^{(v)} \\ \left(\mathbf{I} - \mathbf{G}_{state} diag\left(\boldsymbol{\tau}\right)\right) \mathbf{E}_{tot}^{(v)} \end{bmatrix} = \mathbf{b}^{(v)} = \begin{bmatrix} \mathbf{E}_{scatt}^{(v)} \\ \mathbf{E}_{inc}^{(v)} \end{bmatrix} \tag{A.5}$$

where $\boldsymbol{\tau} = [\tau_1, ..., \tau_N]^t$ is an array containing the values of the contrast function in the N subdomains, $diag\,(\boldsymbol{\tau})$ is a diagonal matrix whose diagonal elements are the values of the array $\boldsymbol{\tau}$, $\mathbf{E}_{tot}^{(v)} = \left[E_{tot,1}^{(v)}, ..., E_{tot,N}^{(v)} \right]$ and $\mathbf{E}_{inc}^{(v)} = \left[E_{inc,1}^{(v)}, ..., E_{inc,N}^{(v)} \right]$ are two arrays containing the values of the total and incident electric fields in the N sub-domains, and $\mathbf{E}_{scatt}^{(v)} = \left[E_{scatt,1}^{(v)}, ..., E_{scatt,M}^{(v)} \right]$ is an array with the values of the scattered electric field at the M measurement points of the v-th view. Moreover, $\mathbf{G}_{data}^{(v)}$ and $\mathbf{G}_{state}$ are two matrices of sizes $M \times N$ and $N \times N$, respectively, whose elements are the integrals of the Green's function.

Finally, Equation (4.6) is yielded by combining all the V views as follows

$$\mathbf{A}\,(\boldsymbol{\tau}; \mathbf{E}_{tot}) = \begin{bmatrix} \mathbf{G}_{data}^{(1)} diag\,(\boldsymbol{\tau})\, \mathbf{E}_{tot}^{(1)} \\ (\mathbf{I} - \mathbf{G}_{state} diag\,(\boldsymbol{\tau}))\, \mathbf{E}_{tot}^{(1)} \\ \vdots \\ \mathbf{G}_{data}^{(V)} diag\,(\boldsymbol{\tau})\, \mathbf{E}_{tot}^{(V)} \\ (\mathbf{I} - \mathbf{G}_{state} diag\,(\boldsymbol{\tau}))\, \mathbf{E}_{tot}^{(v)} \end{bmatrix} = \mathbf{b} = \begin{bmatrix} \mathbf{E}_{scatt}^{(1)} \\ \mathbf{E}_{inc}^{(1)} \\ \vdots \\ \mathbf{E}_{scatt}^{(V)} \\ \mathbf{E}_{inc}^{(V)} \end{bmatrix} \qquad (A.6)$$

where $\mathbf{E}_{tot} = \left[\left(\mathbf{E}_{tot}^{(1)} \right)^t, ..., \left(\mathbf{E}_{tot}^{(V)} \right)^t \right]^t$.